Title: Coronin1A regulates tumor microenvironment in colitis-associated colorectal cancer in a SUMO-dependent way

Rohan Babar[1], Poorvi Saini[1a], Neha Guliya,[1a] , Vishnu Ashok Kumar E[2b], Prakhar Varshney[3b] , Aamir Suhail[4] , Mukesh Singh [5], Prabhakar Mujagond[6], Shivangi Tyagi[1,] Lalita Mehra[5], Dolly Jain[1] Prasenjit Das[5] Jean Pieters[7], Krishnan Vengadesan[1] Avinash Bajaj[1] , Vineet Ahuja[5] and Chittur V. Srikanth [1,*]

1. Laboratory of Gut Infection and Inflammation Biology, Regional Centre for Biotechnology, 3rd milestone, Faridabad-Gurugram expressway, Faridabad. India 121001.
2. Nencki Institute of Experimental Biology, Warsaw, Poland.
3. Department of Laboratory Medicine and Pathology, Centre for Immunology, University of Minnesota, USA.
4. Harvard Medical School, USA.
5. All India Institute of Medical Sciences, New Delhi, India.
6. Meril Life Science Pvt.Ltd, India
7. Biozentrum, University of Basel, Switzerland.

a: second author with equal contribution, b: third author with equal contribution.

*** Corresponding Author:**

C. V. Srikanth: cvsrikanth@rcb.res.in

ABSTRACT

Inflammatory bowel disease (IBD), comprising Crohn's disease and Ulcerative colitis, is a group of multifactorial illnesses with persistent gastrointestinal inflammation and a series of undesirable consequences. IBD patients have a three times higher risk of developing colitis-associated colorectal cancer (CAC). A higher mutational burden due to persistent inflammation acts as a driver of dysplasia and even tumorigenesis. While the pathological sequence is known, the molecular mechanisms underlying the transition from chronic inflammation to CAC remain largely elusive. Post-translational modification- SUMOylation plays an integral role in shaping gut inflammation as well as several forms of cancers, including sporadic colorectal cancer. In this study, the contribution of SUMOylation to CAC pathogenesis was characterized. In the AOM-DSS CAC mice model and human IBD patient specimens, SENP5, but not other deSUMOylases, shows an altered expression. Notably, both SENP5 expression dynamics and alterations in the SUMOylome occur in chronically inflamed and neoplastic colon tissues. SENP5 interactome analysis identified Coronin1A (Coro1A), an actin-binding protein predominantly expressed in immune cells. Coro1A also shows a state-specific, distinct expression pattern in the colon. Interestingly, in contrast to wild-type mice, Coro 1A knockout mice were resistant to polyp formation, with reduced cell proliferation, oncogene expression, and epithelial-to-mesenchymal transition (EMT) gene activation, and reduced extracellular matrix (ECM) development and fibrosis, suggesting its integral role in tumorigenesis. WT mice with chronically inflamed colons and polyps have a higher number of M2-like macrophages, with increased abundance of Coro1A, suggesting a role of Coro1A in modulating the tissue microenvironment toward a pro-tumorigenic state. Mechanistically, Coro1A physically interacts with TGF-β RI and regulates TGF-β-TGF-β RI signalling endosome stability, thereby controlling TGF-β-mediated macrophage polarization. Detailed *in vitro* experiments revealed stabilization of Coro 1A through its interaction with SUMOylated Raftlin protein. Overall, Coro 1A is necessary and sufficient for TGF-β signalling, macrophage polarization, and tumorigenesis in CAC.

Key Words: Coronin 1A, SENP5, Transforming Growth Factor -β receptors, M2 macrophages, Colitis-associated colorectal cancer, SUMO2/3.

55 **Introduction:**

56 Colorectal cancer (CRC) is a notorious form of gastrointestinal cancer, with high incidence and
57 alarmingly poor prognosis (Bray et al., 2024; Sung et al., 2025; Schmitt & Greten, 2021). Despite
58 some improvements in therapy, the mortality of CRC remains significantly high, with a 5-year
59 survival rate for stage 4 CRC being less than 10%. Predominant forms of colorectal cancer include
60 (a) sporadic colorectal cancer (hereafter SCRC), which arises due to spontaneous mutation(s) in
61 colorectal epithelium, and (b) colitis-associated colorectal cancer (hereafter CAC), resulting from
62 chronic inflammation in the gastrointestinal tract (Foersch & Neurath, 2014; R. W. Zhou et al.,
63 2023). Multiple routes of tumor initiation and progression in CRC include distinct molecular
64 drivers, such as Adenomatous polyposis coli (APC), TP53, Kirsten rat sarcoma (KRAS), B-Raf
65 protooncogene ser/thre kinase (BRAF), PIK3CA, MMR genes (MSH2, MSH6, and MLH1), and
66 SMAD4, etc (Bogaert & Prenen, 2014; Díaz-Gay et al., 2025; Su et al., 2024). Significantly, the
67 underlying molecular pathology differs across CRC subtypes. SCRC typically follows an
68 adenoma-to-carcinoma sequence driven by prior genetic predispositions (Yamagishi et al., 2016;
69 Yin et al., 2023). Whereas CAC begins with chronic inflammation, progresses through grades of
70 dysplasia, and ultimately ends in carcinoma(Zhou et al., 2023). Consistently, patients with Crohn's
71 disease (CD) and ulcerative colitis (UC) display a 2-3-fold higher risk of developing CAC (Shawki
72 et al., 2018; Yashiro, 2014; Yin et al., 2023). Chronic inflammation exposes IBD patients to
73 repeated cycles of damage and healing of the mucosa, triggering genetic and/or epigenetic
74 perturbations. These events, referred to as induced field cancerization, prime the tumorigenesis
75 process. Consistent with this, ulcerative colitis patients display a 25-fold higher mutational burden,
76 rendering them susceptible to CAC (Kakiuchi et al., 2020). Infiltrating immune cells and resident
77 fibroblasts of the chronically inflamed gut can induce Wnt-β-Catenin, STAT3/IL-6, and
78 COX2/PGE2 pathways, which are potentially pro-tumorigenic (Dan et al., 2023; Shawki et al.,
79 2018). The tissue microenvironment in this case generates robust reactive oxygen/nitrogen species
80 along with a secretome comprising IL-6, TNF-α, GM-CSF, IL-23, and IL-17, further contributing
81 to DNA damage, epithelial proliferation, and myeloid cell recruitment and activation. Once
82 tumorigenesis is set, the tissue microenvironment is reprogrammed into a tumor-favoring
83 immunosuppressive state. TGF-β, IL-10 loop, or CCR2/CXCL-12 immune evasion pathways
84 induce polarization of immune cells into M2 macrophages, N2 neutrophils, Th2 cells, and T-reg
85 cells (Y. Deng et al., 2025; M. Zhang et al., 2023). Collectively, these events shield dysplastic cells

86 from immune surveillance and foster their proliferation. However, the mechanisms underlying
87 TME reprogramming remain elusive.

88 Macrophage involvement, characterized as CD11b^{+}, F4/80^{+}, and Ly6C high and M2 type
89 macrophages, which are referred to as tumor-associated macrophages (TAMs), significantly
90 contributes to the initiation and progression of CAC(Y. Deng et al., 2025; Shin et al., 2023;
91 Hardbower et al., 2017; Y. H. Sheng et al., 2022; Y. Wang et al., 2023; Yuan et al., 2021). Though
92 crosstalk among M2 macrophages, surrounding stromal cells, and other immune cells shapes the
93 tumor microenvironment during CAC progression, there is a lack of mechanistic understanding
94 of these events.

95 Expansion of immunosuppressive, pro-tumorigenic microenvironment- creates a permissive
96 niche for dysplastic clones to proliferate. A form of cellular post-translational modification
97 (PTM), called SUMOylation, has been shown to be integral in shaping inflammation and cancer.
98 Mediated by the action of three enzymes (E1, E2, and E3), the covalent attachment of SUMO
99 protein isoform (SUMO 1-5) to the target protein takes place, which potentially modulates its
100 function. The deSUMOylase enzymes (SENP1-3 and SENP5-7) then deconjugate the SUMO
101 attachment, making the process reversible. A series of publications have demonstrated a strong
102 connection of SUMOylation with inflammation (Mustfa et al., 2017; Suhail et al., 2019),(Long et
103 al., 2025; Ma et al., 2024). Dysregulation of the SUMOylation pathway has also been linked to
104 EMT and cancer pathophysiology (Gu et al., 2023a; L. Wang et al., 2021). The key molecules
105 involved in the transition from chronic colitis to cancer, such as NF-κB, β-Catenin, p53, AKT,
106 and STAT3, with respect to their activation, stability, and localization, are known to be regulated
107 by SUMOylation. (Gostissa et al., 1999; Lin et al., 2016; Yang et al., 2020; Z. Zhou et al., 2016)
108 Components of the SUMOylation machinery are overexpressed in SCRC and are associated with
109 poor patient prognosis (Du et al., 2016; Liu et al., 2023; Z. Sheng et al., 2025). However, it
110 remains underexplored in CAC to date. Since chronic inflammation in IBD is the primary driver
111 of CAC development, we hypothesized that SUMOylation contributes directly or indirectly to
112 CAC progression. In this study, we demonstrate a dynamic expression pattern of deSUMOylase
113 SENP5 and its prominent interacting partner Coronin1A, an actin-binding immune cell-specific
114 protein, particularly in chronically inflamed regions compared with polyp regions. Coronin1A

maintains the canonical TGF-β pathway and thus supports TGF-β-mediated M2 macrophage polarization and modulation of the tumor microenvironment in CAC.

Results:

• Dynamic expression pattern of SENP5 in chronic colitis and colitis-associated colorectal cancer (CAC)

To test the possible role of the SUMOylation machinery in CAC, we employed the previously reported AOM-DSS mice model of CAC (Arnesen et al., 2021). Briefly, 4 mice were included in each group: Control, Chronic colitis (hereafter referred to as CC), and the CAC. After intraperitoneal administration of azoxymethane (AOM) at 10mg/kg to the CAC group, 1% Dextran sulphate sodium (DSS) was given in their drinking water for alternate weeks for 14 weeks to the CAC and CC groups. In contrast, control mice received normal drinking water throughout the experiment. (Fig. 1A). The animals were monitored throughout the experiment, including constant recording of their body weight (Fig. 1B). Post-experimental treatment regimen, the animals were euthanized, and relevant organs were harvested. The successful establishment of the CAC model was evident by the presence of multiple polyps in the distal colon of the CAC group.

In contrast, the rest of the colon in the CAC (hereafter referred to as Non-polyp) and CC exhibited a pronounced morphological signature of chronic inflammation, characterized by reduced body weight and colon length (Fig. 1 B and C), along with enhanced splenomegaly (Fig. 1D). Histopathology of colon revealed marked infiltration of immune cells along with other signs of chronic inflammation and malignancy in CC and CAC polyps, respectively (Fig. 1E). qRT-PCR-based analysis confirmed significant upregulation of C-Myc in the polyp region (38±5.074), followed by the non-polyp region (22.83±4.642), confirming the development of malignancy in the CAC group. (Fig.S1 A). To test the involvement of SUMOylation in CAC, the abundance of SUMO1 and SUMO2/3 conjugated proteins (hereafter referred to as SUMOylome) in CC and polyp tissue lysates was examined. Compared to the control group, a detectable change in SUMO1 SUMOylome and a pronounced alteration of SUMO2/3 SUMOylome were observed in lysates from both CC and polyps (Fig.1F). An accumulation of free SUMO1 was observed in CC and polyp tissue lysate.

144 In contrast, no comparable accumulation of SUMO2/3 was observed. To investigate
145 possible involvement of deSUMOylases in this process, qRT-PCR-based expression analysis of
146 deSUMOylases was carried out. Notably, expression of SENP1, SENP2, SENP3, SENP6, and
147 SENP7 remained unchanged, while SENP5 showed a significant increase in expression in the CC
148 (2.61±0.15) and non-polyp regions (2.38±0.25) of CAC. Intriguingly, in stark contrast, SENP5
149 expression was downregulated in the CAC polyps (-2.8± 0.15) (Fig. 1G). We validated SENP5
150 expression dynamics in AOM-DSS mice tissue lysate by immunoblotting (Fig. 1H).
151 Furthermore, the relevance of this finding was investigated in actual CAC patient specimens
152 obtained from the Gastroenterology and Nutrition clinic (AIIMS, Delhi). Biopsies of CAC (N=15),
153 SCRC (N=9), and irritable bowel syndrome (IBS)(N=10) were included in this study. SUMO1 and
154 SUMO2/3 SUMOylome was examined in CAC patient tissue lysates. Consistent with the above
155 findings, a notable alteration in both SUMO1 and SUMO2/3 SUMOylome was observed. The
156 SUMO2/3 SUMOylome was more drastically affected. Moreover, consistent with the AOM-DSS
157 model, increased free sumo was observed in patient tissue lysates (Fig.1I). Furthermore,
158 expression of SENP5 in CAC patient specimens was also downregulated (~2.06 ± 0.50-fold) (Fig.
159 1J). Interestingly, in stark contrast, SENP5 was upregulated in sporadic colorectal cancer patient
160 samples (hereafter referred to as SCRC) (Fig. 1J). Immunoblots of SENP5 in CAC patient tissue
161 lysates also revealed reduced expression compared to healthy controls (Fig. 1K).
162 Additionally, $Apc^{+/-}$ and $Apc^{+/+}$mice were used to develop SCRC (Ren et al., 2019). The animals
163 were administered 2% DSS for 1 week, followed by 14 weeks of incubation to induce
164 tumorigenesis (Fig. S1B). At the conclusion of the experiment, mice were euthanized, and colons
165 were harvested. Prominent polyps were present at the distal end of the $Apc^{+/-}$ mice colon (Fig.S1C).
166 Tissue lysates from the control colon, as well as the polyp and non-polyp regions of $Apc^{+/-}$, were
167 probed for SENP5 by immunoblotting.
168 Notably, upregulated expression of SENP5 was observed in the polyp region compared to the
169 healthy control and non-polyp region (Fig.1L). Our findings of SENP5 in SCRC patients and the
170 murine model ($Apc^{+/-}$) are consistent with the previous report showing that upregulated SENP5 in
171 SCRC plays a key role in DNA damage repair (Liu et al., 2023). These results clearly indicated a
172 key difference between SCRC and CAC in SENP5 function. The marked difference in SENP5
173 expression between polyps and non-polyps in the CAC model prompted us to investigate the

mechanism in greater detail. To understand the regulatory mechanism driven by SENP5, we conducted SENP5 interactome analysis.

- **Altered Interactome of SENP5 in chronic colitis and colitis-associated colorectal cancer (CAC)**

The interactome of SENP5 was investigated by performing Co-IP of tissue lysates from control, chronic colitis, non-polyp, and polyp regions of the AOM-DSS mouse model, followed by MS/MS analysis (n=3). An IgG isotype control antibody was used as a negative control. (Fig. 2. A) Pull-down proteins were analyzed by high-resolution tandem mass spectrometry (MS/MS) using a quadrupole time-of-flight (qTOF) mass spectrometer. Initially, 2315 proteins were identified across all four groups; after contaminant removal, the remaining 1,884 proteins were subjected to further analysis. The MaxQuant platform was used to quantify the identified proteins. Peptides found in the isotype control IgG were manually subtracted from the pull-down samples during subsequent analysis. Differential proteome of control, chronic colitis (CC), non-polyp, and polyp obtained from intensity-based absolute quantification illustrated in a Venn diagram (Fig. 2 B), revealing 460 proteins in control, 508 in CC, 510 in non-polyp, and 406 in polyp. Out of which 29 proteins were unique to control, 43 were unique in CC, 74, and 21 were unique in non-polyp and polyp, respectively. Notably, 282 proteins are present in all four conditions. In the identified set of proteins, we detected SUMO2. Recent structural studies have demonstrated the active, specific interaction between SENP5 and SUMO2, underscoring the robustness of our interactome approach. (Sánchez-Alba et al., 2025) A list of proteins identified across all four conditions is provided in the supplementary.

Differential enrichment analysis of SENP5-interacting proteins showed a distinct pattern across all four conditions. 114 proteins were enriched, and 15 proteins were depleted in their interaction with SENP5 significantly in the non-polyp region. Under CC,39 proteins were enriched with SENP5, and 13 proteins were depleted in their interactions with SENP5.

In the polyp group, 132 proteins showed reduced interaction with SENP5, and five proteins showed enrichment with SENP5. Here, the definition of significance is a fold change greater than two and a p-value <0.05.

204 To understand the biological significance of proteins differentially enriched for SENP5,
205 Gene Ontology (GO) pathway analysis was performed on enriched and depleted proteins across
206 all three disease conditions. Pathway enrichment significance was assessed using hypergeometric
207 and multiple test correction at FDR less than 0.05. The *p*-values are corrected for multiple testing
208 within each category using the Benjamini-Hochberg procedure. As both non-polyp and chronic
209 colitis represent states of chronic inflammation, we chose non-polyp samples for differential GO
210 pathway enrichment analysis. In this enrichment analysis, polyp and non-polyp samples were
211 independently compared with the control to identify pathways associated with the tumor and the
212 adjacent non-tumor area.
213 Molecular function and cellular component-based GO pathway analysis revealed a profound
214 enrichment of SENP5-interacting proteins with actin filament binding or actin binding functions,
215 and the actin cytoskeleton cellular component, particularly in the non-polyp region. While the
216 enrichment of these proteins was very feeble in the polyp region (Fig. 2C) (Fig.S2. A). These
217 results suggest that SENP5 displays a more pronounced interaction with proteins involved in Actin
218 binding or linked to the actin cytoskeleton in the non-polyp region. In contrast, such interactions
219 are markedly reduced in polyp regions. From the significantly enriched list of proteins falling
220 under the Actin binding or Actin filament binding function, we shortlisted proteins Coro1A, Tmp4,
221 Myh9, Col6A3, and Dync1h1, based on their roles in cancer or disease progression, as well as the
222 presence of prominent SUMO-binding or SUMO-interacting sites (Fig.2D). The differential
223 enrichment of selected genes was visualized on volcano plot, revealing their prominent enrichment
224 in the non-polyp and CC region and abolished enrichment in polyp region. (Fig 2. E) (Fig.S2.B) It
225 underlines a shift in the interactome of SENP5 from the non-polyp to the polyp region, indicating
226 a crucial role of these proteins in disease progression. Among the selected candidates, Coro1A
227 (Coronin 1A) stood out as the most prominent pick. The immune cell-specific protein Coro1A is
228 known to interact with filamentous Actin and regulate actin dynamics by interacting with the
229 Arp2/3 complex (Galkin et al., 2008; Humphries et al., 2002). Coronin 1A plays a role in T-cell
230 maturation, as well as T-cell receptor-based signaling, neutrophil trafficking, and immune
231 deficiency (Castro-Castro et al., 2011; Mueller et al., 2008; Pick et al., 2017; Stocker et al.,
232 2018).Additionally, there is multiple evidence of Coronin1A involvement in immunological
233 pathways associated with chronic inflammation and its related manifestations, such as lung
234 fibrosis, lupus nephritis, and non-alcoholic steatohepatitis (NASH), and autoimmune diseases such

as multiple sclerosis. (X. Deng et al., 2024; Nicolaou et al., 2020; Principi et al., 2023; Siegmund et al., 2016)In light of these, we set forth to investigate the role of Coronin-1A in CAC progression.

- **Coro1A is an interactor of SENP5**

The interactome analysis enabled us to identify Coronin-1A (hereafter referred to as Coro1A) as an interactor of SENP5. Coro1A-SENP5 interaction was scrutinized using a co-immunoprecipitation (Co-IP) assay. The immunoblot clearly showed strong binding of Coro1A to SENP5, particularly in tissues from CC and non-polyp areas of CAC mice (Fig. 3A). Furthermore, the expression profile of Coro1A was examined in the AOM-DSS mouse model. An elevated expression of Coro1A in CC and, interestingly, in the non-polyp region of CAC was observed. In contrast, in the polyp, much lower expression was detected (Fig. 3B). These results were validated in a murine colitis genetic model using IL10$^{-/-}$ mice. IL10$^{-/-}$ mice spontaneously develop colitis (Gunasekera et al., 2020).To establish a synchronized CAC in this background, the animals were administered AOM (10mg/kg) intraperitoneally, followed by 7 alternating cycles of low-dose 1% DSS (Fig. S3A). Post-treatment, the mice were euthanized, and the relevant organs were harvested. Notably, we did not detect any polyps in CAC mice, despite probing the colons of CC and CAC mice for Coro1A expression. Immunoblotting of colon lysates revealed a pronounced increase in Coro1A expression in both CC and CAC tissues compared to untreated controls (Fig. 3C), confirming that Coro1A upregulation is not restricted to a single chronic colitis model but is found in a broad range of chronic colitis models. Next, the expression of Coro1A was analyzed in an acute colitis mouse model. The acute colitis model was developed as described by (Suhail et al., 2019)(Fig. S3B). Coro1A expression was not modulated in the acute colitis mouse model (Fig. S3C). These results implied that Coro1A induction is limited to chronic colitis. Additionally, we probed Coro1A in colonic lysates from the Apc$^{+/-}$ SCRC model and found no significant differences in its expression; however, a trend of decreasing Coro1A expression was observed in the non-tumor adjacent area and the tumor area. (Fig. S3D). Next, the relevance of Coro1A expression in chronic gut inflammation was examined in human colon biopsies. Biopsy samples from UC (N=5) patients also showed significantly elevated Coro1A expression compared to those from IBS patients (N=4), as shown by immunoblot (Fig. 3D). These findings suggest a potential role for Coro1A in the development of colitis-associated cancer.

266 Together, these findings indicate that Coro1A upregulation is a feature specific to chronic
267 inflammatory settings and inflammation-driven tumorigenesis, rather than sporadic tumor
268 development. To gain insights into the subcellular localization of Coro1A, immunohistochemistry
269 (IHC) was performed. Enhanced expression of Coro1A was observed in infiltrating immune cells
270 in the CC and non-polyp areas compared with the control. Coro1A protein was detected in the
271 polyp region, though with less intensity as compared to CC and non-polyp (Fig. 3E). Furthermore,
272 these observations were confirmed in patient biopsy-derived archived slides, which showed a
273 consistent increase in Coro1A expression in infiltrating immune cells in UC and the adjacent
274 inflamed CAC tumor area compared to the IBS control. Notably, a prominent presence of Coro1A
275 in the CAC tumor, albeit less than in non-polyp and UC, was observed (Fig. 3F). These results
276 reveal that Coro1A is uniformly present in immune cells and is consistently upregulated during
277 chronic inflammation. However, an unusually high abundance of Coro1A in the non-polyp region
278 of CAC prompted us to investigate its role in CAC development.

279• **Absence of Coro1A confers resistance to CAC development in mice**

280 To understand the relevance of increased Coro1A expression in infiltrating immune cells, we
281 employed Coro1A KO mice (hereafter, Coro1A^{KO}). Coro1A ^{KO} mice were generated in the
282 laboratory of J.M. Penninger (IMBA, Vienna) by using *a Cre/LoxP*-based gene-targeted strategy.
283 The deleted region encompasses the entire coding sequence after exon 1 (Kaminski et al., 2011).
284 Complete KO of the Coro1A gene was confirmed by immunoblot of Coro1A from colonic tissue
285 lysates of Wild-type mice (WT) and Coro1A^{KO} mice (Fig. S4A and B).
286 To understand the relevance of Coro1A in CAC development, WT and Coro1A^{KO} were subjected
287 to the AOM-DSS treatment as described in Fig.1A. A schematic representation of the experimental
288 design, which lasted for 14 weeks, is shown in Fig. 4A. The animals were monitored throughout
289 the experiment, including constant recording of their body weight (Fig. S4C). Post experiment,
290 mice were euthanized, and the colon, spleen, and other relevant organs were harvested. Gross
291 morphological parameters were evaluated to compare the extent of disease development in WT
292 and Coro1A^{KO} mice. The length of the colon and splenomegaly were analyzed in both CC and
293 CAC groups across both genotypes. A considerable reduction in colon length of CC and CAC
294 categories of each genotype was observed, indicating the establishment of colitis (Fig. S4.D). No
295 significant differences were observed in the respective sub-categories between the WT and

296 Coro1A^{KO} groups. However, the colon from WT mice in the CAC group showed a wider distal
297 end than those in all other groups from both genotypes, suggesting the possible presence of polyps.
298 In line with this, the colon from WT mice in the CAC group showed the development of multiple
299 polyps, a feature absent in Coro1A^{KO} mice (Fig. 4B). Moreover, there was an evident
300 splenomegaly in the case of the CAC^{WT} group, which was more pronounced in the WT as
301 compared to their KO counterparts (Fig. S4E). H&E staining of colonic tissue sections from WT
302 and Coro1A^{KO} mice across all conditions was carried out. Sections from CC^{WT} and CAC ^{WT} groups
303 showed prominent markers of colitis and cancer, including high-grade dysplasia, mild field effect,
304 collagen deposition, distorted crypt architecture, a widened muscularis layer, and moderate
305 inflammation with immune cell infiltration.
306 In contrast, the CC and CAC groups of Coro1A^{KO} mice exhibited no or very low-grade dysplasia,
307 field effect, crypt distortion, and collagen deposition, accompanied by prominent immune cell
308 infiltration and inflammation, as indicated by the histopathology score (Fig. 4C and Fig. S4F).
309 Further Sirius red staining showed prominent collagen deposition in CC^{WT} and CAC $^{WT.}$In contrast,
310 Coro1A^{KO} mice exhibited strikingly less collagen deposition in CC and CAC, indicating attenuated
311 extracellular matrix (ECM) deposition in Coro1A ^{KO} mice compared with WT. (Fig.4D). The lack
312 of polyp formation and absence of adenocarcinoma in Coro1A^{KO} CAC mice necessitated the
313 investigation of molecular markers associated with proliferation, inflammation, extracellular
314 matrix (ECM) deposition, and epithelial-to-mesenchymal transition (EMT) in colonic tissue
315 lysates from both genotypes across all samples.
316 Both Ki-67, a proliferation marker, and C-Myc, a protooncogene, were markedly elevated in CC
317 ^{WT}(2.973±0.6296; 2.363±0.3234) and CAC^{WT} (6.600±0.05003; 5.050±0.3396) mice, whereas they
318 were downregulated in the CC^{Coro1aKO}(-2.723±1.513;-1.987±0.7342) and CAC^{Coro1aKO}(-
319 3.137±0.2270; -1.980±0.2722) counterparts (Fig.4.E). Expression of E-Cadherin was dramatically
320 downregulated in CC^{WT}(-29.10 ± 9.570) while the CAC^{WT} group showed marked upregulation
321 (14.22±1.650). Interestingly, both features were completely absent in the Coro1AKO groups. This
322 pattern of E-cadherin expression aligns with recent reports of elevated E-cadherin expression in
323 solid tumors (Burandt et al., 2021; Rodriguez et al., 2012) (Fig. S4G). Cox2, a pro-inflammatory
324 marker, was downregulated significantly in CC(-8.043±2.687) and CAC(-4.457±1.057) of WT,
325 whereas Coro1A^{KO} CC and CAC showed very subtle changes. Anti-inflammatory and pro-wound
326 healing marker-Arginase-1(Arg1) was markedly upregulated in CAC^{WT}(6.700±0.6255), and

327 downregulated in CC^{WT}(-3.600±0.5615). In the $Coro1A^{KO}$ CC and CAC mice, this pattern was
328 observed, but with significantly lower values (-2.097±0.3783; 1.847±0.8995) (Fig.4F). Together,
329 these results indicate a tendency toward higher cell proliferation, higher oncogenic, excessive
330 wound healing, anti-inflammatory, and lower pro-inflammatory activity in WT mice; however,
331 these features were either absent or diminished in $Coro1A^{KO}$ mice.
332 Further analysis of ECM remodeling genes, including Fibronectin, α-SMA, and Col1A1, revealed
333 significant upregulation in WT mice from the CC(4.183±0.6451; 10.04±3.008; 4.227±0.9239) and
334 CAC(5.233±0.04910; 2.633±0.9347; 6.157±0.6388) groups. In contrast, their expression was
335 comparatively lower in respective groups of $CC^{Coro1A\ KO}$ (-4.727±1.916; -2.898± 0.3824; 0.5067±
336 0.1074) and $CAC^{Coro1AKO}$(-4.370±1.344;-2.513±0.1995;1.100±0.04933) mice (Fig.4G).
337 Consistently, EMT-associated transcription factors SNAIL and SLUG were also upregulated in
338 CAC^{WT} (7.072±1.964; 24.33± 5.503) relative to the counterpart $Coro1A^{KO}$ tissues group (-7.223±
339 0.2706; 0.5819± 0.3946) (Fig.S4H). Additionally, p53 was upregulated in CAC^{WT} (1.490± 0.4539)
340 compared to CC^{WT} (-0.1667±0.3820) and both Coro1A KO conditions(-0.300±0.1102;
341 0.1367±0.1637). It is consistent with reports of p53 overexpression in UC, CAC, and sporadic
342 colorectal cancer (Khursheed et al., 2024; Lu et al., 2017; Popp et al., 2016) (Fig. 4H). Altogether,
343 these findings demonstrate that molecular footprints associated with proliferation, inflammation,
344 ECM remodeling, and EMT are pronounced in WT mice, correlating with their increased
345 susceptibility to CAC development compared to $Coro1A^{KO}$ mice.
346

347• **Increased expression of Coro1A is associated with M2 macrophages**

348 To understand the immune cell type that shows enhanced Coro1A expression in chronic
349 inflammatory conditions and plays a crucial role in CAC development, we analyzed immune cells
350 isolated from the lamina propria of control, CC, non-polyp, and polyp tissues from WT mice by
351 flow cytometry. Flow cytometry was performed using predefined gating strategy, as shown in Fig.
352 S5A. Analysis revealed, in contrast to the control group, a marked increase in the number of
353 $F4/80^+$ and $CD11b^+$ macrophages in CC, non-polyp, and polyp regions (Fig. 5A and B), while the
354 neutrophil count ($CD45^+$ and $Ly6G^+$) was decreased in the CC and non-polyp regions, but
355 unexpectedly elevated in the polyp tissue (Fig S.5 B and C). To confirm whether Coro1A is
356 increased in infiltrating macrophages, the Median fluorescence intensity (MFI) of Coro1A during

357 flow cytometric analysis was calculated. MFI analysis revealed increased abundance of Coro1A
358 in infiltrating macrophages across all three conditions (Fig. 5C). While decreased abundance of
359 Coro1A was observed in neutrophils in the CC and non-polyp regions, it was strikingly elevated
360 in the polyp region (Fig. S5D). Under prolonged chronic inflammation, dynamic macrophages
361 exhibit remarkable plasticity, adapting to either a pro-inflammatory (M1) or an anti-inflammatory
362 (M2) state. Overall, macrophages, particularly anti-inflammatory, pro-tumorigenic M2
363 macrophages, utilize a variety of signaling cascades to promote CAC. (Hardbower et al., 2017;
364 Wang et al., 2023; Yuan et al., 2021 Suarez-Lopez et al., 2018) Further analysis demonstrated a
365 gradual enrichment of(Arg^+-1) M2-like macrophages in CC, non-polyp, and polyp regions
366 compared to the $iNOS^+$ M1-like macrophages (Fig. 5D). A significantly higher M2 (Arg^+) /M1
367 ($iNOS^+$) ratio was seen in the area of non-polyp and polyp (Fig.5E). Subsequent analysis revealed
368 increased MFI of Coro1A is associated with Arg^+ M2 macrophages (Fig. 5F), whereas $iNOS^+$ M1
369 macrophages did not show such a trend (Fig. S5E).

370 To gain a mechanistic understanding of these observations, *in vitro* experiments were conducted.
371 Macrophages were treated with IL-4 and TGF-β to induce an M2-like phenotype as previously
372 reported (Stein et al., n.d.)(Zhang et al., 2016).Notably, exposure to these two cytokines increased
373 intracellular Coro1A levels (Fig. 5 G and H). This phenotype was accompanied by the upregulation
374 of several canonical M2 macrophage markers 14 hours post cytokine treatment (p.c.t) (Fig. 5I and
375 J).

376 Considering TGF-β being one of the inducers of Coro1A, the levels of TGF-β in the tissue lysates
377 of the AOM-DSS murine model were verified. Found an increased abundance of TGF-β in the CC
378 and CAC colon of IL-$10^{-/-}$ AOM-DSS mice, as determined by ELISA, underscoring the connection
379 between TGF-β and Coro1A signaling (Fig. 5 K). Collectively, these results suggest that Coro1A
380 is involved in the function of M2-like macrophages and thus modulates the tumor
381 microenvironment.

382• **Coro1A interacts directly with the TGF-βRI and controls TGF-β-mediated M2 macrophage**
383 **polarization**

384 Previous reports have implicated Coro1A in regulating TGF-βRI and in the differentiation of Th17
385 $CD4^+$ T cells (Kaminski et al., 2011). Based on this, we set forth to investigate the possible
386 mechanism by which Coro1A crosstalks with TGF-β-signaling in macrophages. Co-IP analyzed

387 the potential interaction between Coro1A and TGF-βRI. RAW264.7 cell lysate was pulled down
388 with an anti-Coro1A antibody, followed by immunoblotting against TGF-βRI. A direct interaction
389 of Coro1A with TGF-βRI was evident (Fig. 6.A). Furthermore, structured illumination microscopy
390 (SIM) revealed a direct interaction between TGF-βRI and Coro1A, as evidenced by strong
391 colocalization signals (Fig.6B). Furthermore, interaction of Coro1A was not restricted to TGF-β
392 RI; it also interacted with TGF-β RII (Fig. S. 6A).

393 The role of Coro1A in macrophage function was next assessed. J774 macrophages stably knocked
394 down for Coro1A (hereafter referred to as J774 $^{\text{Coro1A KD}}$) were used (Fig. 6C) and (Fig.S6B). The
395 interaction between Coro1A and TGF-βRI was validated in J774 ^{WT} and J774 $^{\text{Coro1A KD}}$ cells by
396 antibody-based pull-down. The blots revealed interaction of Coro1A and TGF-βRI in J774 ^{WT} cells
397 but not in J774 $^{\text{Coro1A KD}}$ cells (Fig. 6D).
398 Under the basal level, there is no significant change in the expression of prototypical M2 markers
399 like Arginase-1, IL-10, master regulator of M2 macrophage markers SNAIL, and TGF-βRI, in
400 J774^{WT} and J774$^{\text{Coro1A KD}}$ cells. Upon stimulation with TGF-β, J774^{WT} exhibited strong induction
401 of M2 markers Arginase-1 (6.877±1.372) and SNAIL (5.395±0.856), whereas this phenotype was
402 severely blunted in J774$^{\text{Coro1A-KD}}$ cells (Arginase-1 0.5067±0.0898, SNAIL 2.201±1.164)
403 measured by qRT-PCR (Fig.6E, Left and Right). In line with these changes in gene expression,
404 the secretion of the anti-inflammatory cytokine IL-10 was significantly higher in J774^{WT} cells
405 (55.83±14.29) after TGF-β stimulation; however, in J774 $^{\text{Coro1A KD}}$ cells treated with TGF-β, IL-10
406 secretion was considerably lower (6.904±15.23). (Fig. 6F). Furthermore, Arginase-1-positive cells
407 were quantified using Flow Cytometry, revealing that J774 ^{WT} cells showed a pronounced response
408 to TGF-β stimulation, with increased Arginase-1-positive cells (27.67±9.615), whereas J774 $^{\text{Coro1A}}$
409 ^{KD} cells failed to respond to TGF-β with the same efficiency (4.667±2.749). (Fig. 4G). Considering
410 reduced expression of Arginase, SNAIL, and less secretion of IL-10, the expression of TGF-βRI
411 in J774 ^{WT} and J774 $^{\text{Coro1A KD}}$ cells was examined. TGF-βRI showed comparable basal levels of
412 expression in both J774 ^{WT} and J774 $^{\text{Coro1A KD}}$ cells. Upon TGF-β exposure, it was upregulated in
413 both cell types (1.993±0.1658; 1.513±0.4103) (Fig. 6H). This indicates that TGF-β receptor
414 transcription is intact in J774 $^{\text{coro1A KD}}$ cells, and that impaired signaling likely arises from defects
415 at the protein level. Mechanistically, in the canonical TGF-β signaling pathway, the activated TGF-
416 β receptor phosphorylates SMAD2/3, which form a complex with SMAD4 and translocate to the
417 nucleus to drive transcription of target genes (Nakao & Imamura, 1997). Accordingly, TGF-β

418 stimulation increases the nuclear accumulation of pSMAD2/3 in cells responding to the TGF-β
419 trigger, as compared to less or non-stimulated cells. In line with the above observation, J774 ^{WT}
420 cells exposed to TGF-β showed enhanced nuclear accumulation of SMAD3 as compared to J774
421 $^{Coro1A\ KD}$ cells (Fig. 6I). Furthermore, bone marrow-derived macrophages (hereafter referred to as
422 BMDMs) isolated from WT mice showed promising accumulation of pSMAD3 in their nucleus
423 on TGF-β stimulation, whereas Coro1A^{KO} mice-derived BMDMs showed impaired nuclear
424 accumulation of pSMAD3, as shown by immunofluorescence microscopy (Fig. 6J). Together,
425 these findings demonstrate that Coro1A is a critical regulator of TGF-β-mediated SMAD3
426 activation in macrophages and, consequently, of TGF-β-mediated macrophage polarization.

427

428• **Coro1A is required for the stability of TGF-βRI**

429 To understand the relevance of Coro1A interaction with TGF-βRI, TGF-βRI expression was
430 investigated in stable J774 $^{Coro1A\ KD}$ cells. A significant decrease in TGF-βRI protein expression
431 levels was seen in J774$^{Coro1A\ KD}$ cells compared to J774^{WT} cells (Fig. 7A). Additionally, TGF-βRI
432 expression was validated in BMDM^{WT} and BMDM $^{Coro1A\ KO}$ by confocal microscopy. A significant
433 reduction in FITC-labelled TGF-βRI fluorescence intensity in BMDM $^{Coro1A\ KO}$ was observed, as
434 compared to BMDM ^{WT} (Fig. 7B). Furthermore, to assess overall TGF-βRI-mediated signaling in
435 J774 $^{Coro1A\ KD}$ cells, pAKT/AKT level, as one of the immediate downstream readouts of the TGF-
436 β signaling, was examined. TGF-β-induced pAKT level was markedly reduced in J774 $^{Coro1A\ KD}$
437 cells as compared to J774 ^{WT} cells, indicating impaired SMAD-independent signaling as well in
438 J774 $^{Coro1A\ KD}$ cells (Fig. 7C). TGF-β signaling is autoregulatory; the activation of intact TGF-β
439 receptors induces *TGFB1* transcription, leading to enhanced precursor synthesis and the release of
440 mature TGF-β into the supernatant. Conversely, impaired TGF-βR signaling lowers both
441 intracellular precursor levels and the secreted TGF-β (Deng et al., 2024; Massagué, 2012).ELISA
442 and immunoblot verified autoregulatory secretion of TGF-β in cell supernatant from J774 ^{WT} and
443 J774 $^{Coro1A\ KD}$ cells. A considerably lower concentration of TGF-β appeared in the cell supernatant
444 collected from J774 $^{Coro1A\ KD}$ cells as compared to J774 ^{WT} cells (Fig. 7D). These findings were
445 further supported by immunoblot analysis of secreted TGF-β in the supernatant, confirming a
446 reduced secretion of TGF-β from J774 $^{Coro1A\ KD}$ cells (Fig.S6C). Further, the TGF-β level in the
447 tissue lysate of WT and Coro1A ^{KO} CAC mice model was measured using ELISA. TGF-β levels

448 were upregulated in CC ^{WT} and CAC ^{WT} compared to both WT Control and their respective Coro1A
449 ^{KO} counterparts, indicating a marked reduction in TGF-β synthesis in Coro1A ^{KO} mice. (Fig. 7E).
450 Next, the mechanism by which Coro1A safeguards TGF-βRI from degradation was investigated.
451 Previous studies have shown that Coro1A decorates signaling endosomes of the neuronal growth
452 factor (NGF)-tropomyosin-related kinase type-1 (TrkA) once it is internalized within the neuronal
453 cell body from lysosomal degradation. (Suo et al., 2014).
454 We hypothesized that the TGF-β-TGF-βRI complex, upon internalization, is protected from
455 degradation by Coro1A in macrophages. In line with this, bafilomycin-A1-mediated blocking of
456 lysosomal acidification rescued the TGF-βRI level in J774 $^{Coro1A\ KD}$ cells as compared to untreated
457 J774 $^{Coro1A\ KD}$ cells (Fig.7F), whereas blocking proteasomal degradation by MG-132 treatment
458 resulted in no change in TGF-βRI expression in J774 $^{Coro1A\ KD}$ cells. (Fig.S6D). As a positive
459 control, p62 accumulated under bafilomycin-A1 treatment, while polyubiquitinated proteins were
460 enriched following MG-132 treatment, confirming effective lysosomal and proteasomal inhibition,
461 respectively (Fig. S6E and F). Furthermore, colocalization of FITC-labelled TGF-βRI(Green) with
462 Lysotracker (Red) in BMDM ^{WT} and BMDM $^{Coro1A\ KO}$ revealed a higher degree of TGF-βRI
463 accumulation within lysosomes of BMDM $^{Coro1A\ KO}$, as observed by strong yellow color puncta
464 (Fig. 7G). Together, these results suggest that in the absence of Coro1A, canonical and non-
465 canonical TGF-β signaling are hampered because TGF-β-TGF-βRI signaling endosomes are
466 predominantly targeted for lysosomal degradation.
467
468 • **Coro1A utilizes the calcium-calcineurin signaling pathway to protect TGF-βRI from**
469 **degradation.**
470 Previous reports have demonstrated that Coro1A-mediated calcium influx protects NGF-TrkA
471 signaling endosomes and *M. tuberculosis* phagosomes from lysosomal degradation (Jayachandran
472 et al., 2007; Mueller et al., 2008; Suo et al., 2014).
473 To test whether Coro1A utilizes calcium ion influx to stabilize TGF-β-TGF-β RI signaling
474 endosomes from lysosomal degradation, RAW 264.7 cells were treated with cell-permeable
475 calcium chelator 1,2-bis(o-aminophenoxy) ethane-N, N, N, N-tetraacetic acid, tetraacetoxymethyl
476 ester (BAPTA-AM) and assessed the TGF-βRI level by immunoblotting. Notably, the level of
477 TGF-βRI in RAW264.7 cells treated with BAPTA-AM was significantly lower than that in
478 untreated controls (Fig. 8A). The result phenocopied the finding observed in the Coro1A-depletion

479 condition. (Fig.7A). Moreover, increasing calcium concentration in J774 $^{Coro1A\ KD}$ cells using
480 calcium ionophore Ionomycin partially rescued TGF-β RI level as compared to J774 $^{Coro1A\ KD}$ cells
481 (Fig. 8B). Taken together, these data suggest stability of TGF-βRI is directly linked to the ability
482 of Coro1A to induce calcium release. Provided that *M. tuberculosis* (Jayachandran et al., 2007)
483 and NGF-TrkA signaling endosomes (Suo et al., 2014) utilize calcium ion-activated calcineurin
484 phosphatase to evade lysosomal degradation, it was speculated that TGF-β RI signaling endosomes
485 may employ a similar mechanism. In RAW264.7 cells, potent calcineurin inhibitors, Cyclosporin
486 A (CsA) and FK506, were added to test whether inhibiting calcineurin phosphatase results in
487 degradation of TGF-β RI. Similar to BAPTA-AM, treatment with CsA and FK506 resulted in a
488 significant reduction in TGF-βRI expression (Fig. 8C and D). Collectively, these results suggest
489 that Coro1A, associated with TGF-β-TGF-β RI signaling endosomes, utilizes the calcium-
490 calcineurin signaling pathway to protect TGF-β RI signaling endosomes from lysosomal
491 degradation in the macrophages.
492
493• **SUMO2/3 governs the stability of Coro1A**
494 Since Coro1A was identified in this study as an interactor of deSUMOylase SENP5, we tested
495 whether Coro1A is SUMO-modified. Co-immunoprecipitation was performed using anti-
496 SUMO2/3 antibody in J774^{WT} cell lysates, followed by immunoblotting against Coro1A.
497 Interestingly, Coro1A was detected in the SUMO2/3 pull-down (Fig. 9A, bottom). Moreover, the
498 Coro1A band appeared at its usual molecular weight, with no shift in molecular weight detected,
499 indicating that Coro1A itself does not undergo SUMOylation. Surprisingly, in reverse Co-IP with
500 Coro1A, SUMO2/3 bands appeared in the range of 75 kDa-150 kDa, suggesting that Coro1A may
501 interact with already SUMOylated proteins (Fig. 9A, Top). In line with previous findings on
502 Coro2A, where it interacts with SUMOylated Liver X-receptors (LXRs) through SUMO-
503 interacting motifs (SIM)(Huang et al., 2011). It was speculated that Coro1A may utilize its SIM
504 site to interact with SUMOylated proteins. SIM, a conserved hydrophobic amino acid (V/I V/I X
505 V/I), followed by acidic residues, enables the protein to interact with other SUMOylated proteins,
506 influencing their stability, localization, and downstream signaling.(Kerscher, 2007; Song et al.,
507 2004).
508 Using GPS-SUMO and JASSA (Beauclair et al., 2015; Gou et al., 2024),we identified potential
509 SIM sites in Coro1A; however, sites recognized by both tools with high scores were prioritized

510 (Fig.9 B). SIM Sites 124-128, 155-159, and 167-171 were selected for further study. These
511 findings raise two questions: the functional relevance of Coro1A SIM sites and the identity of the
512 protein undergoing SUMOylation to which Coro1A interacts via its SIM site. Conservation of the
513 chosen SIM sites was analyzed using a multiple-sequence alignment across different species (Fig.
514 S7A). To identify the critical SIM site required for Coro1A to function and the relevance of SIM-
515 SUMO interaction, SIM sites were perturbed by performing Site-Directed Mutagenesis (SDM) by
516 replacing the hydrophobic Valine (V) residue with positively charged Lysine (K) residue; this
517 change is expected to disrupt the SIM-SUMO interaction, as established by Song et al. (2004)
518 (Fig.S7 B).
519 To understand the fate of these mutants, Coro1A-GFP ^{WT} and SIM mutants (Coro1A-GFP ^{V124K},
520 Coro1A-GFP ^{V155K}, and Coro1A-GFP ^{V167K}) were transfected into RAW264.7 cells, and protein
521 expression was analyzed on an immunoblot. A marked reduction in the expression of Coro1A-
522 GFP^{V155K} was observed on immunoblot (Fig. 9C). To validate the above finding, the
523 hydrophobicity of the SIM site in the Coro1A ^{V155K} mutant was replenished by replacing lysine
524 (K) with alanine (A), resulting in partial rescue of the Coro1A-GFP protein (Fig. 9D).
525 Furthermore, confocal microscopy of RAW264.7 cells transfected with Coro1A-GFP ^{WT} and
526 Coro1A SIM mutants showed that neither mutation altered localization nor induced aggregation
527 in Coro1A. However, Coro1A-GFP ^{V155K} showed a marked reduction in GFP fluorescence
528 intensity as compared to Coro1A-GFP ^{WT} and other SIM mutants (Fig. 9E).
529 Overall, these results suggest that perturbing SIM sites affects Coro1A stability. Molecular
530 dynamics simulations were carried out between Coro1A ^{WT} and Coro1A ^{V155K} mutant using the
531 CABS-Flex 3.0 server (https://doi.org/10.1093/nar/gkaf412) to rule out the possibility of structural
532 aberration induced by the V155K mutation in Coro1A. The results showed that both the wildtype
533 and V155K mutant proteins exhibited similar dynamic behavior, indicating that the mutation does
534 not induce any significant structural aberration that could cause protein denaturation (Fig. S7C).
535 Next, SIM-SUMO interaction was disrupted independently of Coro1A by transiently knocking
536 down the only SUMO-conjugating enzyme, UBC9, in RAW264.7 cells, thereby lowering global
537 SUMOylation. Under these conditions, Coro1A expression was strikingly less. (Fig.9F). This
538 effect is restricted at the protein level, as the transcript of Coro1A was upregulated on UBC9
539 knockdown (Fig.S7D). To investigate the route of Coro1A-GFP ^{V155K} degradation, RAW264.7
540 cells transfected with Coro1A-GFP ^{WT} and ^{V155K} mutant were treated with MG-132 and

541 Bafilomycin-A1. Surprisingly, partial rescue was observed in Coro1A-GFP ^{V155K} in both
542 conditions (Fig.9G). Altogether, these results show that disruption of the SIM site or lowering
543 global SUMOylation leads to degradation of the Coro1A protein, indicating that Coro1A depends
544 on SUMO2/3 and SUMOylated target protein for stability.
545
546• **Coro1A interacts with SUMOylated Raftlin-1 through SIM interaction**
547 To identify potential SUMOylated proteins involved in the SIM-SUMO interaction with Coro1A,
548 two distinct bands of SUMO2/3, observed between 75 kD and 150 kD (Fig. 9A, Top), were
549 subjected to mass spectrometry. After subtracting proteins detected in IgG, a list of potential
550 proteins that may undergo SUMOylation was obtained (Fig. 10A).
551 From that list, Raftlin, a novel major lipid raft protein, was selected as a promising candidate to
552 undergo SUMOylation and interact with Coro1A. Previous reports have shown that Raftlin
553 controls T-cell receptor (TCR) and B-cell receptor (BCR) signaling by mobilizing calcium ions
554 (Kazuko Saeki & Akihiko Yoshimura, 2003; Saeki et al., 2009). Raftlin plays a critical role in
555 endocytosis, decorates signaling endosomes, and is detected together with Coro1A in the VEGFR2
556 interactome (Tatematsu et al., 2016; Watanabe et al., 2011a; Bayliss et al., 2020). These findings
557 indicate a close association between Raftlin and Coro1A, and, together with their functional
558 similarity, led us to select Raftlin as a potential candidate for the Coro1A SIM-SUMO interaction.
559 To test the interaction between Coro1A and Raftlin, co-immunoprecipitation (co-IP) was
560 performed using an anti-Coro1A antibody in J774 ^{WT} and J774 $^{Coro1A\ KD}$ cell lysates. Raftlin-
561 Coro1A interaction appeared in J774 ^{WT}, but not in J774 $^{Coro1A\ KD}$ (Fig. 10 B). Furthermore, their
562 interaction was validated in RAW264.7 cells, confirming its conservation across different cell
563 types (Fig. S7E). To identify potential SUMOylation sites present in Raftlin, the GPS-SUMO and
564 JASSA software tools were employed. Both software tools with high scores identified the K31 and
565 K224 sites (Fig. 10C). To narrow down on the possible SUMOylation site, an *in-silico* protein-
566 protein docking approach was employed. While docking the SUMO2 protein on the alpha fold
567 predicted structure of Raftlin, parameters like supramolecular geometry, accessibility of lysine (K)
568 residues for isopeptide bond formation with SUMO, and minimal energy score were considered.
569 Molecular docking demonstrated interaction between the di-glycine motif of SUMO2 (G-97) with
570 K31, K139, and K308 of Raftlin, with SUMO2-K31 interaction being most compact and exhibiting
571 the lowest minimum energy score (Fig. 10D). Additionally, multiple sequence alignment revealed

572 that K31 is highly conserved across different species, underlining its functional importance
573 (Fig.S7F) whereas other mentioned sites are not conserved. To test whether Raftlin undergoes
574 SUMOylation and whether K31 is the potential site of SUMO binding, SDM was performed to
575 substitute lysine (K31) with arginine (K31R), as SUMO can form an isopeptide bond with only
576 lysine and not with arginine (Rytinki & Palvimo, 2009). Next, RAW264.7 cells were transfected
577 with Raftlin ^{WT} and Raftlin ^{K31R,} along with appropriate controls, and subjected to GFP-antibody-
578 based pull-down. Immunoblot revealed a prominent interaction between Raftlin ^{WT} and SUMO2/3,
579 as well as between Raftlin ^{WT} and Coro1A. In contrast, Raftlin ^{K31R} did not interact with SUMO2/3
580 and showed a feeble interaction with Coro1A (Fig. 10E). Raftlin ^{K31R} showed comparable stability
581 to Raftlin ^{WT} as demonstrated by immunoblotting (Fig. S7G). In line with this, structured
582 illumination microscopy (SIM) demonstrated strong colocalization of Coro1A (Red) with Raftlin
583 ^{WT} (Green), which was markedly reduced with Raftlin ^{K31R} (Fig. 10F). To map the interacting
584 interface of SUMOylated Raftlin with Coro1A, a stable Raftlin-SUMO complex was docked on
585 Coro1A (PDB ID: 2AQ5). Protein-protein docking analysis indicated that SUMO interacts with
586 Coro1A through a region spanning residues 155-159 and 167-171. The SUMO-interacting
587 interface on Coro1A is highlighted in yellow (Fig.10G). Notably, these regions correspond to
588 SUMO-interacting motifs (SIMs) of Coro1A, consistent with our previous findings demonstrating
589 that SIM 155-159 is critical for Coro1A to interact with SUMO2/3 and maintain stability. Overall,
590 these results revealed that Coro1A interacts with SUMOylated Raftlin at K31 through the SIM
591 site.
592
593 **Discussion:**
594 In the current work, a screen was carried out to assess the possible involvement of SUMOylation
595 machinery components in CAC, leading to the identification of the deSUMOylase- SENP5. To
596 dissect the contribution of SENP5 in CAC, its interactome was analyzed, and Coro1A emerged as
597 an outcome. Coro1A, an actin-binding regulatory protein, is associated with immune cell function
598 but has not been explored in the context of IBD or CAC (Humphries et al., 2002; Mueller et al.,
599 2008; Pick et al., 2017; Stocker et al., 2018). However, increased expression of Coro1A has been
600 reported in several chronically inflamed and autoimmune disease models, such as renal fibrosis,
601 lupus nephritis, and lung fibrosis, as well as in some forms of cancer (X. Deng et al., 2024; Elihamu
602 et al., 2025; Kros et al., 2024; Nicolaou et al., 2020; Niu et al., 2024; Principi et al., 2023;

603 Siegmund et al., 2016). In lung adenocarcinoma, increased expression of Coro1A correlated with
604 TNM stage, ranked among the top 10 prognostic markers, particularly as an M2 or TAM
605 macrophage marker, and appeared to shape the tumor microenvironment (TME) (Z. Li et al., 2025;
606 Sun et al., 2024) (Bao et al., 2022; Y. Zhou et al., 2021). Coro1A expression is linked to cancer
607 pathogenesis, since knockdown of Coro1A curbs the growth and metastasis of breast cancer cells
608 (Elihamu et al., 2025; He et al., 2018; Jeon et al., 2024; Kros et al., 2024). Likewise, Coro 1A has
609 been identified as one of the five robust biomarkers in bladder cancer (Kumar et al., n.d.).

610 A direct interaction of Coro1A with the C-terminus of β_2 integrins is required
611 for polymorphonuclear leukocyte (PMNs) trafficking, adhesion, and post-adhesion events (Pick et
612 al., 2017). Furthermore, in a cystic fibrosis model, Coro1A was shown to regulate integrin
613 clustering and activation, a mechanism required for monocyte function (Younis et al., 2024). The
614 immune regulatory function of Coro 1A is exemplified by the finding linking Coro 1A to allograft
615 tolerance. Specifically, T cells lacking Coro1A suppressed the allograft rejection phenotype in a
616 wild-type host upon adoptive transfer, while maintaining T cell-specific responses against the
617 pathogen (Jayachandran et al., 2019). Likewise, Coro1A ^{KO} mice display attenuated response in
618 an experimental model of encephalomyelitis (Jayachandran et al., 2019; Kaminski et al., 2011).
619 Overall, these reports make it evident that several aspects of immune cell function, including
620 maintenance of numbers, trafficking, adhesion, and post-adhesion events, are directly governed by
621 Coro 1A(Jayachandran & Pieters, 2015; Mueller et al., 2008; Ndinyanka Fabrice et al., 2025; Pick
622 et al., 2017; Shiow et al., 2009; Younis et al., 2025).

623 Arguably, these phenotypes result from significant signaling alterations in these cells, with
624 Coro1A function playing a direct role. Coro1A was shown to regulate TGF-βR signaling in an
625 experimental autoimmune encephalomyelitis (EAE) model. Coro1A^{KO} mice exhibited less severe
626 EAE. Unexpectedly, upon re-induction of EAE, Coro1A^{KO} mice showed severe signs of EAE, with
627 a strong correlation with IL-17-producing T cells. Coro1A^{KO} Th17 cells show a severe defect in
628 TGF-βR-mediated SMAD3 activation, leading to increased IL-17 secretion (Kaminski et al.,
629 2011). TGF-β and IL-4 are key inducers of M2 macrophages and systemic immune suppression.
630 TGF-β promotes immune suppression in T cells, Dendritic cells (DCs), neutrophils, and
631 macrophages via canonical (SMAD2/3-dependent) and non-canonical pathways. TGF-β signaling
632 hampers DC maturation and antigen-presenting capacity by modulating co-stimulatory molecule

633 expression. In T-Cells, TGF-β suppresses TCR-induced cell proliferation and regulatory T cell
634 differentiation by inducing Foxp3. TGF-β also polarizes neutrophils towards the pro-tumorigenic
635 N2 phenotype. Given the broad immunosuppressive effects of TGF-β, we hypothesize that Coro1A
636 may regulate these TGF-β-induced processes in immune cells, as we have demonstrated in
637 macrophages (Z. Deng et al., 2024b; Fridlender et al., 2009; Gong et al., 2012a; C. S. Lin et al.,
638 2013; Mckarns et al., 2004; Strobl & Knapp, 1999).

639 Owing to TGF-β signaling's multifaceted functions, mutations in components have also
640 been linked to colorectal cancer, particularly in the tumor microenvironment (TME). Genetic
641 alterations in genes encoding components of the TGF-β signaling pathway, particularly TGF-βRII
642 (50-60%) and SMAD4 (46-48%), are the most common in CAC cases (Calon et al., 2012; Means
643 et al., 2018; Yashiro, 2014). In CAC macrophages, characterized as $CD11b^{+}$ $F4/80^{+}$ $Ly6C^{+}$, are
644 increased and play a crucial role in tumorigenesis; their depletion halts tumorigenesis. Highly
645 plastic macrophages under persistent chronic conditions polarize towards an M2-like phenotype
646 and act as a key driver of the CAC (Hardbower et al., 2017; Sheng et al., 2022; Shin et al., 2023;
647 Wang et al., 2023; Yuan et al., 2021).

648 Interestingly, polymorphisms in TGF-β Receptors and/or signaling components have been
649 reported to be associated with a concomitant decrease in the $CD11b^{+}$ $F4/80^{+}$ M2 macrophage
650 population (Gong et al., 2012). In line with this, in the current work, we observed that Coro1A is
651 a potent regulator of TGF-β signaling in macrophages in CAC. Myeloid cells play a key role in
652 shaping TME, and TGF-β signaling is essential for myeloid cell function in CAC (Chan et al.,
653 2022). Furthermore, TGF-β-deficient mice exhibit significantly reduced CAC burden, lower tumor
654 burden, and substantially reduced IL-6 and TNF-α production (J. Li et al., 2013; W. Wang et al.,
655 2015). This phenotype closely matches our observation in $Coro1A^{KO}$ mice, which show reduced
656 TGF-β signaling and fewer tumors. The integral role of Coro1A in immune cell function and TGF-
657 β signaling also strongly connects to fibrosis and the mechanisms that contribute to it. The c-AMP-
658 responsive element-binding protein (CREBH) controls Coro1A expression and regulates
659 autophagy in NASH, thereby preventing liver fibrosis. $CREBH^{KO}$ mice exhibit liver fibrosis by
660 activating TGF-β, CTGF signaling pathways, and deposition of collagen, α-SMA, and fibronectin
661 (Deng et al., 2024).An extensive clinical study involving colorectal cancer patients (N=94) showed
662 that overexpression of markers of cancer-associated fibroblasts was associated with tumor-

663 infiltrating lymphocytes, thus revealing a vital role for CAFs in maintaining the colorectal TME
664 (Zadka et al., 2021). In our study, Coro1A^{KO} mice showed resistance to polyp formation in an
665 AOM-DSS model, with significantly reduced markers of fibrosis, accompanied by attenuated
666 proliferation, oncogene, and EMT gene activation. The connection between Coro1A and fibrosis
667 and tumorigenesis was through its regulation of TGF-β signaling. Mechanistically, Coro1A-
668 mediated mobilized calcium activates Calcineurin phosphatases, which, in turn, activate genes
669 involved in preventing lysosomal fusion of phagosomes and signaling endosomes(Jayachandran
670 et al., 2007; Suo et al., 2014). In our study, we also found Coro1A employing the same calcium-
671 calcineurin pathway to protect the TGF-β signaling endosome from lysosomal degradation.

672 The fascinating part of the work is how SUMOylation of Raftlin protein bridges these
673 diverse pathways. We observed that Coro1A depends on SUMOylated Raftlin for stability via the
674 SUMO-SIM interaction. SIM-deficient Coro1A undergoes rapid degradation, leading to
675 concomitant dysregulated TGF-β signaling. Raftlin and Coro1A exhibit a functional correlation.
676 Like Coro1A, Raftlin also controls B-cell receptor (BCR) and T-cell receptor (TCR) signaling by
677 modulating calcium mobilization, and both are key players in clathrin-mediated endocytosis, a
678 common pathway utilized by TGF-β signaling endosomes to initiate signaling. Given their
679 functional correlation, our finding highlights SUMO as a connecting link between Coro1A and
680 Raftlin (Bayliss et al., 2020; Kazuko Saeki & Akihiko Yoshimura, 2003; Saeki et al., 2009;
681 Tatematsu et al., 2016; Watanabe et al., 2011) (Lacy et al., 2018). Presumably, SENP5 plays a role
682 in Raftlin SUMOylation, an attractive area for future research. Overall, our study revealed a critical
683 role of Coro1A in shaping the tumor microenvironment in CAC by modulating TGF-β signaling
684 and promoting a M2-like non-inflammatory macrophage phenotype.

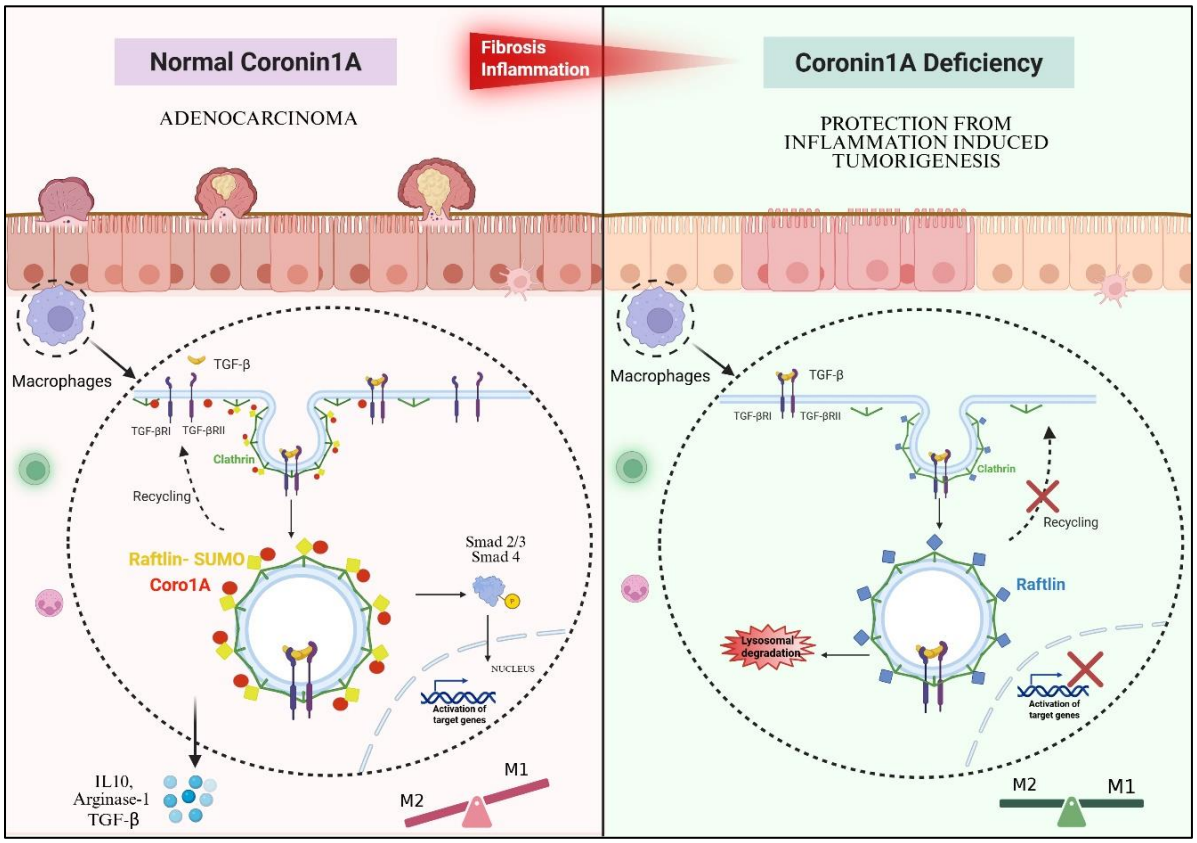
Normal Coronin1A
Fibrosis
Inflammation
Coronin1A Deficiency
ADENOCARCINOMA
PROTECTION FROM
INFLAMMATION INDUCED
TUMORIGENESIS
Macrophages
TGF-β
TGF-βRI
TGF-βRII
Clathrin
Recycling
Raftlin- SUMO
Coro1A
Smad 2/3
Smad 4
NUCLEUS
Activation of
target genes
IL10,
Arginase-1
TGF-β
M1
M2
Macrophages
TGF-β
TGF-βRI
TGF-βRII
Clathrin
Recycling
Raftlin
Lysosomal
degradation
Activation of
target genes
M2
M1

695 **Figure legends:**

696 **Dynamic expression pattern of SENP5 in chronic colitis and colitis-associated colorectal**
697 **cancer (CAC)**

698 A. Schematic representation of the chemically induced murine CAC model (AOM-DSS) in
699 C57BL/6 mice.

700 B. The graph represents the body weight of experimental animals during the development of
701 the AOM-DSS model.

702 C. A representative image showing the gross morphology of the colon. The graph on the right
703 shows the quantification of colon length. White arrows indicate polyps present at the distal end of
704 the colon.

705 D. A representative image shows the gross morphology of the spleen. The graph to the right
706 shows the spleen weight-to-body weight ratio in the mice.

707 E. Representative Hematoxylin and Eosin-stained colon section from Control, CC, non-polyp,
708 and polyp.

709 F. Immunoblot of SUMO-1 and SUMO-2/3 conjugated proteins (global SUMOylome) from
710 colonic tissue lysates of chronic colitis (CC) and polyps from the murine CAC model, with free
711 SUMO is shown in the red box.

712 G. Heatmap qRT-PCR-based fold change expression of deSUMOylases SENP1, SENP2,
713 SENP3, SENP5, SENP6, and SENP7 in CC, non-polyp, and polyp regions of the CAC murine
714 model relative to the average control values.

715 H. Immunoblot showing SENP5 expression in lysates from colonic tissue of Control, CC,
716 non-polyp, and polyp samples. The graph at the bottom shows the densitometric analysis of the
717 fold intensity of SENP5 expression, normalized to the loading control.

718 I. Immunoblot of SUMO-1 and SUMO-2/3 conjugated proteins (global SUMOylome) from
719 tissue lysates of CAC patient samples with free SUMO is shown in the red box.
720 J. qRT-PCR-based fold change expression of deSUMOylase SENP5 from SCRC (N=9) and
721 CAC (N=15) patient samples relative to the average IBS values (N=10).
722 K. Immunoblot showing SENP5 expression in colonic biopsies from control and CAC
723 patients. The graph at the bottom shows the densitometric analysis of the fold intensity of SENP5
724 expression, normalized to the loading control.
725 L. Immunoblot showing SENP5 expression in colonic tissue lysates of Control, non-polyp
726 SCRC, and polyp SCRC of $Apc^{+/+}$ and $APC^{+/-}$ model. The graph at the bottom shows the
727 densitometric analysis of the fold intensity of SENP5 expression, normalized to the loading
728 control.
729 Each dot represents (C, D, H, and L) for one mouse, (J) for one patient, and (K) lysate from one
730 patient biopsy. Each box represents one mouse (G). Actin was used as a loading control for F, H,
731 and L, and GAPDH was used as a loading control for I and K. GAPDH was used for gene
732 normalization (G and J). The immunoblots shown here are representative of three biological
733 replicates. Error bars represent mean ±SEM. Statistical analysis performed using the unpaired
734 Student's t-test, with a p-value <0.05 considered statistically significant. *<0.05, **<0.01,
735 ***<0.001, ****<0.0001, ns: non-significant.
736
737 Figure-2
738 **Altered interactome of SENP5 in chronic colitis and colitis-associated colorectal cancer**
739 A. Schematic representation of SENP5 pull-down using anti-SENP5 antibody from Control, CC,
740 non-polyp, and polyp tissue lysates. Isotype antibody (IgG) was used as a negative control.

741 B. Venn diagram showing the number of unique and common proteins across the Control, CC,
742 non-polyp, and polyp groups.
743 C. The Gene Ontology (GO) Pathway analysis (molecular function) of differentially enriched
744 SENP5 interacting proteins in the non-polyp and polyp region, as compared to the Control.
745 Pathway enrichment significance was assessed using hypergeometric and multiple test
746 correction at FDR less than 0.05.
747 D. Table of shortlisted potential SENP5 interacting proteins from the Actin binding function
748 pathway based on their functional role in cancer or any disease progression, and having a
749 SUMO binding or interacting motif.
750 E. Volcano plot of differentially enriched proteins with SENP5 in non-polyp and polyp as compared
751 to the Control, with shortlisted potential SENP5 interactors marked. Here, significance is defined
752 as fold change >2 and p-value < 0.05.
753
754 Figure-3
755 **Coro1A as an interactor of SENP5**
756 A. Top: Colonic tissue lysates of Control, CC, non-polyp, and polyp were immunoprecipitated with
757 anti-SENP5 antibody and immunoblotted for Coro1A. Bottom: 10% of input loaded from the
758 same tissue lysate and immunoblotted for Coro1A and Actin. Isotype antibody (IgG) was used
759 as a negative control.
760 B. Immunoblot showing Coro1A expression in colonic tissue lysates of Control, CC, non-polyp,
761 and polyp. The graph on the right shows densitometric analysis of fold intensity of Coro1A
762 expression, normalized to loading control.

763 C. Immunoblot showing Coro1A expression in colonic tissue lysates from Control, CC, and CAC
764 colon of an AOM-DSS model performed in IL-10$^{-/-}$ mice. The graph on the right shows
765 densitometric analysis of fold intensity of Coro1A expression, normalized to loading control.
766 D. Immunoblot showing Coro1A expression in human colonic biopsies of IBS (N=4) and ulcerative
767 colitis (N=5) patients. The graph on the right shows densitometric analysis of fold intensity of
768 Coro1A expression, normalized to loading control.
769 E. Immunohistochemistry of Coro1A in colonic tissue sections of Control, CC, non-polyp, and
770 polyp region of AOM-DSS mice model. Scale bar 100µm.
771 F. Immunohistochemistry of Coro1A in archived colonic biopsy slides from IBS, UC, and CAC
772 patients. Scale bar 100µm.
773 Each dot represents (B and C) one mouse or (D) one patient biopsy tissue lysate. Actin was used
774 as a loading control (A and B), and GAPDH was used as a loading Control (C and D). The inset
775 shows a zoomed image of a colon section. Asterisks show Coro1a expression (E and F). The
776 immunoblots shown here are representative of three biological replicates.
777 Error bars represent mean ±SEM. Statistical analysis performed using the unpaired Student's t-
778 test, with a p-value <0.05 considered statistically significant. *<0.05, **<0.01, ***< 0.001,
779 ****<0.0001, ns: non-significant.
780
781 Figure-4
782 **Absence of Coro1A confers resistance to CAC development in mice:**
783 A. Schematic representation of the chemically induced murine CAC model (AOM-DSS) in WT
784 (C57BL/6) and Coro1 A ^{KO} (C57BL/6) mice.

785 B. Representative longitudinal cut-open colon image from the CAC group of WT and Coro1A ^{KO}

786 mice. White arrows indicate polyps present at the distal end of the WT colon.

787 C. Representative Hematoxylin and Eosin-stained colon section from Control, CC, and CAC group

788 of WT and Coro1A ^{KO} mice.

789 D. Representative Sirius Red-stained colon section from Control, CC, and CAC group of WT and

790 Coro1A^{KO} mice.

791 E. qRT-PCR-based fold change expression of Proliferation and Oncogene; Ki67 and C-Myc

792 relative to the average control values.

793 F. qRT-PCR-based fold change expression of pro-inflammatory and anti-inflammatory markers,

794 COX-2 and Arginase-1, relative to the average control values.

795 G. qRT-PCR-based fold change expression of ECM markers, Fibronectin, α-SMA, and Col1A1

796 relative to the average control values.

797 H. qRT-PCR-based fold change expression of p53 relative to the average control values.

798 Each dot represents one of the mice (E, F, G, and H). Samples analyzed by qRT-PCR include

799 CC ^{WT}, CAC ^{WT}, CC $^{Coro1A\ KO}$, and CAC $^{Coro1A\ KO}$. GAPDH was used for Gene normalization

800 (E, F, G, and H). Error bars represent mean ± SEM. Statistical analysis performed using the

801 unpaired Student's t-test, with a p-value <0.05 considered statistically significant. *<0.05,

802 **<0.01, ***< 0.001, ****<0.0001, ns: non-significant.

803

804 Figure -5

805 **Increased expression of Coro 1A is associated with M2 macrophages.**

806 A. Representative counter plots showing F4/80^{+} and CD11b^{+} macrophage infiltration in Control,

807 CC, non-polyp, and polyp regions.

808 B. Percentage infiltration of macrophages in Control, CC, non-polyp, and polyp as determined by
809 flow cytometry.
810 C. Median Fluorescence intensity (MFI) of Coro1A in infiltrated macrophages across Control, CC,
811 non-polyp, and polyp as measured by flow cytometry.
812 D. Representative plot showing the distribution of iNOS$^+$ (%) and Arg-1$^+$ (%) macrophages across
813 Control, CC, non-polyp, and polyp.
814 E. Ratio of M2 (Arg-1$^+$) to M1 (iNOS$^+$) macrophages in all four conditions: Control, CC, non-
815 polyp, and polyp, as determined by flow cytometry.
816 F. MFI of Coro1A in Arg-1$^+$ macrophages across Control, CC, non-polyp, and polyp.
817 G. Immunoblot showing expression of Coro1A in bone-marrow-derived macrophages (BMDMs)
818 cells treated with IL-4 for 16, 18, and 20 hours. The graph on the right shows the densitometric
819 analysis of the fold intensity of Coro1A expression, normalized to the loading control.
820 H. Immunoblot showing expression of Coro1A in RAW 264.7 cells treated with TGF-β for 2,3, and
821 4 hours. The graph on the right shows the densitometric analysis of the fold intensity of Coro1A
822 expression, normalized to the loading control.
823 I. qRT-PCR analysis showing fold-change expression of M1(iNOS and IL-8) and M2 (Arg-1,
824 YM1, and Mrc1) macrophage markers in BMDMs treated with IL-4.
825 J. qRT-PCR analysis showing fold-change expression of M2 macrophage markers, Arginase-1, and
826 SNAIL in RAW264.7 cells treated with TGF-β.
827 K. Quantification of TGF-β levels in colonic tissue lysates from AOM-DSS mice, measured by
828 ELISA.

829 Each dot represents (B, C, E, F, and K) one mouse, or (G, H, I, and J) independent experiments
830 of 3 biological replicates. Actin is used as a loading control (G and H). GAPDH used for Gene

normalization (I and J). The immunoblots shown here are representative of three biological replicates. Error bars represent mean ± SEM. Statistical analysis performed using the unpaired Student's t-test, with a p-value <0.05 considered statistically significant. *<0.05, **<0.01, ***< 0.001, ****<0.0001, ns: non significant.

Figure-6

Coro1A interacts with TGF-β receptors directly and controls TGF-β-mediated M2 macrophage polarization.

A. Top: RAW264.7 cell lysates immunoprecipitated with anti-Coro1A antibody and immunoblotted for TGF-βRI. Bottom:10% of input loaded from the same cell lysate and immunoblotted for Coro1A, TGF-βRI, and Actin. Isotype antibodies (IgG) were used as a negative control.
B. Representative structured illumination microscopy (SIM) showing cellular localization of TGF-βRI (Red) and Coro 1A (Green). The asterisks in the zoomed version of the merged image show colocalization of TGF-βRI (Red) and Coro1A-GFP (Green).
C. Immunoblot confirming loss of Coro1A protein expression in stable J774 $^{\text{Coro1A KD}}$ cells compared to J774^{WT} cells.
D. Top: J774 ^{WT} and J774 $^{\text{Coro1A KD}}$ cell lysates immunoprecipitated with anti-Coro1A antibody and immunoblotted for TGF-βRI. Bottom: 10% of input loaded from cell lysate and immunoblotted for Coro1A, TGF-βRI, and Actin. Isotype antibodies (IgG) were used as a negative control.
E. qRT-PCR-based fold-change expression of Arginase-1 (left) and SNAIL (right) in J774 ^{WT} and J774 $^{\text{Coro1A KD}}$ cells with and without TGF-β stimulation.

854 F. Concentration analysis of IL-10 in the cell culture supernatant of J774 ^{WT} and J774$^{Coro1A\ KD}$
855 cells with and without TGF-β stimulation using ELISA.
856 G. Flow cytometry-based analysis of Arginase-1 positive cells in J774 ^{WT} and J774 $^{Coro1A\ KD}$ cells
857 with and without TGF-β stimulation.
858 H. qRT-PCR-based fold-change expression of TGF-βRI in J774 ^{WT} and J774 $^{Coro1A\ KD}$ cells with
859 and without TGF-β stimulation.
860 I. Immunoblot showing nuclear accumulation of SMAD3 post 30 and 60 minutes of TGF-β
861 exposure to J774 ^{WT} and J774 $^{Coro1A\ KD}$ cells.
862 J. Representative confocal images of BMDM ^{WT} and BMDM $^{Coro1A\ KO}$ cells with and without
863 TGF-β stimulation, stained for pSMAD3 (Red). A dotted white circle demarks nuclear
864 boundaries. The graph to the right illustrates the mean fluorescence intensity of pSMAD3 in
865 the nuclei (n = 60). (Scale bar = 5μm).
866 Each dot represents (E, F, G, and H) one independent experiment of a biological experiment,
867 and (J) one cell. Actin was used as a loading control (A, C, and D). Lamina AC was used as a
868 loading control (I), GAPDH was used for Gene normalization (E and H). The immunoblots shown
869 here are representative of three biological replicates. Error bars represent mean ± SEM. Statistical
870 analysis performed using the unpaired Student's t-test, with a *p*-value <0.05 considered
871 statistically significant. *<0.05, **<0.01, ***<0.001, ****<0.0001, ns: non-significant.
872
873
874
875
876

877 Figure-7

878 **Coro1A is required for the stability of TGF-βRI**

879 A. Immunoblot showing TGF-β R1 expression in J774 ^{WT} and J774 $^{Coro1A\ KD}$ cells. The graph at
880 the bottom shows densitometric analysis of the fold intensity of TGF-βRI, normalized to the
881 Control.

882 B. Representative confocal image of BMDM ^{WT} and BMDM $^{Coro1A\ KO}$ cells stained for TGF-
883 βRI (Green) (n=100). The graph on the right shows the quantification of TGF-βRI mean
884 fluorescence intensity. (Scale bar=5μm).

885 C. Immunoblot showing pAKT and AKT expression in J774 ^{WT} and J774 $^{Coro1A\ KD}$ cells. The graph
886 at the bottom shows the desitometric analysis of the fold intensity of pAKT, normalized to the
887 AKT.

888 D. Concentration analysis of TGF-β in the cell culture supernatant of J774 ^{WT} and J774 $^{Coro1A\ KD}$
889 cells using ELISA.

890 E. Concentration analysis of TGF-β from the tissue lysates of WT and Coro1A ^{KO} CAC (AOM-
891 DSS) mice model.

892 F. Immunoblot showing TGF-βRI expression in J774^{WT} and J774$^{Coro1A\ KD}$ cells with and without
893 Bafilomycin-A1 treatment (100nM). The graph at the bottom shows densitometric analysis of
894 TGF-βRI, normalized to the Control.

895 G. Representative confocal images of BMDM ^{WT} and BMDM $^{Coro1A\ ko}$ cells stained for TGF-βRI
896 (Green) using anti-TGF-βRI antibody and Lysosomes with LysoTracker Red DND-99 (Red).
897 The graph at the bottom illustrates the quantification of colocalization between TGF-βRI and
898 Lysosomes, as determined from images (n=60), using Mander's overlap coefficient. (Scale
899 bar=5μm).

900 Each dot represents an independent experiment (A, C, D, and F), one cell (B and G), and one
901 mouse (E). Actin was used as a loading control (A and F), and GAPDH was used as a loading
902 control (C). The immunoblots shown here are representative of three biological replicates.
903 Error bars represent mean ± SEM. Statistical analysis performed using the unpaired Student's
904 t-test, with a p-value <0.05 considered statistically significant. *<0.05, **<0.01, ***< 0.001,
905 ****<0.0001, ns: non-significant.

906 Figure-8

907 **Coro1A utilizes calcium-calcineurin signaling to protect TGF-βRI from lysosomal**
908 **degradation.**

909 A. Immunoblot showing TGF-βRI expression in RAW 264.7 cell lysate after treatment with
910 BAPTA-AM (10 μM). The graph on the right shows densitometric analysis of fold intensity of
911 TGF-βRI, normalized to the loading Control.

912 B. Immunoblot showing TGF-βRI expression in J774 ^{WT} and J774 $^{Coro1A\ KD}$ cell lysates post-
913 treatment with Inomycin (3.5 μM). The graph on the right shows densitometric analysis of fold
914 intensity of TGF-βRI, normalized to the loading Control.

915 C. Immunoblot showing TGF-βRI expression in RAW264.7 cell lysate post-treatment with
916 Cyclosporin A (CsA) (6 μM). The graph on the right shows densitometric analysis of fold
917 intensity of TGF-βRI, normalized to the loading Control.

918 D. Immunoblot showing TGF-βRI expression in RAW 264.7 cell lysate post-treatment with FK506
919 (3 μM). The graph on the right shows densitometric analysis of fold intensity of TGF-βRI,
920 normalized to the loading Control.

921 Each dot represents an independent biological replicate (A, B, C, and D). As a loading control,
922 Actin was used (A, B, C, and D). The immunoblots shown here are representative of three

923 biological replicates. Error bars represent mean ± SEM. Statistical analysis performed using the
924 unpaired Student's t-test, with a p-value <0.05 considered statistically significant. *<0.05,
925 **<0.01, ***< 0.001, ****<0.0001, ns: non-significant.

926 Figure-9

927 **SUMO2/3 governs the stability of Coro1A**

928 A. Top: J774^{WT} cell lysates immunoprecipitated with anti-Coro1A antibody and immunoblotted
929 for SUMO2/3. Bottom: reverse Co-IP using anti-SUMO2/3 antibody from the same lysates and
930 probed for Coro1A with 10% of input loaded and immunoblotted for Coro1A, SUMO2/3, and
931 Actin. Isotype antibodies (IgG) were used as a negative control.

932 B. The table represents possible SIM sites in Coro 1A as predicted by software programs GPS-
933 SUMO and JASSA. SIM sites predicted by both the software are highlighted in yellow.

934 C. Immunoblot showing Coro1A-GFP ^{WT} and SIM mutants (V124K, V155K, V167K) fusion
935 protein expression in transfected RAW264.7 cells. The graph at the bottom shows
936 densitometric analysis of the fold intensity of Coro1A-GFP, normalized to the loading control.

937 D. Immunoblot showing Coro1A -GFP ^{WT} and SIM mutants (V155K, V155A) fusion protein
938 expression in transfected RAW264.7 cells. The graph on the right shows densitometric
939 analysis of the fold intensity of Coro1A-GFP, normalized to the loading control.

940 E. Representative confocal images of Coro1A-GFP ^{WT} and SIM mutants (V124K, V155K,
941 V167K) fusion protein expression in transfected RAW264.7 cells. (Scale bar =5μm).

942 F. Immunoblot showing Coro1A and UBC9 expression upon siRNA-mediated UBC9
943 knockdown in RAW264.7 cells. The graphs at the bottom show densitometric analysis of the
944 fold intensity of Coro1A and UBC9, normalized to the loading control.

945 G. Immunoblot showing expression of Coro1A-GFP ^{WT} and SIM mutant (V155K) fusion protein
946 expression in RAW264.7 cells with and without treatment of MG-132 (20 μM) and
947 Bafilomycin-A1 (100 nM).
948 Each dot represents an independent experiment (C, D, and F) of biological replicates. Actin
949 was used as a loading control (A, C, D, F, and G). The immunoblots shown here are
950 representative of three biological replicates. Error bars represent mean ± SEM. Statistical
951 analysis performed using the unpaired Student's t-test, with a p-value <0.05 considered
952 statistically significant. *<0.05, **<0.01, ***< 0.001, ****<0.0001, ns: non-significant.

953 Figure-10

954 **Coro1A interacts with SUMOylated Raftlin-1 through the SIM site**

955 A. The table lists putative SUMOylated proteins identified by mass spectrometry.
956 B. Top: J774^{WT} and J774$^{Coro1A\ KD}$ cell lysates immunoprecipitated with anti-Coro1A antibody and
957 immunoblotted for Raftlin. 10% of the input was loaded from the same cell lysate and probed
958 for Raftlin, Coro1A, and Actin. Isotype antibody (IgG) was used as a negative control. Actin
959 was used as a loading control.
960 C. The table shows the possible SUMOylation sites in Raftlin, as predicted by GPS-SUMO and
961 JASSA. SUMoylation sites predicted by both software are highlighted in yellow.
962 D. Computational molecular docking of the alphafold structure of Raftlin and SUMO 2 using
963 HADDOCK2.4. web server. Alpha fold structure of Raftlin (Grey) and SUMO2 is (Magenta).
964 K31, the SUMO binding site is highlighted in Red.
965 E. Top: Raftlin^{WT}, Raftlin ^{K31R}, and Vector control transfected into RAW264.7 cell lysates were
966 immunoprecipitated with an anti-GFP antibody and immunoblotted for SUMO2/3, Coro1A,
967 and GFP. Bottom: 10% of the input was loaded from the same cell lysate and probed for Raftlin,

968 Coro1A, Actin, and SUMO2/3. Isotype antibody (IgG) was used as a negative control. Actin
969 was used as a loading control.
970 F. Representative images of structured illumination microscopy displaying images of transfected
971 RAW264.7 cells with Raftlin^{WT} and Raftlin ^{K31R} (Green) stained with Coro1A (Red) using anti-
972 Coro1A antibody. The inset shows zoomed areas of images, marked with arrows, to illustrate
973 colocalization (scale bar = 5 μm).
974 G. Computational molecular docking of the crystal structure of Coro1A (2AQ5) and stable binary
975 structure of Raftlin and SUMO 2 performed using HADDOCK2. 4. 3-D structure of Coro1A
976 (Green), Raftlin-1 (Grey), and SUMO2 is Magenta, and SIM sites 155-159 and SIM 167-171
977 are in red. The area of SUMO2 interacting with Coro1A is highlighted in yellow.
978 **Supplementary Figure 1**

979 A. qRT-PCR-based fold change expression of C-Myc from CC, non-polyp, and polyp tissue of
980 AOM-DSS mice model. GAPDH was used for gene normalization. Each dot represents one
981 mouse.
982 B. Schematic representation of the sporadic colorectal cancer (SCRC) model in Apc$^{+/+}$ and Apc
983 $^{+/-}$ mice.
984 C. Representative longitudinal cut-open colon image of Apc$^{+/+}$ and Apc$^{+/-}$ mice. Black arrows
985 indicate polyps present at the distal end of the colon.
986 Error bars represent mean ±SEM. Statistical analysis performed using the unpaired Student's t
987 test, with a p-value <0.05 considered statistically significant. *<0.05, **<0.01, ***< 0.001,
988 ****<0.0001, ns: non-significant.
989
990

991 **Supplementary Figure 2**

992 A. The Gene Ontology (GO) Pathway analysis (cellular component) of differentially enriched
993 SENP5 interacting proteins in the non-polyp and polyp region, as compared to the Control.
994 Pathway enrichment significance was assessed using hypergeometric and multiple test
995 correction at FDR less than 0.05.

996 B. Volcano plot of differentially enriched proteins with SENP5 in CC as compared to the Control,
997 with shortlisted potential SENP5 interactors marked. Here, significance is defined as fold
998 change >2 and *p*-value < 0.05.

999

1000 **Supplementary Figure 3**

1001 A. Schematic representation of the CAC (AOM-DSS) model in WT and $IL10^{-/-}$ mice.

1002 B. Schematic representation of the Acute colitis model (Day-7) in WT mice.

1003 C. Immunoblot showing Coro1A expression in lysates of colonic tissue from the acute colitis
1004 model. The graph on the right shows densitometric analysis of fold intensity of Coro1A
1005 expression, normalized to loading control.

1006 D. Immunoblot showing Coro1A expression in colonic tissue lysates of Control, non-polyp, and
1007 polyp ($Apc^{+/-}$)SCRC model. The graph on the right shows densitometric analysis of fold
1008 intensity of Coro1A expression, normalized to loading control.

1009 Each dot represents one mouse (C and D). Actin was used as a loading control (C and D). The
1010 immunoblots shown here are representative of three biological replicates. Error bars represent
1011 mean ±SEM. Statistical analysis performed using the unpaired Student's t-test, with a p-value
1012 <0.05 considered statistically significant. *<0.05, **<0.01, ***< 0.001, ****<0.0001, ns: non-
1013 significant.

1014 **Supplementary Figure 4**

1015 A. Representative immunoblot confirming loss of Coro1A protein expression in colonic tissue
1016 lysate of Coro1A ^{KO} mice compared to WT mice.

1017 B. Representative agarose gel image confirming the genotype of Coro1A ^{KO} mice (400bp).

1018 C. The graph represents the body weight of experimental animals during the development of the
1019 AOM-DSS model.

1020 D. A representative image showing the gross morphology of the colon from both genotypes (WT
1021 and Coro1A ^{KO}). The graph at the bottom shows the quantification of colon length.

1022 E. A representative image showing the gross morphology of the spleen (Splenomegaly) from both
1023 genotypes (WT and Coro1A ^{KO}). The graph at the bottom shows the quantification of spleen
1024 weight to the mice's body weight.

1025 F. Histopathological scoring of murine colon tissue sections was performed in a blinded manner
1026 by an experienced pathologist. Parameters such as collagen deposition, mascularis layer
1027 widening, crypt architecture distortion, and inflammation were scored as 0 (absent), 1(mild),
1028 and 2 (moderate). Field effect was scored as 0 (absent) and 1 (present), and dysplasia as 0
1029 (absent), 1 (low-grade dysplasia), and 2 (high-grade dysplasia).

1030 G. qRT-PCR-based fold change expression of E-Cadherin relative to the average control values.

1031 H. qRT-PCR-based fold change expression of EMT markers, SLUG, and SNAIL relative to the
1032 average control values.

1033 Each dot represents one mouse (D, E, F, and G). Samples analyzed by qRT-PCR include CC ^{WT},
1034 CAC ^{WT}, CC $^{Coro1A\ KO}$, and CAC $^{Coro1A\ KO}$. GAPDH was used for Gene normalization (F and G).
1035 Error bars represent mean ± SEM. Statistical analysis performed using the unpaired Student's t-

1036 test, with a p-value <0.05 considered statistically significant. *<0.05, **<0.01, ***< 0.001,
1037 ****<0.0001, ns: non-significant.
1038
1039 **Supplementary Figure 5**
1040 A. Representative flow cytometry plots showing the gating strategy used for cell population
1041 identification and analysis, including a fluorescence-minus-one (FMO) control.
1042 B. Representative counter plots showing CD 45^+ and $Ly6G^+$ neutrophil infiltration in Control, CC,
1043 non-polyp, and polyp regions.
1044 C. Percentage infiltration of Neutrophils in Control, CC, non-polyp, and polyp as determined by
1045 flow cytometry.
1046 D. Median Fluorescence intensity (MFI) of Coro1A in infiltrated neutrophils across Control, CC,
1047 non-polyp, and polyp as measured by flow cytometry.
1048 E. MFI of Coro1A in $iNOS^+$ macrophages across Control, CC, non-polyp, and polyp.
1049 Here, each dot represents one mouse (B, C, D, and E). Error bars represent mean ± SEM.
1050 Statistical analysis performed using the unpaired Student's t-test, with a p-value <0.05
1051 considered statistically significant. *<0.05, **<0.01, ***< 0.001, ****<0.0001, ns: non-
1052 significant.
1053 **Supplementary Figure 6**
1054 A. Top: RAW264.7 cell lysates immunoprecipitated with anti-Coro1A antibody and
1055 immunoblotted for TGF-βRII. Bottom:10% of input loaded from the same cell lysate and
1056 immunoblotted for Coro1A, TGF-β RII, and Actin. Isotype antibodies (IgG) were used as a
1057 negative control.

1058 B. Representative confocal images of J774 ^{WT} and J774 $^{Coro1A\ KD}$ cells showing a marked reduction
1059 in the expression of Coro1A in J774$^{Coro1A\ KD}$ cells (Scale bar=5μm). Coro1a shows typical cortex-
1060 based localization in J774^{WT} cells, which is absent in J774$^{Coro1A\ KD}$ cells. Actin was stained with
1061 Phalloidin to mark the cell boundaries.

1062 C. Immunoblot showing TGF-β secreted by J774 ^{WT} and J774 $^{Coro1A\ KD}$ cells in respective cell
1063 culture media. Ponceau image was used as a loading control. The graph at the bottom shows
1064 densitometric analysis of fold intensity of Coro1A expression, normalized to the loading control.

1065 D. Immunoblot showing TGF-β RI expression in J774 ^{WT} and J774 $^{Coro1A\ KD}$ cells with and without
1066 MG-132 treatment (20 μM). The graph on the right shows densitometric analysis of the fold
1067 intensity of TGF-βRI, normalized to the loading control.

1068 E. Representative immunoblot showing p62 expression in J774 ^{WT} and J774 $^{Coro1A\ KD}$ cells with
1069 and without Bafilomycin-A treatment (100 nM).

1070 F. Representative immunoblot showing poly-ubiquitination in J774 ^{WT} and J774 $^{Coro1A\ KD}$ cells with
1071 and without MG-132 treatment (20 μM).

1072 Each dot represents (C and D) one independent experiment of three biological replicates. Actin
1073 is used as a loading control (A, D, E, and F). The immunoblots shown here are representative of
1074 three biological replicates. Error bars represent mean ± SEM. Statistical analysis performed
1075 using the unpaired Student's t-test, with a p-value <0.05 considered statistically
1076 significant. *<0.05, **<0.01, ***< 0.001, ****<0.0001, ns: non-significant.

1077 **Supplementary Figure 7**

1078 A. Multiple sequence alignment of Coro1A protein sequences from eight mammalian species
1079 reveals that selected SIM sites are conserved (highlighted in a red rectangle).

1080 B. Table representing site-directed mutations performed in SUMO-interacting motifs (SIM) sites;
1081 Valine (V) of the SIM site replaced by Lysine (K).
1082 C. RMSF plots of Coro1A^{WT} and Coro1A^{V155K} mutant showing fluctuations of residues observed
1083 in molecular dynamics run by the CABS flex server.
1084 D. qRT-PCR-based fold change expression of UBC9 and Coro1A from RAW264.7 cells
1085 transfected with Scr siRNA and UBC9 siRNA. GAPDH was used for gene normalization. Each
1086 dot represents one independent experiment.
1087 E. Top: RAW 264.7 cell lysates immunoprecipitated with anti-Coro1A antibody and
1088 immunoblotted for Raftlin. Bottom:10% of input loaded from the same cell lysate and
1089 immunoblotted for Coro1A, Raftlin, and Actin. Isotype antibodies (IgG) were used as a negative
1090 control.
1091 F. Multiple sequence alignment of Raftlin protein sequences from eight mammalian species
1092 reveals a conserved SUMO-binding site (K31) (highlighted in a black rectangle).
1093 G. Representative immunoblot showing stable expression of Raftlin ^{K31R}, similar to Raftlin ^{WT}.
1094

1095 **Material Methods:**

1096 **Human patient samples:**

1097 Human patient samples for IBS (10), UC (19), SCRC (9), and CAC (15) were obtained from the
1098 Gastroenterology Department at All India Institute of Medical Sciences, New Delhi, India. Colonic
1099 biopsies of patients were obtained during routine colonoscopies, with exclusion and inclusion
1100 criteria as specified by Mustafa et al. (2017) and Suhail et al. (2019).Six biopsies were collected
1101 from each patient for use in qRT-PCR, immunoblotting, and histopathology. The study included
1102 patients with mild and moderate Ulcerative Colitis Endoscopic Index of Severity (UCEIS) scores.
1103 Informed consent forms were obtained from each patient during the biopsy procedure. The
1104 patient's sex was not considered in the current study. Ethical approval was obtained from the

1105 Regional Centre for Biotechnology (Approval No. RCB-IEC-H-11) and AIIMS (Approval No.
1106 IEC-217/05.04.2019, RP-19/2019) for using these patients' samples in the current study.

1107 **Mice:** All C57BL/6 mice were maintained in pathogen-free conditions by following all husbandry
1108 standards in the small animal facility of RCB. All mice were provided with sterilized food and
1109 water at 25 °C, under a 12-hour light/dark cycle. To induce CAC, Azoxymethane (AOM) was
1110 injected intraperitoneally into 6-8-week-old male/ female mice weighing 18-20 g at a dose of 10
1111 mg/kg. To induce chronic colonic inflammation, mice were fed 1% Dextran-sulfate-sodium (DSS)
1112 (w/v) (36–50 kDa molecular weight) through autoclaved drinking water for 7 days, followed by a
1113 recovery period of 1 week, during which mice were fed normal drinking water. The model lasts
1114 for 14 weeks. Mice in the control group were fed with normal drinking water. The same procedure
1115 was employed for developing CAC in IL10 $^{-/-}$ mice (C57BL/6 background, obtained from the
1116 National Institute of Immunology, India) and Coro1A$^{-/-}$ mice (C57BL/6 background, kindly
1117 provided by Prof. Jean Pieters, Biozentrum, Switzerland). An acute colitis model was performed
1118 in 6-8-week-old male/female mice weighing 18-20 g, as described by (Suhail et al., 2019).
1119 Symptoms of colitis, such as diarrhea, rectal bleeding, and body weight loss, were monitored
1120 routinely throughout the experiment. Sporadic colorectal cancer model performed in APC$^{+/-}$ mice.
1121 For 1 week, WT and APC$^{+/-}$ mice were fed 2% DSS, followed by 14 weeks of normal drinking
1122 water. Organs, such as the colon and spleen, were examined for gross morphological changes and
1123 used for further experimental analysis. For some crucial *in vitro* experiments, Bone marrow-
1124 derived macrophages (BMDMs) from WT and Coronin1a $^{-/-}$ mice were harvested. The RCB
1125 Institutional Animal Ethics Committee (IAEC) has approved the above-mentioned animal studies
1126 (RCB/IAEC/2024/199, RCB/IAEC/2023/177, RCB/IAEC/2023/156, RCB/IAEC/2021/101).

1127 **Cell culture and transfections**: Murine macrophage cell lines RAW 264.7 and J774 ^{WT} and J774
1128 $^{Coro1A\ KD}$ cell lines were grown in DMEM containing 10% fetal bovine serum, 3.7 g/litre Sodium
1129 bicarbonate, 1% sodium pyruvate, 1% penicillin and streptomycin solution, and 14 mM HEPES
1130 buffer (pH 7.4). BMDMs isolated and cultured from WT and Coronin1A $^{-/-}$ mice as described
1131 by(Toda et al., 2021). All cells were incubated at 37 °C with 5% CO_2. RAW264.7 cells were used
1132 for plasmid-based overexpression and siRNA-based knockdown studies. WT plasmids and
1133 mutants of Coro1A and Raftlin, and Scrambled and targeted UBC9 siRNA were transfected in
1134 RAW264.7 using Xtremegene (Merck) and DharmaFECT (Horizon Discovery) according to the

1135 manufacturer's instructions. RAW264.7, BMDMs, J774 ^{WT,} and J774 $^{Coro1A\ KD}$ cells were
1136 stimulated with IL-4 (20ng/ml) and TGF-β (10ng/ml) for a specified time period. The
1137 pharmacological drugs used in this study to treat RAW264.7, J774 ^{WT,} and J774 $^{Coro1A\ KD}$ cells are
1138 MG-132, Bafilomycin-A1, BAPTA-AM, FK-506, Cyclosporin-A, and Ionomycin. Unstimulated
1139 or untreated cells served as the control.

1140 **Immunoblot**: Human and murine tissues and cell lysates were prepared using RIPA lysis buffer
1141 containing 1X protease inhibitor and 20 mM NEM. The BCA assay was used to quantify proteins.
1142 Equal concentrations of proteins were separated on sodium-dodecyl sulphate polyacrylamide gel
1143 electrophoresis (SDS-PAGE) and transferred to a 0.2 µm or 0.4 µm nitrocellulose membrane. Blots
1144 were blocked with 5% skim milk for 1 hour at room temperature, then probed with antibodies
1145 against the desired proteins overnight at 4 °C. Protein blots were probed with the following set of
1146 antibodies: SENP5, SUMO2/3, SMAD3, Coronin1A, GFP, Actin, GAPDH, TGF-beta, TGF-βRI,
1147 pAKT, AKT, Raftlin, Ubiquitin, and P62. The next day, host-specific HRP-conjugated secondary
1148 antibodies, anti-Rabbit and anti-Mouse, were added and incubated for 1 hour at room temperature.
1149 Protein bands were then detected with Immobilon Forte Western HRP substrate and visualized
1150 with the ImageQuant LAS-4000 imaging system. Immunoblot densitometry analysis was
1151 performed using ImageJ software.

1152 **Quantitative real-time PCR:** RNA was extracted from human patient biopsies, mouse tissue, and
1153 different cell lines using the RNeasy RNA isolation kit. cDNA was synthesized using 1 µg of
1154 isolated RNA from each sample using the iScript cDNA Synthesis Kit. Real-time PCR was
1155 performed using SYBR Green Master Mix in a 20 µL reaction volume on 96-well plates with the
1156 CFX96 Real-Time System. The housekeeping genes GAPDH and HPRT were used for
1157 normalization based on each sample's origin. The list of primers used in this study is included in
1158 the supplementary material.

1159 **Immunohistochemistry**: Mice colon tissue sections were fixed in 4% paraformaldehyde solution
1160 overnight and transferred to cryomatrix, followed by snap-freezing in liquid nitrogen. 5 µm-thick
1161 sections were cut onto glass slides using a Cryotome. The patient's archived tissue biopsy slides
1162 were obtained from the Department of Pathology at AIIMS, New Delhi, India. Tissue sections
1163 were washed three times in 1x PBS (5 minutes each). Further, slides were treated with 3%
1164 Hydrogen peroxide for 10 minutes to quench endogenous peroxidase activity, followed by a

1165 second wash with PBS. Further slides were blocked with 5% Goat serum for 1 hour. Then, the
1166 sections were incubated overnight in a humid chamber with Coronin1A. The next day, sections
1167 were washed with PBS, then incubated with HRP-conjugated secondary antibodies for 2 hours.
1168 Further slides were washed in PBS, stained with DAB, and counterstained with Hematoxylin.
1169 Tissue sections were imaged using a Nikon Bright Field microscope.

1170 **Co-Immunoprecipitation**: Tissue lysate and cell lysate prepared using IP lysis buffer having 1X
1171 protease inhibitor. Samples were centrifuged at high speed at 4ºC for 10 minutes to remove debris.
1172 The supernatant was quantified to 1 mg protein, followed by the addition of the appropriate
1173 antibody at its concentration. Antibody-protein complexes were incubated overnight on an end-to-
1174 end rotor. The next day, activated Agarose-A-beads were used to pull down the antibody-protein
1175 complex. Beads were sedimented by centrifugation (0.5 rcf, 4ºC), washed with IP lysis buffer, and
1176 then denatured. An isotype control IgG was used as a negative control.

1177 **Nuclear fraction isolation:** Cells were washed with chilled PBS, scraped, and collected in pre-
1178 chilled tubes on ice. After centrifugation (10,000 rpm, 5 minutes, and 4 °C), the pellet was
1179 resuspended in a lysis buffer containing chilled PBS, protease inhibitors (PI), and NP-40, and
1180 incubated on ice for 10 minutes. To separate the cytoplasmic fraction, the cell lysate was
1181 centrifuged (10 minutes, 10,000 rpm, 4 °C). The supernatant is the cytoplasmic fraction, and the
1182 pellet is the nuclear fraction. The obtained nuclear pellet was washed 3 times with lysis buffer and
1183 subsequently denatured.

1184 **Hematoxylin and Eosin (H&E) and Sirius red staining:** 5-µm-thick paraffin-embedded tissue
1185 sections were deparaffinized in Xylene and rehydrated through a graded ethanol to distilled water.
1186 For H & E staining, tissue sections were stained with Hematoxylin, followed by eosin
1187 counterstaining. For Sirius red staining, tissue sections were stained with Weigert's iron
1188 hematoxylin, followed by Sirius red stain, and subsequently washed with acidified water to
1189 visualize collagen. Sliders were dehydrated in graded alcohol, cleared in Xylene, and mounted
1190 using DPX mountant. Tissue sections were visualized under a bright-field microscope.

1191 **Immunocytochemistry and structured illumination microscopy:** Cells seeded on a glass
1192 coverslip, fixed with 4% methanol-free paraformaldehyde, washed with PBS, and blocked in 0.1
1193 % BSA containing 0.01% Triton X-100 for 1 hour. Further cells were incubated overnight at 4ºC

1194 with primary antibodies against Coro1A, TGF-βRI, GFP, pSMAD3, Lysotracker, and Phalloidin-
1195 594, followed by a fluorochrome-conjugated secondary antibody the next day for 2 hours at room
1196 temperature. DAPI was used to counterstain nuclei. Coverslips were mounted using Prolong Gold
1197 antifade reagent and imaged by confocal microscopy (Leica SP8) or structured illumination
1198 microscopy (Elyra PS1, Carl Zeiss).

1199 **Lamina propria isolation:** The Lamina propria of the colon was isolated using the method
1200 described by Weigmann et al. (2007). Briefly, the harvested mouse colon was washed with ice-
1201 cold PBS, then longitudinally cut open and again washed with PBS to remove mucus. The open
1202 intestine is cut into small pieces and subjected to predigestion in a buffer containing 5 mM EDTA
1203 and 1 mM DTT for 15-20 minutes in a shaking incubator. With vigorous vortexing, the predigested
1204 tissue was filtered through a 100 µm filter. The remaining tissue was finely chopped and incubated
1205 in a buffer containing collagen and DNase I (50mg per 100 ml PBS) for one hour at 37ºC on slow
1206 shaking. After incubation, the tubes were vortexed, and the cell suspension was passed through a
1207 40 µm strainer. The collected single-cell suspension was vortexed and centrifuged at 500 g for 10
1208 minutes at room temperature. The pellet obtained was resuspended in PBS, and proceeded to flow
1209 cytometric immune phenotyping.

1210 **Flow Cytometry:** Flow cytometric analysis was carried out for immune cells retrieved from the
1211 lamina propria region of the colon (*in vivo*) and cultured J774 ^{WT} and J774 $^{Coro1A\ KD}$ cells (*in vitro*).
1212 *In vivo*-derived immune cells were stained with fixable live-dead stain (Aqua Zombie) for 15
1213 minutes at room temperature in the dark, followed by surface marker staining with fluorophore-
1214 conjugated antibodies against CD-45, CD11b, F4/80, and Ly6G for 1 hour at 4ºC. Further, cells
1215 were fixed with 4% paraformaldehyde at room temperature, followed by permeabilization with
1216 chilled methanol for 20 minutes on ice. Intracellular staining was performed using anti-iNOS and
1217 anti-Arginase-1 fluorophore-conjugated antibodies, along with a primary antibody against
1218 Coronin1A for 1 hour of incubation, followed by secondary antibody staining for 1 hour. The same
1219 fixation, permeabilization, and intracellular staining procedure was employed for *in vitro*-cultured
1220 J774 ^{WT} and J774 $^{Coro1A\ KD}$ cells to stain Arginase-1. Stained cells were resuspended in FACS
1221 buffer, acquired on a BD FACSymphony, and analyzed using FlowJo software.

1222 **Enzyme-linked immunosorbent assay**: Cell supernatant collected from the cell culture system
1223 and colonic tissue lysates were centrifuged to remove debris. The samples were quantified using

1224 the BCA assay, and equal concentrations of samples were subjected to a kit-based enzyme-linked
1225 immunosorbent assay (ELISA) (R&D Systems) to measure TGF-β & IL-10.

1226 **Protein Digestion and LC-MS/MS**: Murine tissue lysates were immunoprecipitated using an
1227 anti-SENP5 antibody, and J774 cell lysates were immunoprecipitated with an anti-Coronin1A
1228 antibody. An isotype-matched IgG antibody was used as a negative control. The co-
1229 immunoprecipitated samples were resolved on 10% SDS–PAGE, followed by in-gel digestion
1230 with Trypsin Gold at a 1:50 enzyme-to-substrate ratio. The resulting peptides were extracted and
1231 purified using C18 StepPak columns, desalted, and reconstituted in a solution of 98% water, 1%
1232 acetonitrile, and 0.1% formic acid.

1233 Tandem MS/MS analysis was performed on a TripleTOF 5600 mass spectrometer (AB Sciex)
1234 operated in information-dependent acquisition (IDA) mode. The instrument was coupled to a trap
1235 column (Magic C18 AQ, 0.1 × 20 mm, 3 µm, 200 Å) and an analytical column (Magic C18 AQ,
1236 0.1 × 150 mm, 3 µm, 200 Å) via a nano-electrospray ionization source. Peptide separation was
1237 achieved using a linear gradient of 5–75% solvent B (100% acetonitrile with 0.1% formic acid)
1238 over 135 minutes at a flow rate of 300 nL/min; solvent A was 100% water with 0.1% formic acid.

1239 The mass spectrometer was operated in data-dependent acquisition mode, automatically switching
1240 between MS and MS/MS scans. Survey MS spectra were acquired over an m/z range of 300–2000
1241 at a resolution of 75,000. The six most abundant precursor ions per cycle were selected for
1242 fragmentation by collision-induced dissociation (CID), with a fixed cycle time of 3 s and a dynamic
1243 exclusion period of 2 min. The obtained raw files from the MS system (.wiff) were processed for
1244 peptide/protein identification using MaxQuant software (v1.6.0.16) under default settings. An in-
1245 house combined UniProt (*Mus musculus*) database, together with common contaminants
1246 sequences, was provided for MS/MS spectra search. The detailed workflow of peptide/protein
1247 identification, including other search parameters and filtering criteria, was followed as mentioned
1248 in (Suhail et al., 2019)

1249 **Structural modeling and docking**: The crystal structure of Coro1A (PDB ID: 2AQ5) and the
1250 AlphaFold-predicted structures of Raftlin1 and SUMO2 were used for protein–protein docking.
1251 Blind docking was performed using the HADDOCK 2.4 web server
1252 (https://rascar.science.uu.nl/haddock2.4/) in standard-precision mode, generating multiple poses

without predefined binding sites. The docked models were clustered and ranked using the default HADDOCK scoring function, and the top three complexes were selected for refinement. Further, using the Schrödinger software suite (https://www.schrodinger.com/), the energies of poses were minimized, and binding energies were calculated. The final model was selected based on the high docking score and favorable minimized binding energies.

Multiple sequence alignment (MSA): FASTA sequences of Coro1A and Raftlin from 8 organisms were retrieved from the Uniprot database and aligned using Clustal Omega with default parameters. Multiple sequence alignments were visualized and analyzed using Jalview (v2.11.5.0) with the ClustalX coloring scheme. Alignment annotations, including consensus, conservation, quality scores, and occupancy, were displayed below the alignment.

Molecular Dynamics Simulation: The wild-type Coro1A structure (PDB ID: 2AQ5) and the PyMOL-generated Coro1A V155K mutant were subjected to molecular dynamics simulations using the CABS flex server with default parameters for 10 seconds, an equivalent simulation time. The server uses coarse-grained Monte Carlo simulations to efficiently sample near-native protein conformational dynamics. Default parameters were used, including structural clustering and all-atom reconstruction. The resulting ensembles were analyzed for conformational flexibility and residue fluctuations, with residue-wise mobility quantified using root-mean-square fluctuation (RMSF) plots generated with the server's analysis tools.

Quantification and statistical analysis: Data were analyzed and visualized using GraphPad Prism version 8.0.1. Results are presented as the mean ± standard error from independent experiments performed in triplicate. As appropriate, statistical analysis was carried out using the unpaired two-tailed Student's t-test or Welch's t-test. A *p*-value less than 0.05 was considered statistically significant.

Acknowledgment:

We thank the sophisticated instrumentation facility at the Central Instrumentation Facility (CIF) of the Regional Centre for Biotechnology (RCB), the Flow Cytometry, Confocal Microscopy, Genomics, and Mass Spectrometry facility of the Advanced Technology Platform Centre (ATPC) in the RCB campus, and the Experimental Animal Facility (EAF) at NCR-Biotech Science Cluster

for animal experiments. We acknowledge Addgene for the Coro1A plasmid (102815). We are grateful to Prof. Josef M. Penninger for sharing Coro1A knockout mice. We are thankful to Prof. Venuprasad Poojary for the Raftlin Plasmid. We thank Prof. Tushar K. Maiti for his extended help with mass spectrometry-based experiments. We are grateful to Dr. Rajender Motiani and Dr. Pallavi Keshtrapal for sharing the crucial reagents used in the experiments.

Funding: This work was supported by an RCB Core Grant, an ICMR(IIRP/SG-2024-01-00385) and DBT (BT/PR45284/CMD/150/9/2022) grant, and a CSIR-JRF fellowship (Council of Scientific and Industrial Research, Govt. of India) of Rohan Babar.

Competing Interest:
The authors declare that they have no competing interests**.**

Author Contributions:

Conceptualization: Chittur V. Srikanth.

Methodology: Rohan Babar, Chittur V. Srikanth.

Investigation: Rohan Babar, Poorvi Saini, Neha Guliya, Prakhar Varshney, Vishnu Ashok Kumar, Prabhakar Mujagond.

Resource: Rohan Babar, Aamir Suhail, Mukesh Singh, Dolly Jain, Lalita Mehra, Shivangi Tyagi.

Supervision: Avinash Bajaj, Krishnan Vengadesan, Prasenjit Das, Vineet Ahuja, and Chittur V. Srikanth.

Project Administration: Chittur V. Srikanth.
Writing-original draft: Rohan Babar, Poorvi Saini, Neha Guliya, and Prakhar Varshney.

Writing -review and editing- Rohan Babar and Chittur V. Srikanth.

1314 References:

1315 1. Foersch S, Neurath MF. Colitis-associated neoplasia: Molecular basis and clinical
1316 translation. Vol. 71, Cellular and Molecular Life Sciences Birkhauser Verlag AG; 2014. p.
1317 3523–35.

1318 2. Zhou RW, Harpaz N, Itzkowitz SH, Parsons RE. Molecular mechanisms in colitis-
1319 associated colorectal cancer. Vol. 12, Oncogenesis Springer Nature; 2023.

1320 3. Díaz-Gay M, dos Santos W, Moody S, Kazachkova M, Abbasi A, Steele CD, et al.
1321 Geographic and age variations in mutational processes in colorectal cancer. Nature.
1322 Nature Research; 2025;643(8070):230–40. DOI: 10.1038/s41586-025-09025-8

1323 4. Bogaert J, Prenen H. Molecular genetics of colorectal cancer. Vol. 27, Annals of
1324 Gastroenterology 2014. p. 9–14.

1325 5. Su Z, El Hage M, Linnebacher M. Mutation patterns in colorectal cancer and their
1326 relationship with prognosis. Heliyon. Elsevier Ltd; 2024;10(17). DOI:
1327 10.1016/j.heliyon.2024.e36550

1328 6. Yin Y, Wan J, Yu J, Wu K. Molecular Pathogenesis of Colitis-associated Colorectal
1329 Cancer: Immunity, Genetics, and Intestinal Microecology. Vol. 29, Inflammatory Bowel
1330 Diseases Oxford University Press; 2023. p. 1648–57.

1331 7. Yamagishi H, Kuroda H, Imai Y, Hiraishi H. Molecular pathogenesis of sporadic
1332 colorectal cancers. Vol. 35, Chinese Journal of Cancer Landes Bioscience; 2016.

1333 8. Yashiro M. Ulcerative colitis-associated colorectal cancer. World J Gastroenterol. WJG
1334 Press; 2014;20(44):16389–97. DOI: 10.3748/wjg.v20.i44.16389

1335 9. Shawki S, Ashburn J, Signs SA, Huang E. Colon Cancer: Inflammation-Associated
1336 Cancer. Vol. 27, Surgical Oncology Clinics of North America W.B. Saunders; 2018. p.
1337 269–87.

1338 10. Kakiuchi N, Yoshida K, Uchino M, Kihara T, Akaki K, Inoue Y, et al. Frequent mutations
1339 that converge on the NFKBIZ pathway in ulcerative colitis. Nature. Nature Research;
1340 2020;577(7789):260–5. DOI: 10.1038/s41586-019-1856-1

1341 11. Dan WY, Zhou GZ, Peng LH, Pan F. Update and latest advances in mechanisms and
1342 management of colitis-associated colorectal cancer. Vol. 15, World Journal of
1343 Gastrointestinal Oncology Baishideng Publishing Group Inc; 2023. p. 1317–31.

1344 12. Deng Y, Jia X, Liu L, He Q, Liu L. The role of intestinal macrophage polarization in
1345 colitis-associated colon cancer. Vol. 16, Frontiers in Immunology Frontiers Media SA;
1346 2025.

1347 13. Zhang M, Li X, Zhang Q, Yang J, Liu G. Roles of macrophages on ulcerative colitis and
1348 colitis-associated colorectal cancer. Vol. 14, Frontiers in Immunology Frontiers Media
1349 S.A.; 2023.

1350 14. Shin AE, Tesfagiorgis Y, Larsen F, Derouet M, Zeng PYF, Good HJ, et al.
1351 F4/80+Ly6Chigh Macrophages Lead to Cell Plasticity and Cancer Initiation in Colitis.
1352 Gastroenterology. W.B. Saunders; 2023;164(4):593-609.e13. DOI:
1353 10.1053/j.gastro.2023.01.002

1354 15. Hardbower DM, Coburn LA, Asim M, Singh K, Sierra JC, Barry DP, et al. EGFR-
1355 mediated macrophage activation promotes colitis-associated tumorigenesis. Oncogene.
1356 Nature Publishing Group; 2017;36(27):3807–19. DOI: 10.1038/onc.2017.23

1357 16. Wang Y, Liu H, Zhang Z, Bian D, Shao K, Wang S, et al. G-MDSC-derived exosomes
1358 mediate the differentiation of M-MDSC into M2 macrophages promoting colitis-to-cancer
1359 transition. J Immunother Cancer. BMJ Publishing Group; 2023;11(6). DOI: 10.1136/jitc-
1360 2022-006166

1361 17. Yuan Q, Gu J, Zhang J, Liu S, Wang Q, Tian T, et al. MyD88 in myofibroblasts enhances
1362 colitis-associated tumorigenesis via promoting macrophage M2 polarization. Cell Rep.
1363 Elsevier B.V.; 2021;34(5). DOI: 10.1016/j.celrep.2021.108724

1364 18. Sheng YH, Davies JM, Wang R, Wong KY, Giri R, Yang Y, et al. MUC1-mediated
1365 Macrophage Activation Promotes Colitis-associated Colorectal Cancer via Activating the
1366 Interleukin-6/ Signal Transducer and Activator of Transcription 3 Axis. CMGH. Elsevier
1367 Inc.; 2022;14(4):789–811. DOI: 10.1016/j.jcmgh.2022.06.010

1368 19. Long Y, Huang F, Zhang J, Zhang J, Cheng R, Zhu L, et al. Identification of
1369 SUMOylation-related signature genes associated with immune infiltration in ulcerative
1370 colitis through bioinformatics analysis and experimental validation. Gene. Elsevier B.V.;
1371 2025;935. DOI: 10.1016/j.gene.2024.148996

1372 20. Ma XN, Li MY, Qi GQ, Wei LN, Zhang DK. SUMOylation at the crossroads of gut
1373 health: insights into physiology and pathology. Vol. 22, Cell Communication and
1374 Signaling BioMed Central Ltd; 2024.

1375 21. Gostissa M, Hengstermann A, Fogal V, Sandy P, Schwarz SE, Scheffner M, et al.
1376 Activation of p53 by conjugation to the ubiquitin-like protein SUMO-1. Vol. 18, The
1377 EMBO Journal 1999.

1378 22. Zhou Z, Wang M, Li J, Xiao M, Chin YE, Cheng J, et al. SUMOylation and SENP3
1379 regulate STAT3 activation in head and neck cancer. Oncogene. Nature Publishing Group;
1380 2016;35(45):5826–38. DOI: 10.1038/onc.2016.124

1381 23. Yang Q, Tang J, Xu C, Zhao H, Zhou Y, Wang Y, et al. Histone deacetylase 4 inhibits
1382 NF-κB activation by facilitating IκBα sumoylation. J Mol Cell Biol. Oxford University
1383 Press; 2020;12(12):933–45. DOI: 10.1093/jmcb/mjaa043

1384 24. Lin CH, Liu SY, Lee EHY. SUMO modification of Akt regulates global SUMOylation
1385 and substrate SUMOylation specificity through Akt phosphorylation of Ubc9 and
1386 SUMO1. Oncogene. Nature Publishing Group; 2016;35(5):595–607. DOI:
1387 10.1038/onc.2015.115

1388 25. Liu T, Wang H, Chen Y, Wan Z, Du Z, Shen H, et al. SENP5 promotes homologous
1389 recombination-mediated DNA damage repair in colorectal cancer cells through H2AZ
1390 deSUMOylation. Journal of Experimental and Clinical Cancer Research. BioMed Central
1391 Ltd; 2023;42(1). DOI: 10.1186/s13046-023-02789-9

1392 26. Sheng Z, Luo S, Huang L, Deng YN, Zhang N, Luo Y, et al. SENP1-mediated
1393 deSUMOylation of YBX1 promotes colorectal cancer development through the SENP1-
1394 YBX1-AKT signaling axis. Oncogene. Springer Nature; 2025;44(19):1361–74. DOI:
1395 10.1038/s41388-025-03302-6

1396 27. Du L, Li YJ, Fakih M, Wiatrek RL, Duldulao M, Chen Z, et al. Role of SUMO activating
1397 enzyme in cancer stem cell maintenance and self-renewal. Nat Commun. Nature
1398 Publishing Group; 2016;7. DOI: 10.1038/ncomms12326

1399 28. Arnesen H, Müller MHB, Aleksandersen M, Østby GC, Carlsen H, Paulsen JE, et al.
1400 Induction of colorectal carcinogenesis in the C57BL/6J and A/J mouse strains with a
1401 reduced DSS dose in the AOM/DSS model. Lab Anim Res. BioMed Central Ltd;
1402 2021;37(1). DOI: 10.1186/s42826-021-00096-y

1403 29. Ren J, Sui H, Fang F, Li Q, Li B. The application of ApcMin/+ mouse model in colorectal
1404 tumor researches. Vol. 145, Journal of Cancer Research and Clinical Oncology Springer
1405 Science and Business Media Deutschland GmbH; 2019. p. 1111–22.

1406 30. Sánchez-Alba L, Ying L, Maletic MD, De Bolòs A, Borràs-Gas H, Liu B, et al. Structural
1407 basis for the human SENP5's SUMO isoform discrimination. Nature Communications .
1408 Nature Research; 2025;16(1). DOI: 10.1038/s41467-025-60029-4

1409 31. Galkin VE, Orlova A, Brieher W, Yuan Kueh H, Mitchison TJ, Egelman EH. Author
1410 manuscript. Vol. 376, J Mol Biol 2008.

1411 32. Humphries CL, Balcer HI, D'Agostino JL, Winsor B, Drubin DG, Barnes G, et al. Direct
1412 regulation of Arp2/3 complex activity and function by the actin binding protein coronin.
1413 Journal of Cell Biology. 2002;159(6):993–1004. DOI: 10.1083/jcb.200206113

1414 33. Mueller P, Massner J, Jayachandran R, Combaluzier B, Albrecht I, Gatfield J, et al.
1415 Regulation of T cell survival through coronin-1-mediated generation of inositol-1,4,5-

1416 trisphosphate and calcium mobilization after T cell receptor triggering. Nat Immunol.
1417 2008;9(4):424–31. DOI: 10.1038/ni1570

1418 34. Stocker TJ, Pircher J, Skenderi A, Ehrlich A, Eberle C, Megens RTA, et al. The Actin
1419 Regulator Coronin-1A Modulates Platelet Shape Change and Consolidates Arterial
1420 Thrombosis. Thromb Haemost. Georg Thieme Verlag; 2018;118(12):2098–111. DOI:
1421 10.1055/s-0038-1675604

1422 35. Castro-Castro A, Ojeda V, Barreira M, Sauzeau V, Navarro-Lérida I, Muriel O, et al.
1423 Coronin 1A promotes a cytoskeletal-based feedback loop that facilitates Rac1
1424 translocation and activation. EMBO Journal. 2011;30(19):3913–27. DOI:
1425 10.1038/emboj.2011.310

1426 36. Pick R, Begandt D, Stocker TJ, Salvermoser M, Thome S, Böttcher RT, et al. Coronin 1A,
1427 a novel player in integrin biology, controls neutrophil trafficking in innate immunity.
1428 Blood. American Society of Hematology; 2017;130(7):847–58. DOI: 10.1182/blood-
1429 2016-11-749622

1430 37. Nicolaou O, Sokratous K, Makowska Z, Morell M, De Groof A, Montigny P, et al.
1431 Proteomic analysis in lupus mice identifies Coronin-1A as a potential biomarker for lupus
1432 nephritis. Arthritis Res Ther. BioMed Central; 2020;22(1). DOI: 10.1186/s13075-020-
1433 02236-6

1434 38. Siegmund K, Klepsch V, Hermann-Kleiter N, Baier G. Proof of principle for a T
1435 lymphocyte intrinsic function of Coronin 1A. Journal of Biological Chemistry. American
1436 Society for Biochemistry and Molecular Biology Inc.; 2016;291(42):22086–92. DOI:
1437 10.1074/jbc.M116.748012

1438 39. Principi L, Ferrini E, Ciccimarra R, Pagani L, Chinello C, Previtali P, et al. Proteomic
1439 Fingerprint of Lung Fibrosis Progression and Response to Therapy in Bleomycin-Induced
1440 Mouse Model. Int J Mol Sci. Multidisciplinary Digital Publishing Institute (MDPI);
1441 2023;24(5). DOI: 10.3390/ijms24054410

1442 40. Deng X, Liu B, Jiang Q, Li G, Li J, Xu K. CREBH promotes autophagy to ameliorate
1443 NASH by regulating Coro1a. Biochim Biophys Acta Mol Basis Dis. Elsevier B.V.;
1444 2024;1870(1). DOI: 10.1016/j.bbadis.2023.166914

1445 41. Gunasekera DC, Ma J, Vacharathit V, Shah P, Ramakrishnan A, Uprety P, et al. The
1446 development of colitis in Il10 −/− mice is dependent on IL-22. Mucosal Immunol.
1447 Springer Nature; 2020;13(3):493–506. DOI: 10.1038/s41385-019-0252-3

1448 42. Suhail A, Rizvi ZA, Mujagond P, Ali SA, Gaur P, Singh M, et al. DeSUMOylase SENP7-
1449 Mediated Epithelial Signaling Triggers Intestinal Inflammation via Expansion of Gamma-
1450 Delta T Cells. Cell Rep. Elsevier B.V.; 2019;29(11):3522-3538.e7. DOI:
1451 10.1016/j.celrep.2019.11.028

1452 43. Kaminski S, Hermann-Kleiter N, Meisel M, Thuille N, Cronin S, Hara H, et al. Coronin
1453 1A is an essential regulator of the TGFβ receptor/SMAD3 signaling pathway in Th17
1454 CD4 + T cells. J Autoimmun. 2011;37(3):198–208. DOI: 10.1016/j.jaut.2011.05.018

1455 44. Burandt E, Lübbersmeyer F, Gorbokon N, Büscheck F, Luebke AM, Menz A, et al. E-
1456 Cadherin expression in human tumors: a tissue microarray study on 10,851 tumors.
1457 Biomark Res. BioMed Central Ltd; 2021;9(1). DOI: 10.1186/s40364-021-00299-4

1458 45. Rodriguez FJ, Lewis-Tuffin LJ, Anastasiadis PZ. E-cadherin's dark side: Possible role in
1459 tumor progression. Vol. 1826, Biochimica et Biophysica Acta - Reviews on Cancer 2012.
1460 p. 23–31.

1461 46. Popp C, Nichita L, Voiosu T, Bastian A, Cioplea M, Micu G, et al. Expression Profile of
1462 p53 and p21 in Large Bowel Mucosa as Biomarkers of Inflammatory-Related
1463 Carcinogenesis in Ulcerative Colitis. Dis Markers. Hindawi Limited; 2016;2016. DOI:
1464 10.1155/2016/3625279

1465 47. Lu X, Yu Y, Tan S. p53 expression in patients with ulcerative colitis - associated with
1466 dysplasia and carcinoma: A systematic meta-analysis. BMC Gastroenterol. BioMed
1467 Central Ltd.; 2017;17(1). DOI: 10.1186/s12876-017-0665-y

1468 48. Khursheed S, Ali T, Mushtaq M, Humayun S, Khan A, Akbar A, et al.
1469 Immunohistochemical Analysis of the p53 Protein in Colorectal Cancer: A
1470 Clinicopathological Study. Cureus. Springer Science and Business Media LLC; 2024;
1471 DOI: 10.7759/cureus.76172

1472 49. Suarez-Lopez L, Sriram G, Kong YW, Morandell S, Merrick KA, Hernandez Y, et al.
1473 MK2 contributes to tumor progression by promoting M2 macrophage polarization and
1474 tumor angiogenesis. Proc Natl Acad Sci U S A. National Academy of Sciences;
1475 2018;115(18):E4236–44. DOI: 10.1073/pnas.1722020115

1476 50. Zhang F, Wang H, Wang X, Jiang G, Liu H, Zhang G, et al. TGF-β induces M2-like
1477 macrophage polarization via SNAIL-mediated suppression of a pro-inflammatory
1478 phenotype [Internet]. Vol. 7 2016 [cited. Available from:
1479 www.impactjournals.com/oncotarget

1480 51. Deng Z, Fan T, Xiao C, Tian H, Zheng Y, Li C, et al. TGF-β signaling in health, disease,
1481 and therapeutics. Vol. 9, Signal Transduction and Targeted Therapy Springer Nature;
1482 2024.

1483 52. Massagué J. TGFβ signalling in context. Vol. 13, Nature Reviews Molecular Cell Biology
1484 2012. p. 616–30.

1485 53. Jayachandran R, Sundaramurthy V, Combaluzier B, Mueller P, Korf H, Huygen K, et al.
1486 Survival of Mycobacteria in Macrophages Is Mediated by Coronin 1-Dependent

1487 Activation of Calcineurin. Cell. Elsevier B.V.; 2007;130(1):37–50. DOI:
1488 10.1016/j.cell.2007.04.043

1489 54. Suo D, Park J, Harrington AW, Zweifel LS, Mihalas S, Deppmann CD. Coronin-1 is a
1490 neurotrophin endosomal effector that is required for developmental competition for
1491 survival. Nat Neurosci. 2014;17(1):36–45. DOI: 10.1038/nn.3593

1492 55. Huang W, Ghisletti S, Saijo K, Gandhi M, Aouadi M, Tesz GJ, et al. Coronin 2A mediates
1493 actin-dependent de-repression of inflammatory response genes. Nature.
1494 2011;470(7334):414–8. DOI: 10.1038/nature09703

1495 56. Kerscher O. SUMO junction - What's your function? New insights through SUMO-
1496 interacting motifs. Vol. 8, EMBO Reports 2007. p. 550–5.

1497 57. Song J, Durrin LK, Wilkinson TA, Krontiris TG, Chen Y. Identification of a SUMO-
1498 binding motif that recognizes SUMO-modified proteins [Internet]. Vol. 101 2004 [cited.
1499 Available from: www.pnas.orgcgidoi10.1073pnas.0403498101

1500 58. Gou Y, Liu D, Chen M, Wei Y, Huang X, Han C, et al. GPS-SUMO 2.0: an updated
1501 online service for the prediction of SUMOylation sites and SUMO-interacting motifs.
1502 Nucleic Acids Res. Oxford University Press; 2024;52(W1):W238–47. DOI:
1503 10.1093/nar/gkae346

1504 59. Beauclair G, Bridier-Nahmias A, Zagury JF, Säb A, Zamborlini A. JASSA: A
1505 comprehensive tool for prediction of SUMOylation sites and SIMs. Bioinformatics.
1506 Oxford University Press; 2015;31(21):3483–91. DOI: 10.1093/bioinformatics/btv403

1507 60. Rytinki MM, Palvimo JJ. SUMOylation attenuates the function of PGC-1α. Journal of
1508 Biological Chemistry. 2009;284(38):26184–93. DOI: 10.1074/jbc.M109.038943

1509 61. Niu X, Xu C, Cheuk YC, Xu X, Liang L, Zhang P, et al. Characterizing hub biomarkers
1510 for post-transplant renal fibrosis and unveiling their immunological functions through
1511 RNA sequencing and advanced machine learning techniques. J Transl Med. BioMed
1512 Central Ltd; 2024;22(1). DOI: 10.1186/s12967-024-04971-9

1513 62. Elihamu D, Li Y, Wang Y, Cui H, Xing Y, Peng H, et al. CORO1A: a pan-cancer
1514 prognosis, diagnostic and immune biomarker based on breast cancer validation. Front
1515 Oncol. Frontiers Media SA; 2025;15. DOI: 10.3389/fonc.2025.1670526

1516 63. Kros JM, Zeneyedpour L, Pedrosa RMSM, Belcaid Z, Dik WA, Luider TM, et al. T cell
1517 induced expression of Coronin-1A facilitates blood-brain barrier transmigration of breast
1518 cancer cells. Sci Rep. Nature Research; 2024;14(1). DOI: 10.1038/s41598-024-83301-x

1519 64. Li Z, Chen L, Wei Z, Liu H, Zhang L, Huang F, et al. A novel classification method for
1520 LUAD that guides personalized immunotherapy on the basis of the cross-talk of

1521 coagulation- and macrophage-related genes. Front Immunol. Frontiers Media SA;
1522 2025;16. DOI: 10.3389/fimmu.2025.1518102

1523 65. Sun Y, Ma Q, Chen Y, Liao D, Kong F. Identification and analysis of prognostic immune
1524 cell homeostasis characteristics in lung adenocarcinoma. Clinical Respiratory Journal.
1525 John Wiley and Sons Inc; 2024;18(5). DOI: 10.1111/crj.13755

1526 66. Zhou Y, Shi X, Chen H, Mao B, Song X, Gao L, et al. Tumor Immune Microenvironment
1527 Characterization of Primary Lung Adenocarcinoma and Lymph Node Metastases. Biomed
1528 Res Int. Hindawi Limited; 2021;2021. DOI: 10.1155/2021/5557649

1529 67. Bao M, Huang Y, Lang Z, Zhao H, Saito Y, Nagano T, et al. Proteomic analysis of plasma
1530 exosomes in patients with non-small cell lung cancer. Transl Lung Cancer Res. AME
1531 Publishing Company; 2022;11(7):1434–52. DOI: 10.21037/tlcr-22-467

1532 68. Kumar P, Nandi S, Tan TZ, Ghee Ler S, Chia KS, Lim W-Y, et al. Highly sensitive and
1533 specific novel biomarkers for the diagnosis of transitional bladder carcinoma [Internet].
1534 Available from: www.impactjournals.com/oncotarget/

1535 69. Jayachandran R, Gumienny A, Bolinger B, Ruehl S, Lang MJ, Fucile G, et al. Disruption
1536 of Coronin 1 Signaling in T Cells Promotes Allograft Tolerance while Maintaining Anti-
1537 Pathogen Immunity. Immunity. Cell Press; 2019;50(1):152-165.e8. DOI:
1538 10.1016/j.immuni.2018.12.011

1539 70. Ndinyanka Fabrice T, Buczak K, Schmidt A, Pieters J. T cell population size control by
1540 coronin 1 uncovered: from a spot identified by two-dimensional gel electrophoresis to
1541 quantitative proteomics. Vol. 22, Expert Review of Proteomics Taylor and Francis Ltd.;
1542 2025. p. 35–44.

1543 71. Jayachandran R, Pieters J. Regulation of immune cell homeostasis and function by
1544 coronin 1. Vol. 28, International Immunopharmacology Elsevier B.V.; 2015. p. 825–8.

1545 72. Shiow LR, Paris K, Akana MC, Cyster JG, Sorensen RU, Puck JM. Severe combined
1546 immunodeficiency (SCID) and attention deficit hyperactivity disorder (ADHD) associated
1547 with a coronin-1A mutation and a chromosome 16p11.2 deletion. Clinical Immunology.
1548 2009;131(1):24–30. DOI: 10.1016/j.clim.2008.11.002

1549 73. Younis DA, Marosvari M, Liu W, Pulikkot S, Cao Z, Zhou B, et al. CFTR dictates
1550 monocyte adhesion by facilitating integrin clustering but not activation. Proc Natl Acad
1551 Sci U S A. National Academy of Sciences; 2025;122(3). DOI: 10.1073/pnas.2412717122

1552 74. Deng Z, Fan T, Xiao C, Tian H, Zheng Y, Li C, et al. TGF-β signaling in health, disease,
1553 and therapeutics. Vol. 9, Signal Transduction and Targeted Therapy Springer Nature;
1554 2024.

1555 75. Fridlender ZG, Sun J, Kim S, Kapoor V, Cheng G, Ling L, et al. Polarization of Tumor-
1556 Associated Neutrophil Phenotype by TGF-β: "N1" versus "N2" TAN. Cancer Cell. Cell
1557 Press; 2009;16(3):183–94. DOI: 10.1016/j.ccr.2009.06.017

1558 76. Gong D, Shi W, Yi S ju, Chen H, Groffen J, Heisterkamp N. TGFβ signaling plays a
1559 critical role in promoting alternative macrophage activation. BMC Immunol. 2012;13.
1560 DOI: 10.1186/1471-2172-13-31

1561 77. Lin CS, Chen MF, Wang YS, Chuang TF, Chiang YL, Chu RM. IL-6 restores dendritic
1562 cell maturation inhibited by tumor-derived TGF-β through interfering Smad 2/3 nuclear
1563 translocation. Cytokine. 2013;62(3):352–9. DOI: 10.1016/j.cyto.2013.03.005

1564 78. Mckarns SC, Schwartz RH, Kaminski NE. Smad3 Is Essential for TGF-1 to Suppress IL-2
1565 Production and TCR-Induced Proliferation, but Not IL-2-Induced Proliferation1 [Internet].
1566 2004 [cited. Available from:
1567 https://academic.oup.com/jimmunol/article/172/7/4275/8060313

1568 79. Strobl H, Knapp W. TGF-1 regulation of dendritic cells TGF-/ dendritic cell / Langerhans
1569 cell / differentiation / antigen presentation. 1999.

1570 80. Calon A, Espinet E, Palomo-Ponce S, Tauriello DVF, Iglesias M, Céspedes MV, et al.
1571 Dependency of Colorectal Cancer on a TGF-β-Driven Program in Stromal Cells for
1572 Metastasis Initiation. Cancer Cell. Cell Press; 2012;22(5):571–84. DOI:
1573 10.1016/j.ccr.2012.08.013

1574 81. Means AL, Freeman TJ, Zhu J, Woodbury LG, Marincola-Smith P, Wu C, et al. Epithelial
1575 Smad4 Deletion Up-Regulates Inflammation and Promotes Inflammation-Associated
1576 Cancer. CMGH. Elsevier Inc; 2018;6(3):257–76. DOI: 10.1016/j.jcmgh.2018.05.006

1577 82. Gong D, Shi W, Yi S ju, Chen H, Groffen J, Heisterkamp N. TGFβ signaling plays a
1578 critical role in promoting alternative macrophage activation. BMC Immunol. 2012;13.
1579 DOI: 10.1186/1471-2172-13-31

1580 83. Chan MKK, Chung JYF, Tang PCT, Chan ASW, Ho JYY, Lin TPT, et al. TGF-β
1581 signaling networks in the tumor microenvironment. Vol. 550, Cancer Letters Elsevier
1582 Ireland Ltd; 2022.

1583 84. Li J, Liu Y, Wang B, Xu Y, Ma A, Zhang F, et al. Myeloid TGF-β signaling contributes to
1584 colitis-associated tumorigenesis in mice. Carcinogenesis. 2013;34(9):2099–108. DOI:
1585 10.1093/carcin/bgt172

1586 85. Wang W, Li X, Zheng D, Zhang D, Peng X, Zhang X, et al. Dynamic changes and
1587 functions of macrophages and M1/M2 subpopulations during ulcerative colitis-associated
1588 carcinogenesis in an AOM/DSS mouse model. Mol Med Rep. Spandidos Publications;
1589 2015;11(4):2397–406. DOI: 10.3892/mmr.2014.3018

1590 86. Zadka Ł, Chabowski M, Grybowski D, Piotrowska A, Dzięgiel P. Interplay of stromal
1591 tumor-infiltrating lymphocytes, normal colonic mucosa, cancer-associated fibroblasts,
1592 clinicopathological data and the immunoregulatory molecules of patients diagnosed with
1593 colorectal cancer. Cancer Immunology, Immunotherapy. Springer Science and Business
1594 Media Deutschland GmbH; 2021;70(9):2681–700. DOI: 10.1007/s00262-021-02863-1

1595 87. Kazuko Saeki, Akihiko Yoshimura. The B-cell-specific major raft protein, Raftlin, is
1596 necessary for the integrity of lipid raft and BCR signal transduction. EMBO.
1597 2003;12:3015–26.

1598 88. Saeki K, Fukuyama S, Ayada T, Nakaya M, Aki D, Takaesu G, et al. A Major Lipid Raft
1599 Protein Raftlin Modulates T Cell Receptor Signaling and Enhances Th17-Mediated
1600 Autoimmune Responses. The Journal of Immunology. Oxford University Press (OUP);
1601 2009;182(10):5929–37. DOI: 10.4049/jimmunol.0802672

1602 89. Watanabe A, Tatematsu M, Saeki K, Shibata S, Shime H, Yoshimura A, et al. Raftlin is
1603 involved in the nucleocapture complex to induce poly(I:C)-mediated TLR3 activation.
1604 Journal of Biological Chemistry. American Society for Biochemistry and Molecular
1605 Biology Inc.; 2011;286(12):10702–11. DOI: 10.1074/jbc.M110.185793

1606 90. Bayliss AL, Sundararaman A, Granet C, Mellor H. Raftlin is recruited by neuropilin-1 to
1607 the activated VEGFR2 complex to control proangiogenic signaling. Angiogenesis.
1608 Springer; 2020;23(3):371–83. DOI: 10.1007/s10456-020-09715-z

1609 91. Tatematsu M, Yoshida R, Morioka Y, Ishii N, Funami K, Watanabe A, et al. Raftlin
1610 Controls Lipopolysaccharide-Induced TLR4 Internalization and TICAM-1 Signaling in a
1611 Cell Type–Specific Manner. The Journal of Immunology. Oxford University Press (OUP);
1612 2016;196(9):3865–76. DOI: 10.4049/jimmunol.1501734

1613 92. Lacy MM, Ma R, Ravindra NG, Berro J. Molecular mechanisms of force production in
1614 clathrin-mediated endocytosis. Vol. 592, FEBS Letters Wiley Blackwell; 2018. p. 3586–
1615 605.

1616 93. Mustfa SA, Singh M, Suhail A, Mohapatra G, Verma S, Chakravorty D, et al.
1617 SUMOylation pathway alteration coupled with downregulation of SUMO E2 enzyme at
1618 mucosal epithelium modulates inflammation in inflammatory bowel disease. Open Biol.
1619 Royal Society Publishing; 2017;7(6). DOI: 10.1098/rsob.170024

1620 94. Toda G, Yamauchi T, Kadowaki T, Ueki K. Preparation and culture of bone marrow-
1621 derived macrophages from mice for functional analysis. STAR Protoc. Cell Press;
1622 2021;2(1). DOI: 10.1016/j.xpro.2020.100246

1623 95. Weigmann B, Tubbe I, Seidel D, Nicolaev A, Becker C, Neurath MF. Isolation and
1624 subsequent analysis of murine lamina propria mononuclear cells from colonic tissue. Nat
1625 Protoc. 2007;2(10):2307–11. DOI: 10.1038/nprot.2007.315

1626

- 1. Dynamic expression pattern of SENP5 in chronic colitis and colitis-associated colorectal cancer (CAC)

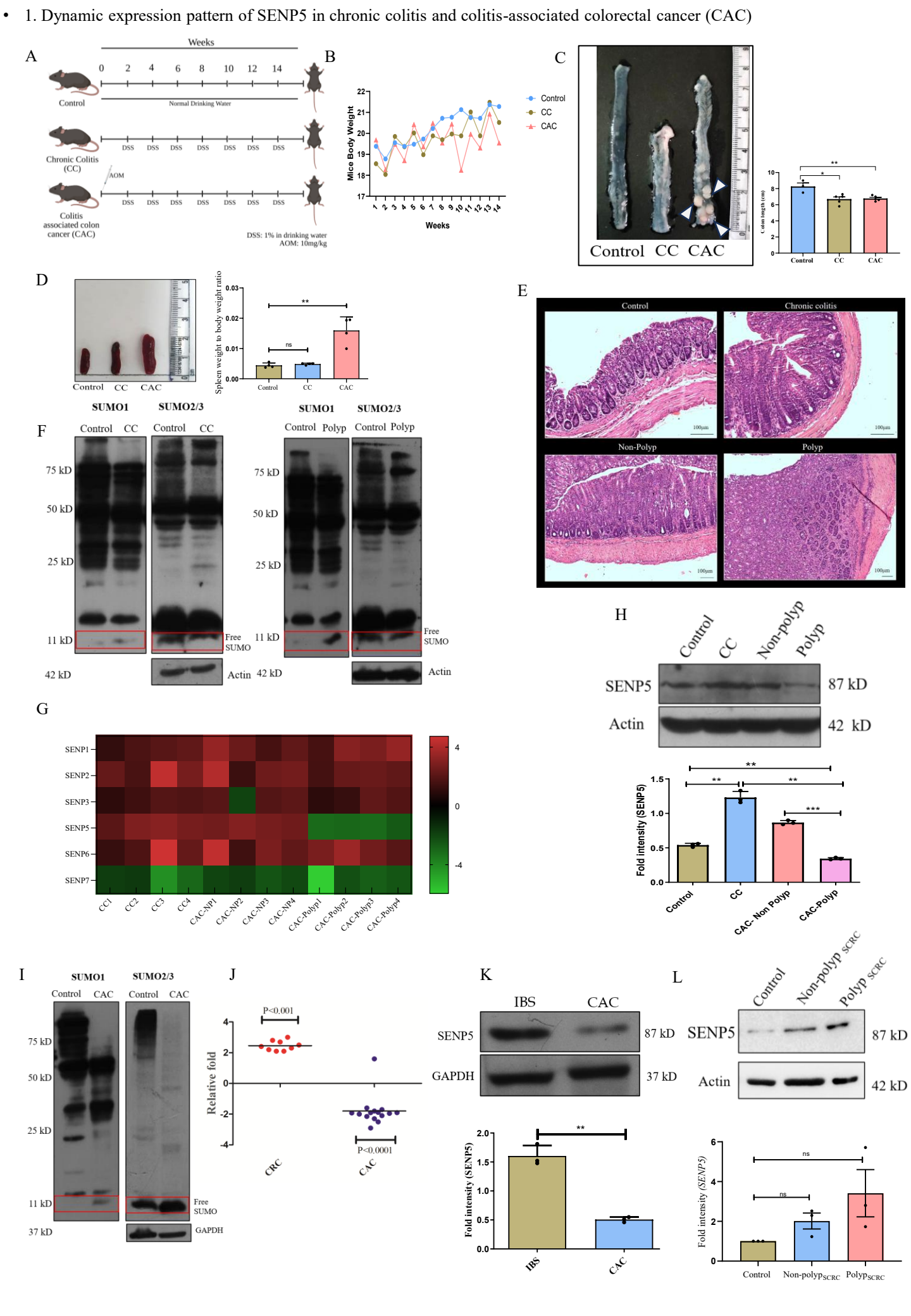

- 2. Altered interactome of SENP5 in Chronic colitis and colitis-associated colorectal cancer (CAC)

A

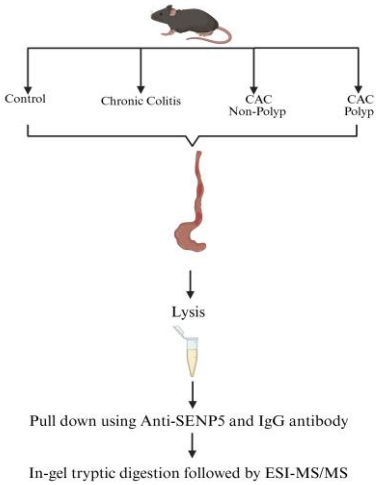

B

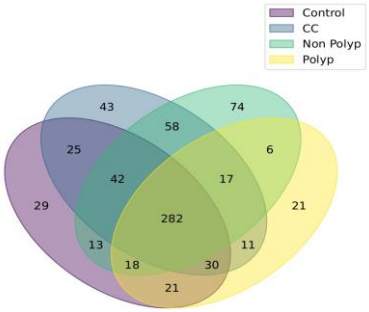

Sample Name	Number of Unique Elements
Control	460
Chronic colitis	508
NP CAC	510
Polyp CAC	406

Parameters	Values
Peptide tolerance	0.5 Da
Significant Threshold	0.05
Protein FDR	5 %
MS/MS tolerance	50ppm

C

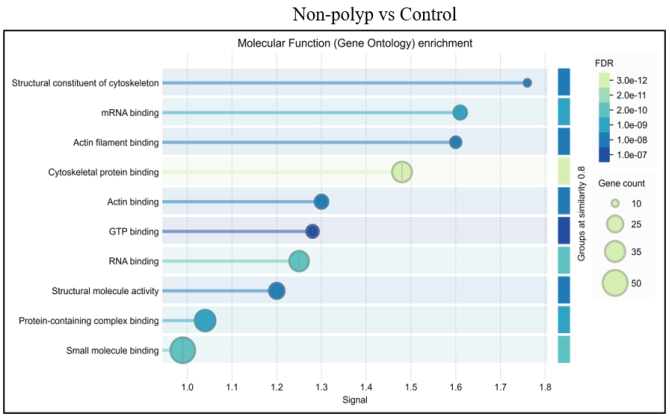

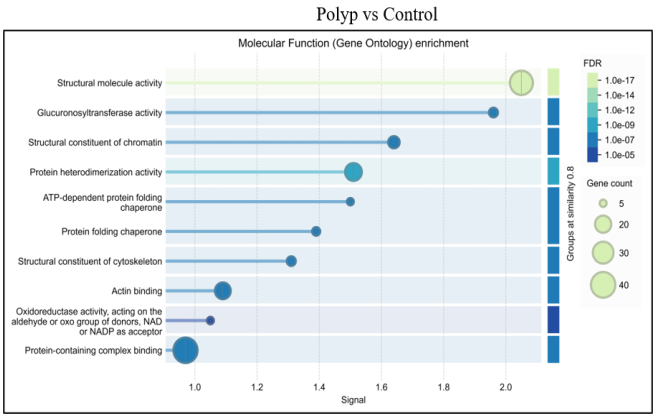

D

Name of the Protein	Condition of identification	Presence of SUMOylation and/or SIM site	Function and disease reported	References
Coronin1A (Coro1a)	Control, CC, Non-Polyp and Polyp	20, 461, 200-204, 155-159	Cytoskeleton remodeling, immune cells maturation and trafficking.	*Pick R. et al. Blood, 2017 Jean Pieters et al. Nat. Rev. 2013*
Myosin-9 (Myh9)	Control, CC, Non-Polyp and Polyp	47, 82,180, 228,289, 580, 778,	Cell adhesion, migration. Involved in the EMT process. Play role in SCRC.	*Yan Zhong et al. Cell Death and Differentiation, 2021 Zixuan Gou et al. Rev. Frontier 2021.*
Tropomyosin 4 (Tmp4)	Control, CC, Non-Polyp and Polyp	104, 113, 153, 125, 190, 56-60, 189-193	Binds actin filaments in muscle and non-muscle cells. Act as Tumor suppressor in SCRC	*Rui Yang et al. Biomed. 2018, Piesi Li et al. Cell Death and Disease 2024*
Collagen alpha-3(VI) (Col6a3)	Control, CC, Non-Polyp and Polyp	32, 98, 698, 504, 242-246, 278-282	Key structural component of VI collagen, part of the ECM. Predominantly expressed in the stroma of the tumor. Serves as a stromal-specific diagnostic marker.	*Jie Qiao et al. Oncotarget, 2015 Wei Liu et al. Oncol Reports, 2018*
Cytoplasmic Dynein 1 heavy chain 1 (Dync1h1)	Control, CC, Non-Polyp and Polyp		Key motor protein involved in retrograde transport, intracellular cargo trafficking, and cytoskeleton organization Promote proliferation in gastric cancer	*Hongyu Pan et al. Expt. Cell Research, 2021.*

E

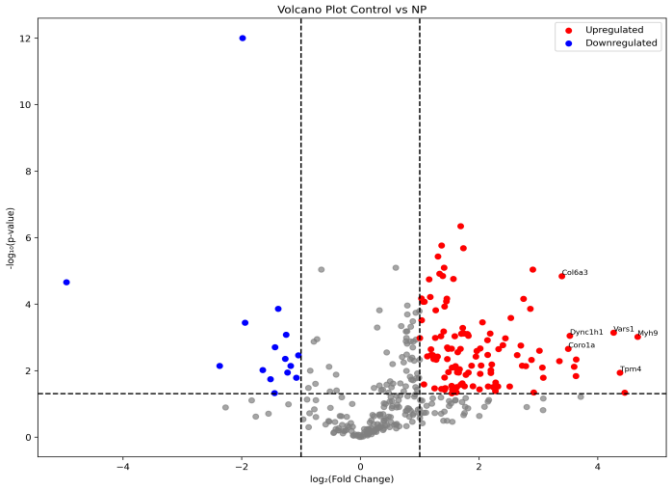

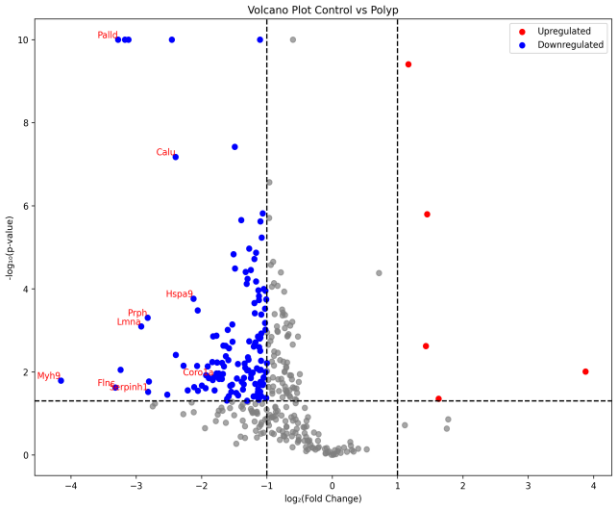

- 3. Coro1A as an interactor of SENP5

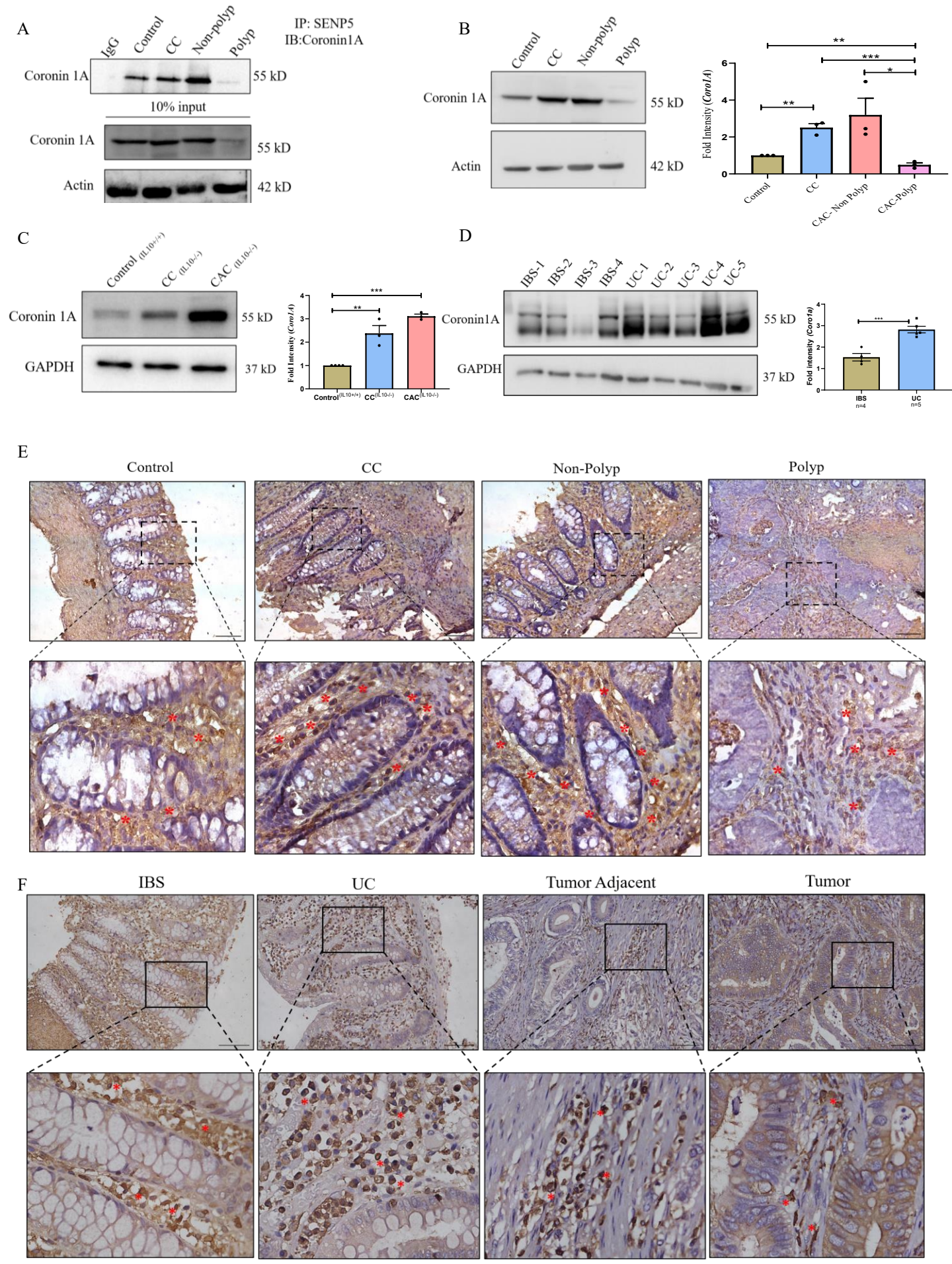

- 4. Absence of Coro 1A confers resistance to CAC development in mice

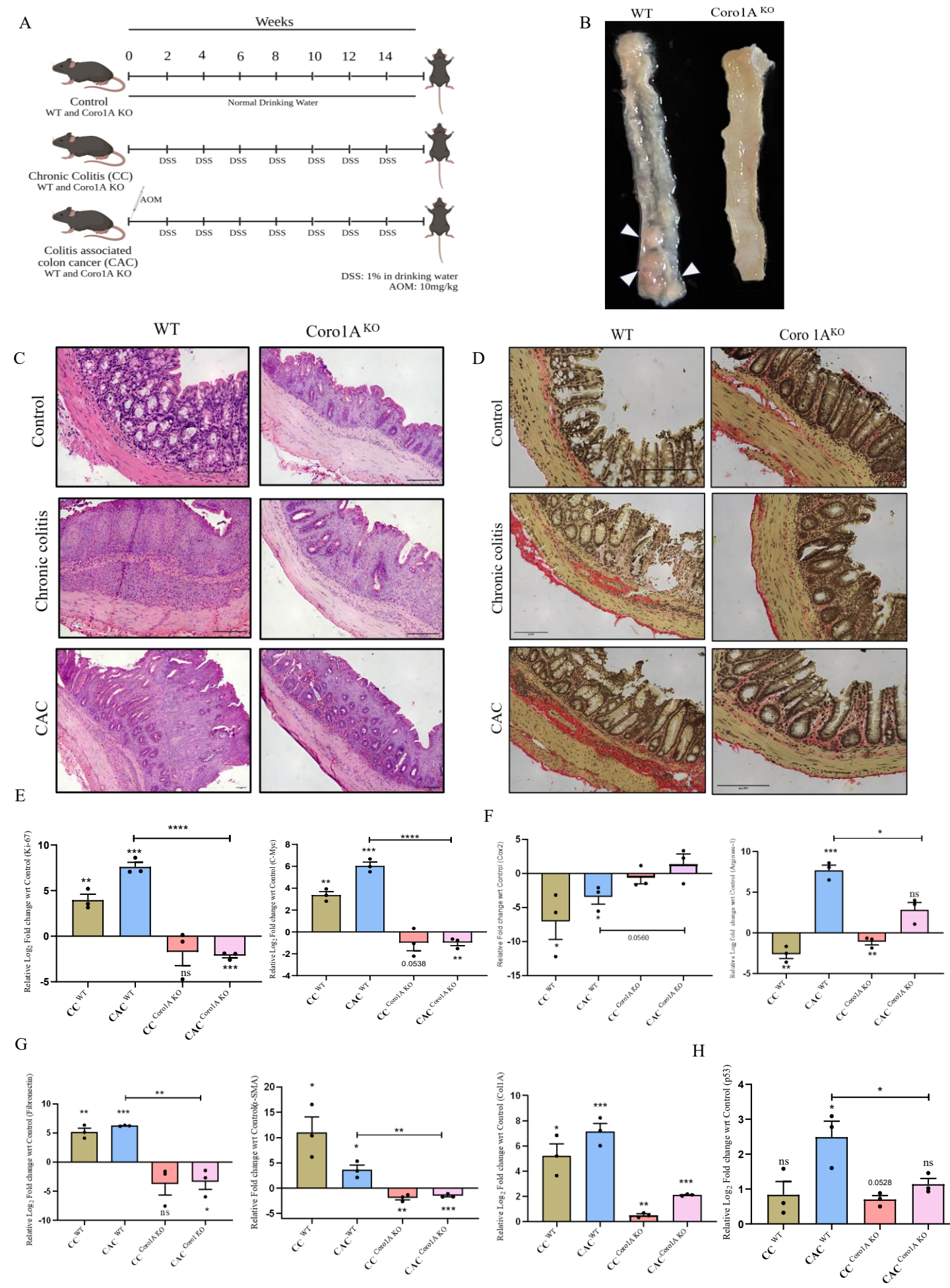

- 5. Increased expression of Coro1A is associated with M2 macrophages

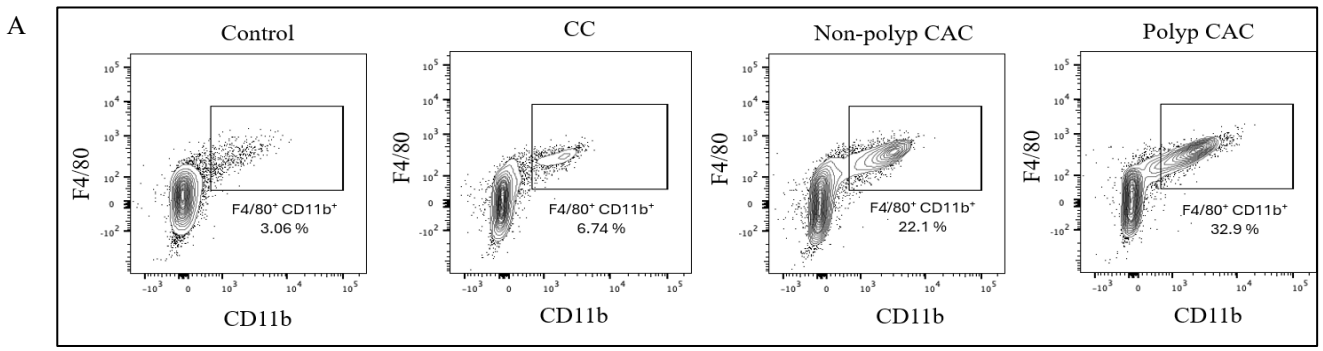

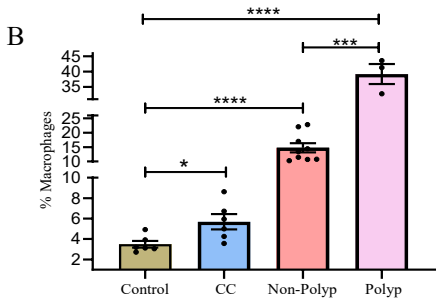

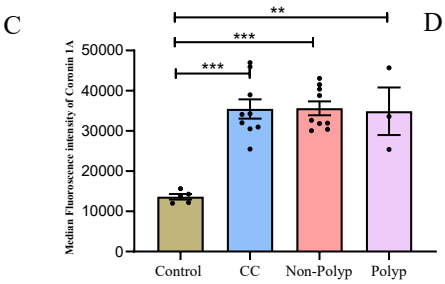

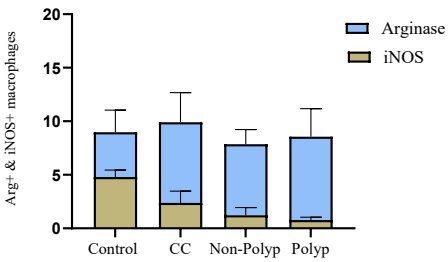

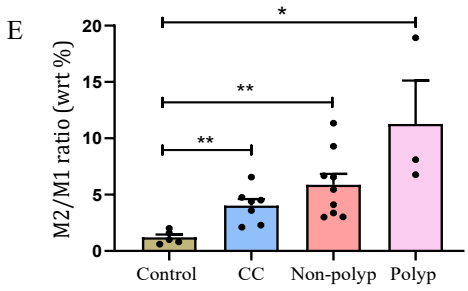

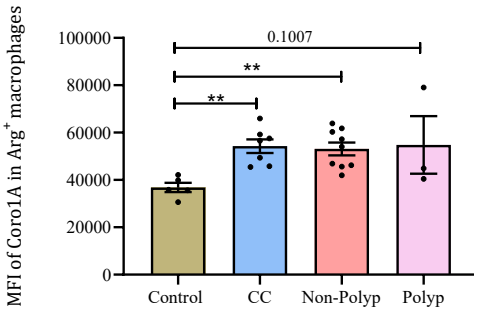

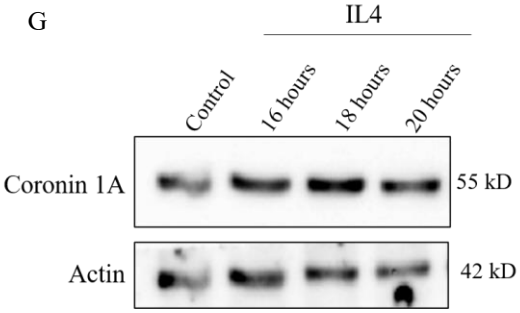

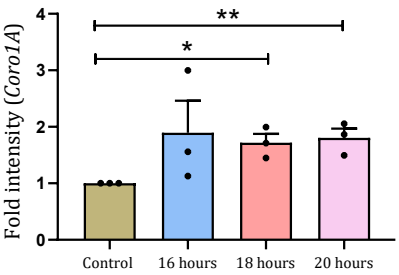

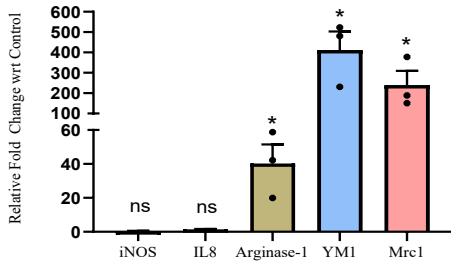

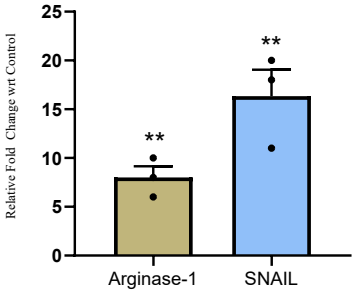

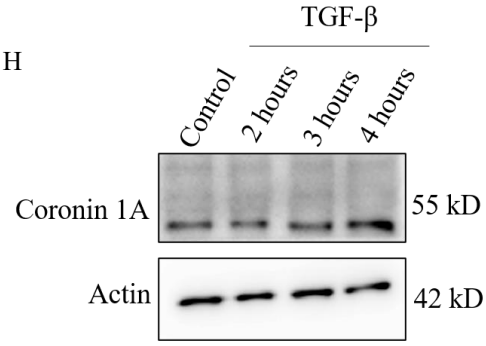

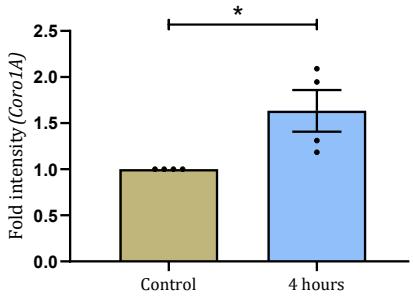

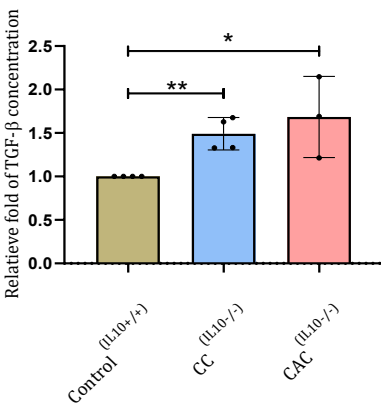

- 6. Coro 1A interacts directly with the TGF-β RI and controls TGF-β-mediated M2 macrophage polarization

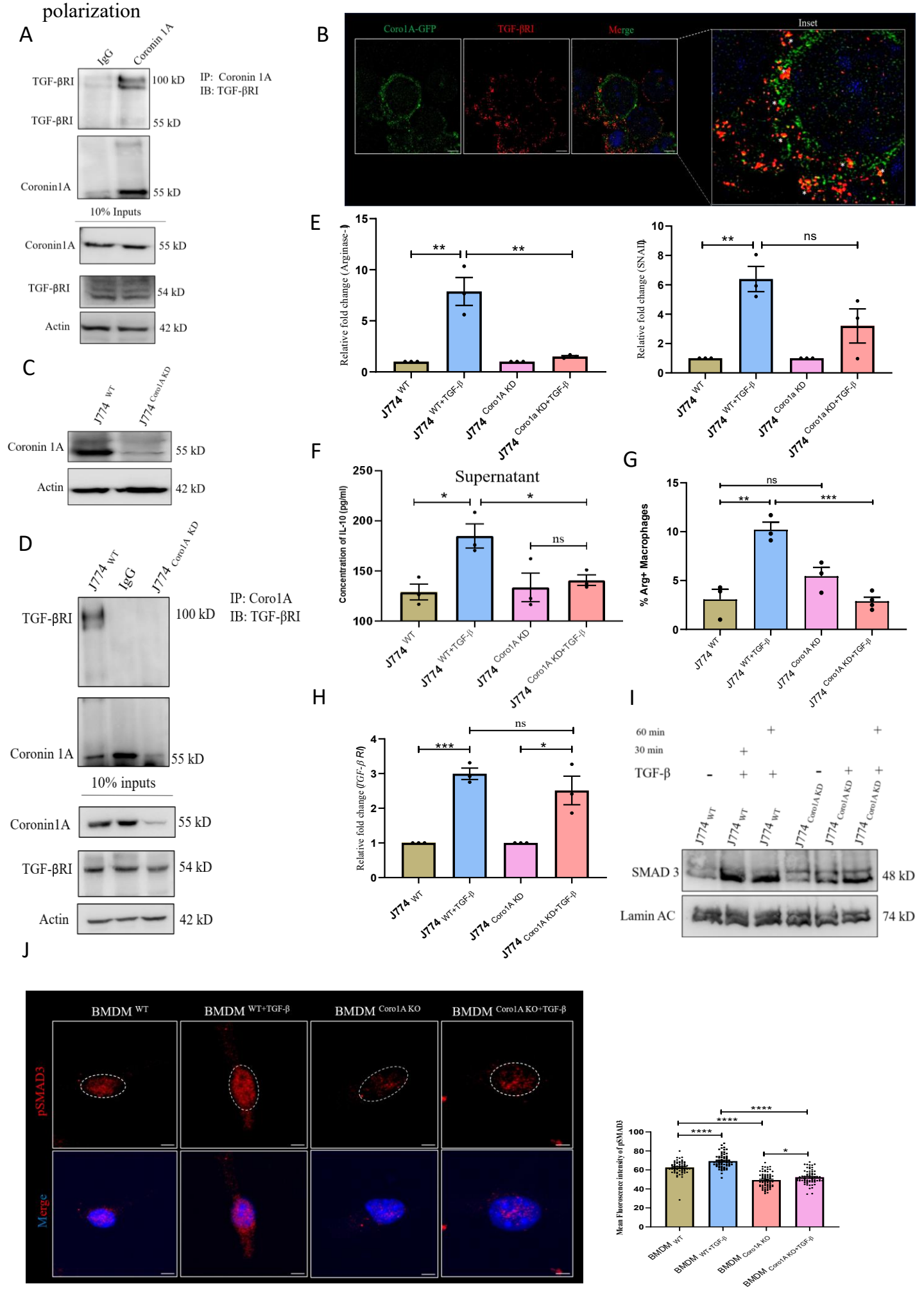

- 7. Coro1A is required for the stability of TGF-βRI

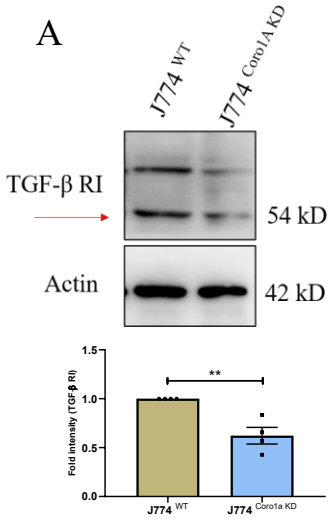

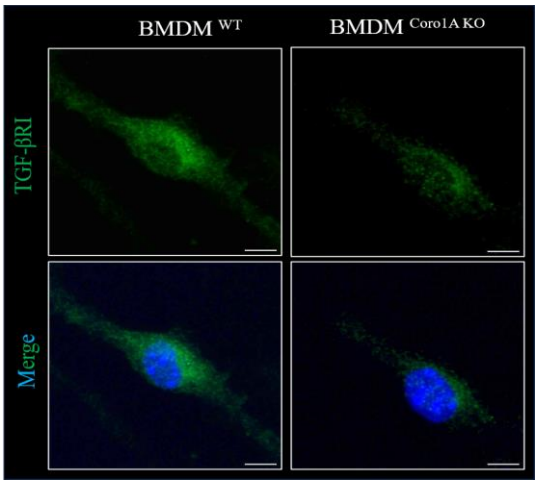

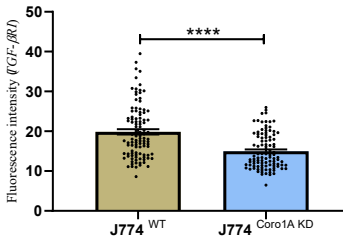

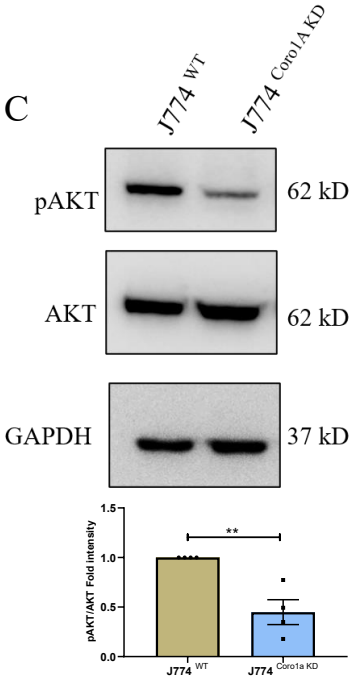

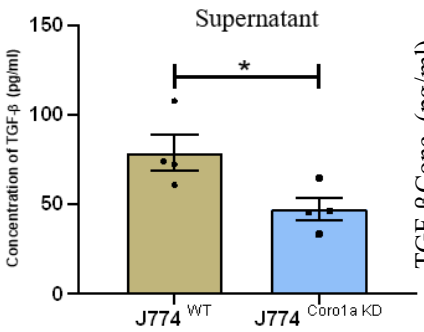

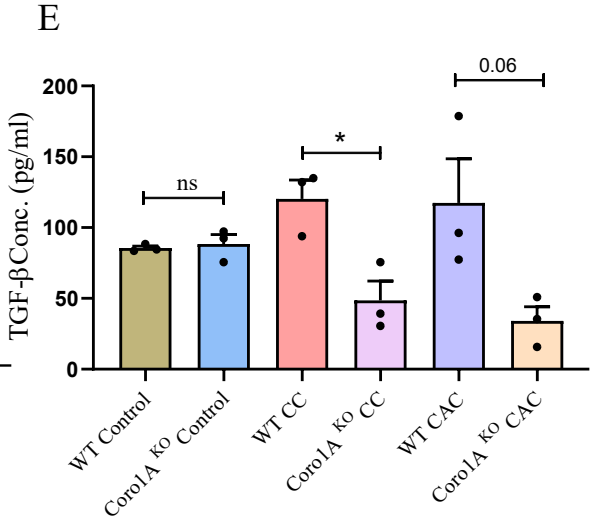

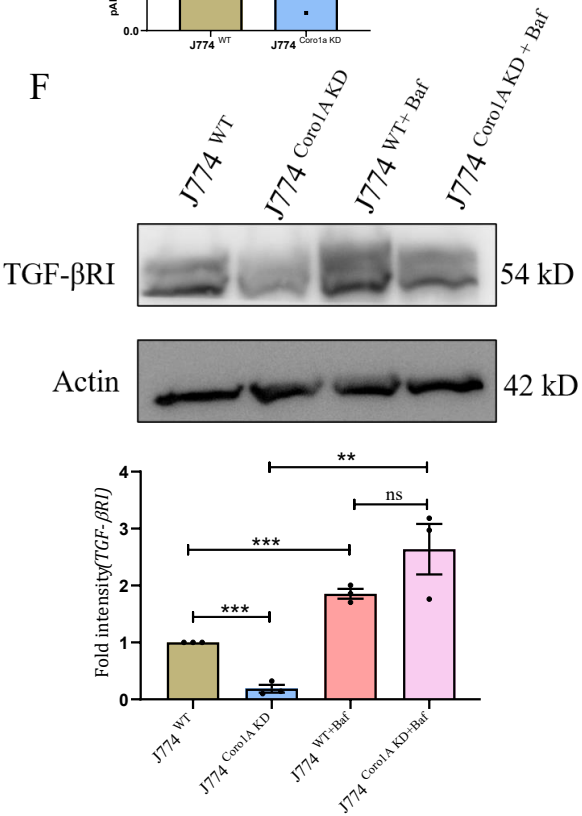

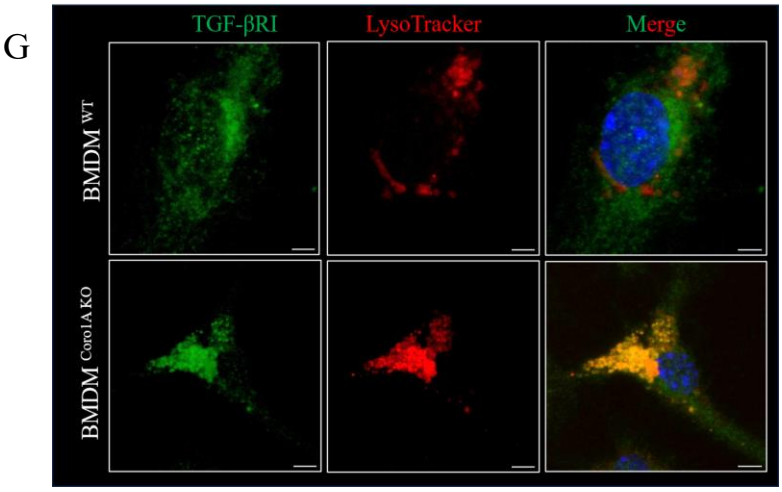

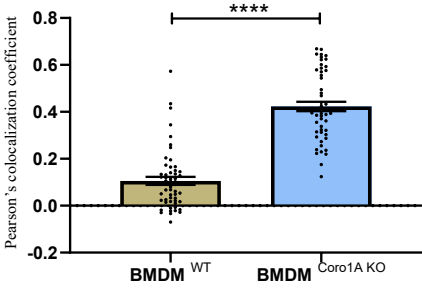

- 8. Coro1A utilizes the calcium-calcineurin signaling pathway to protect TGF-βRI from degradation

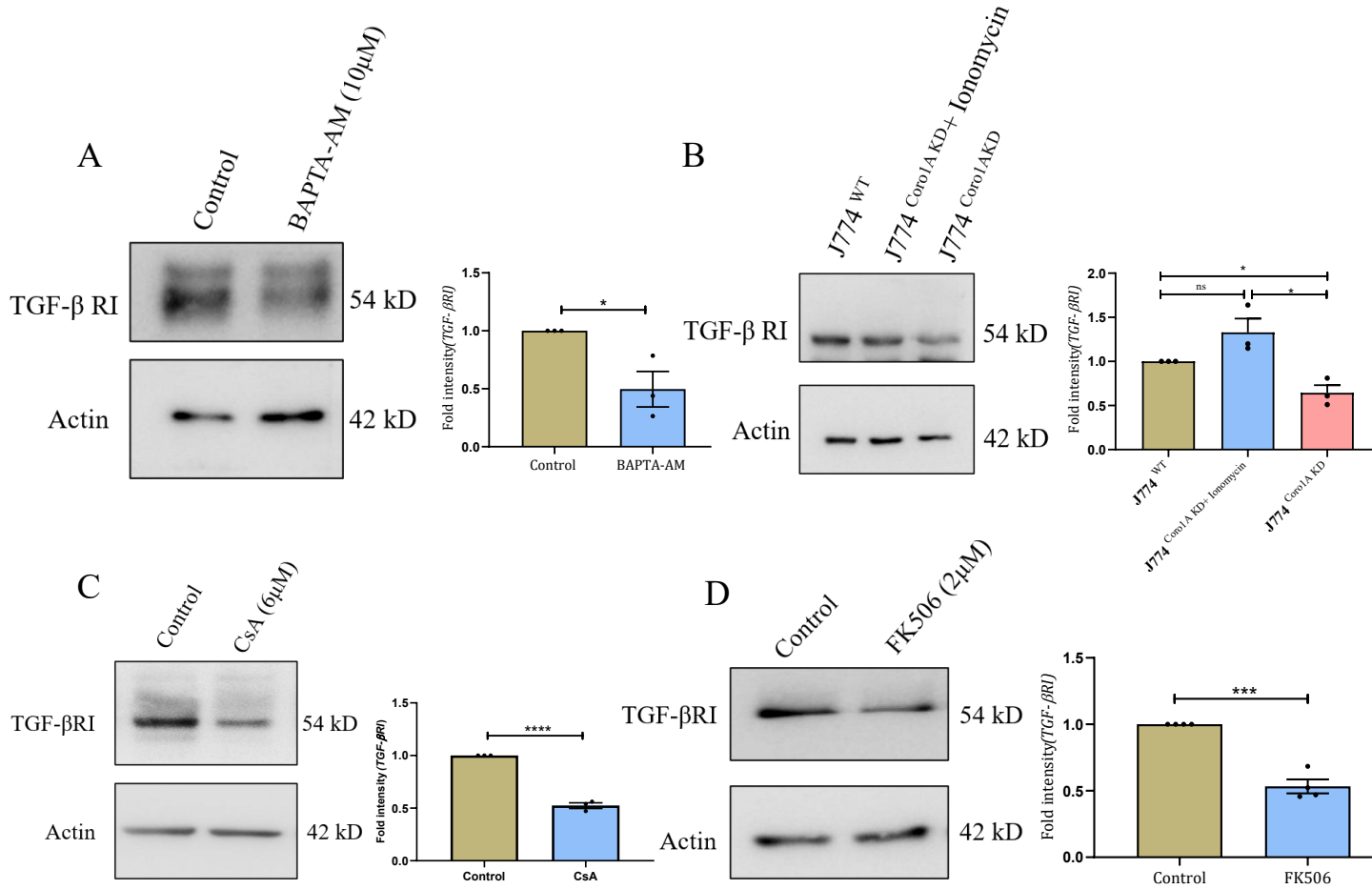

- 9. SUMO2/3 governs stability of Coro1A

A

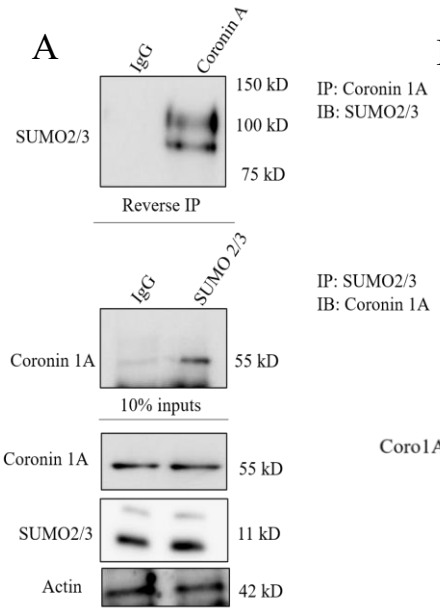

IP: Coronin 1A
IB: SUMO2/3

IP: SUMO2/3
IB: Coronin 1A

B

Protein	GPS	JASSA
Coronin 1a	SIM sites	SIM sites
	155-159	155-159 (High)
	167-171	167-171(High)
	124-128	124-128 (High)
	281-285 (High)	84-87
	440-444	200-204

C

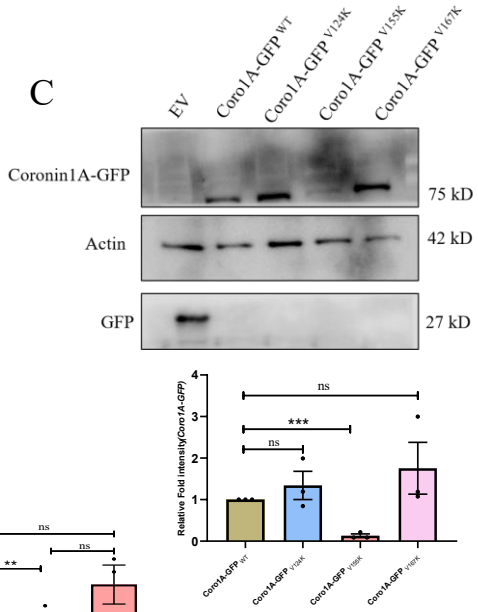

D

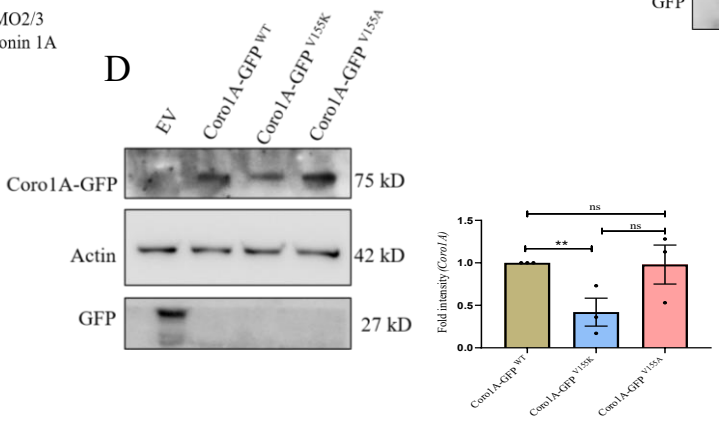

E

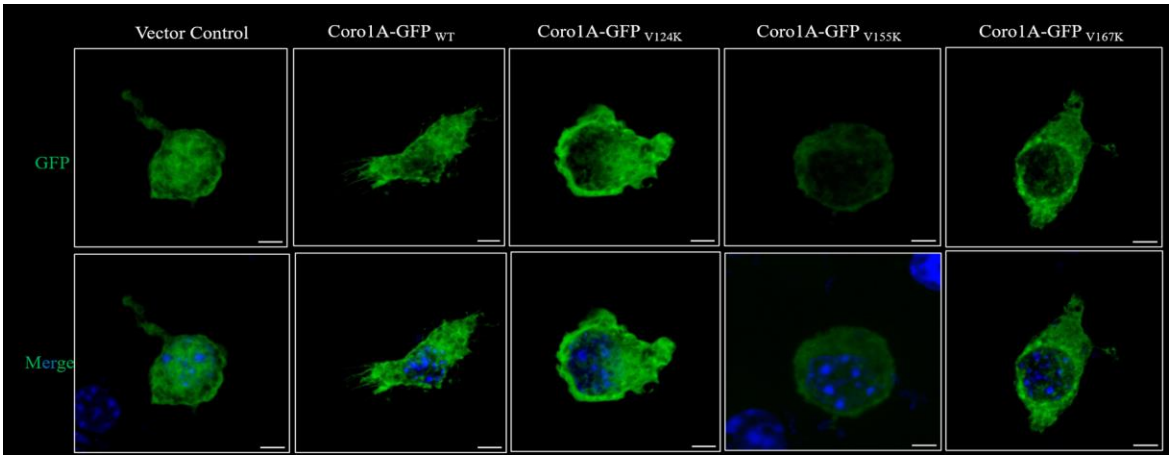

F

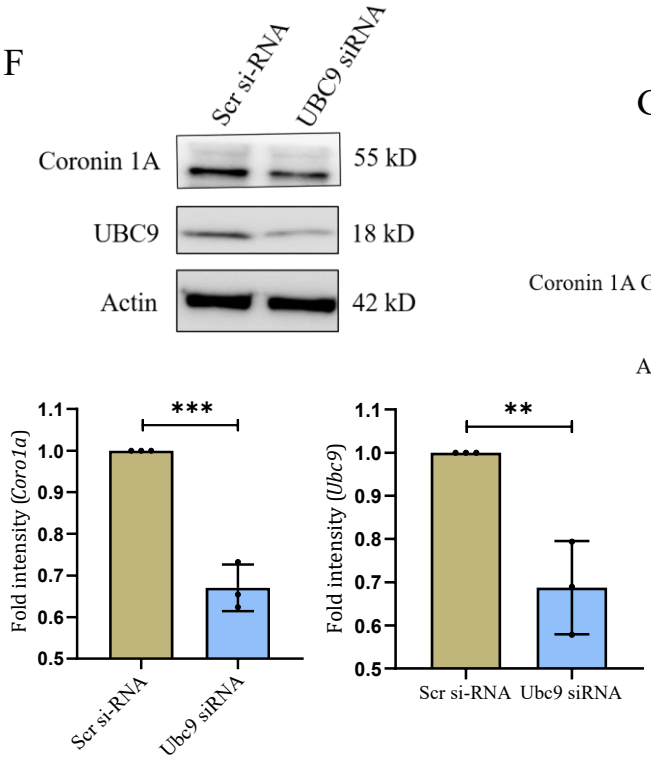

G

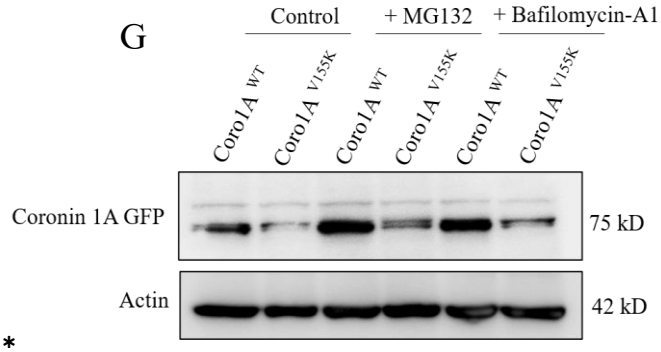

- 10. Coro1A interacts with SUMOylated Raftlin through the SIM site

A

Gene ID	Name of protein	Gene Name	Class of protein
Q6A0D4	Raftlin	Rftn1	Clatherin-AP binding protein
Q5NCX5	Neuralised like protein 4	Neurl4	Ubiquitin protein ligaseQ
Q8BTF7	DNA Ligase	Lig4	DNA metabolism Protein
Q9R087	Glypican-6	Gpc6	Scaffold/adaptor protein
Q8BGQ6	EF-hand calcium-binding domain-containing protein-14	Efcab14	-
Q0VBP7	Protein shisa like -1	Shisal1	Scaffold/adaptor protein

B

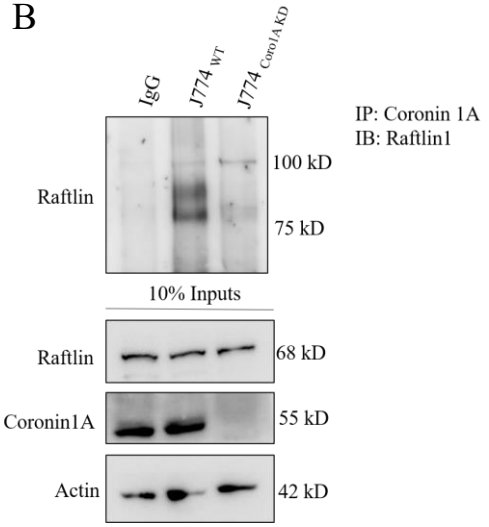

C

Protein	GPS-SUMO	JASSA
	SUMO binding sites	
Raftlin	K31	K31 (High)
	K224	K224 (High)
	K206	
	K381	
	K481	
	K191	

D

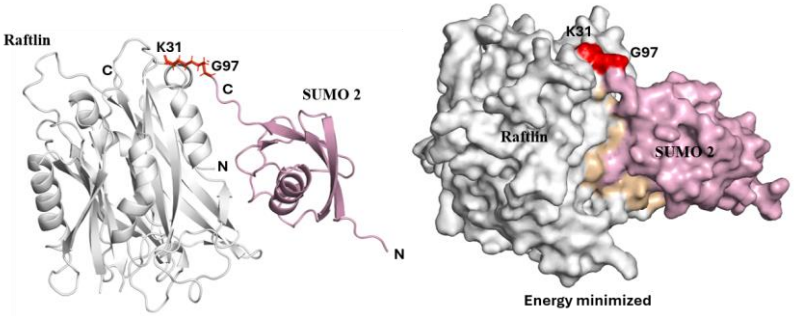

E

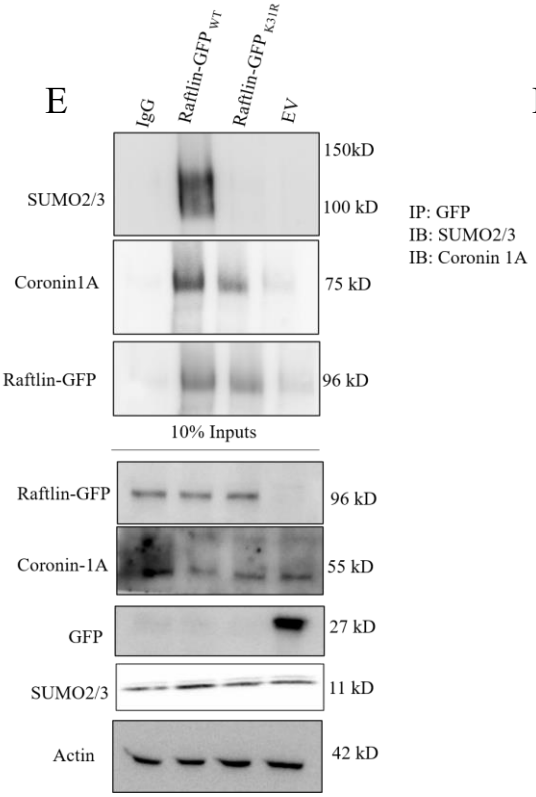

F

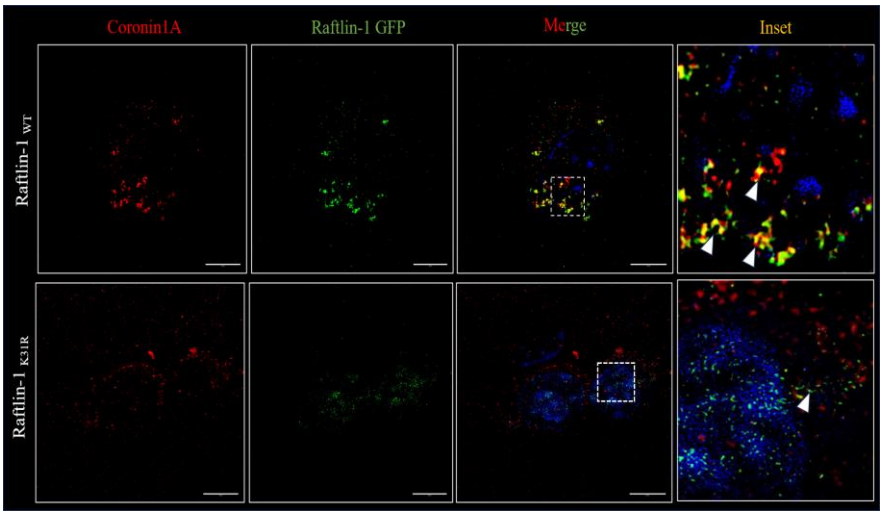

G

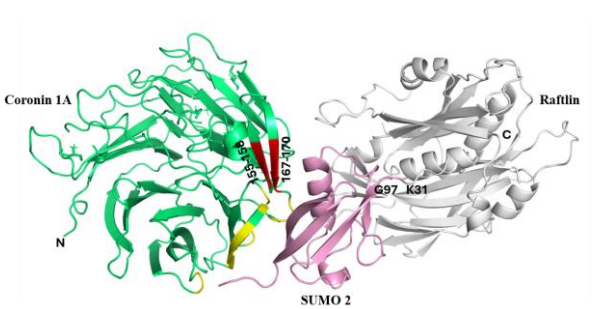

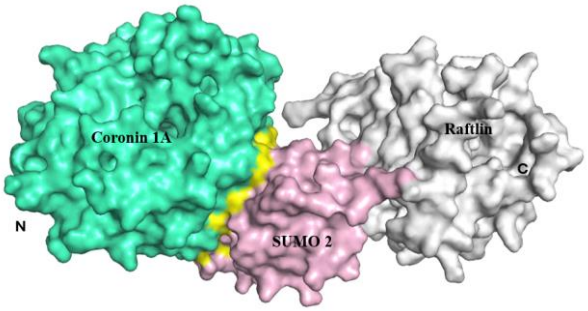

- Supplementary Figure 01:

A

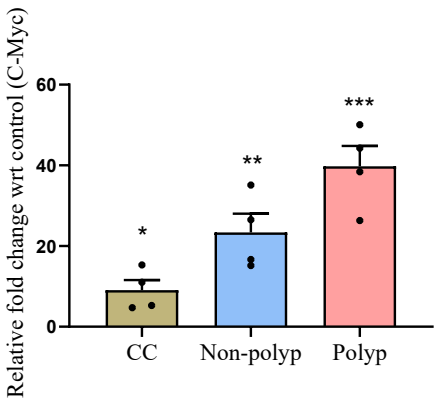

B

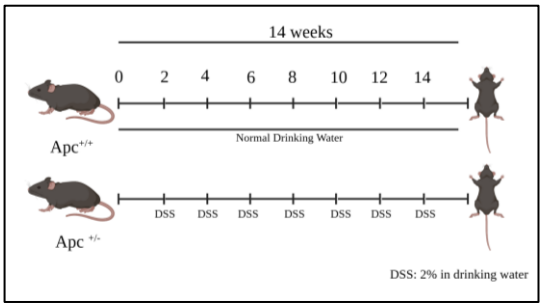

C

- Supplementary Figure 02:

A

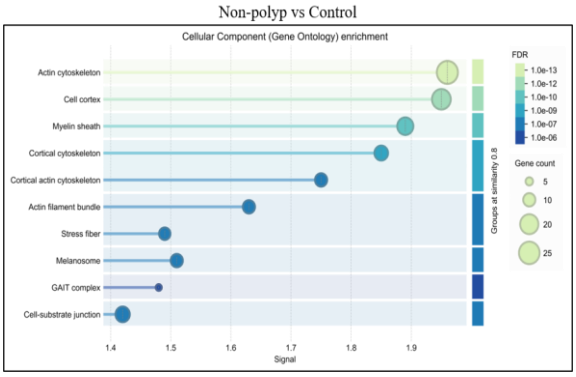

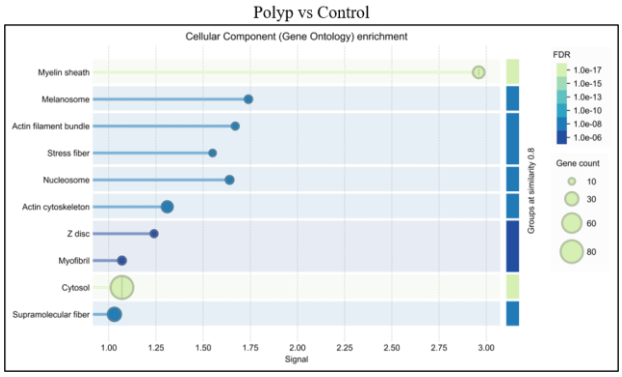

B

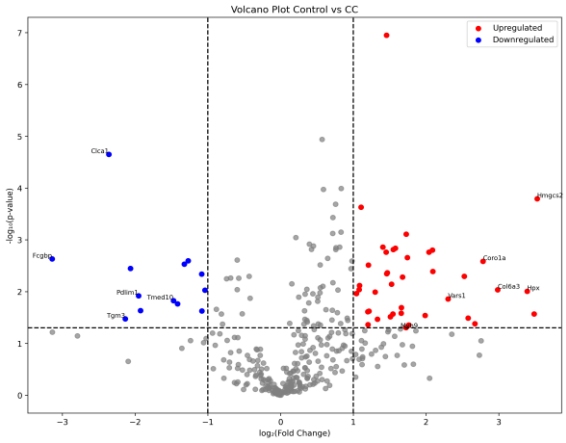

- Supplementary Figure 03:

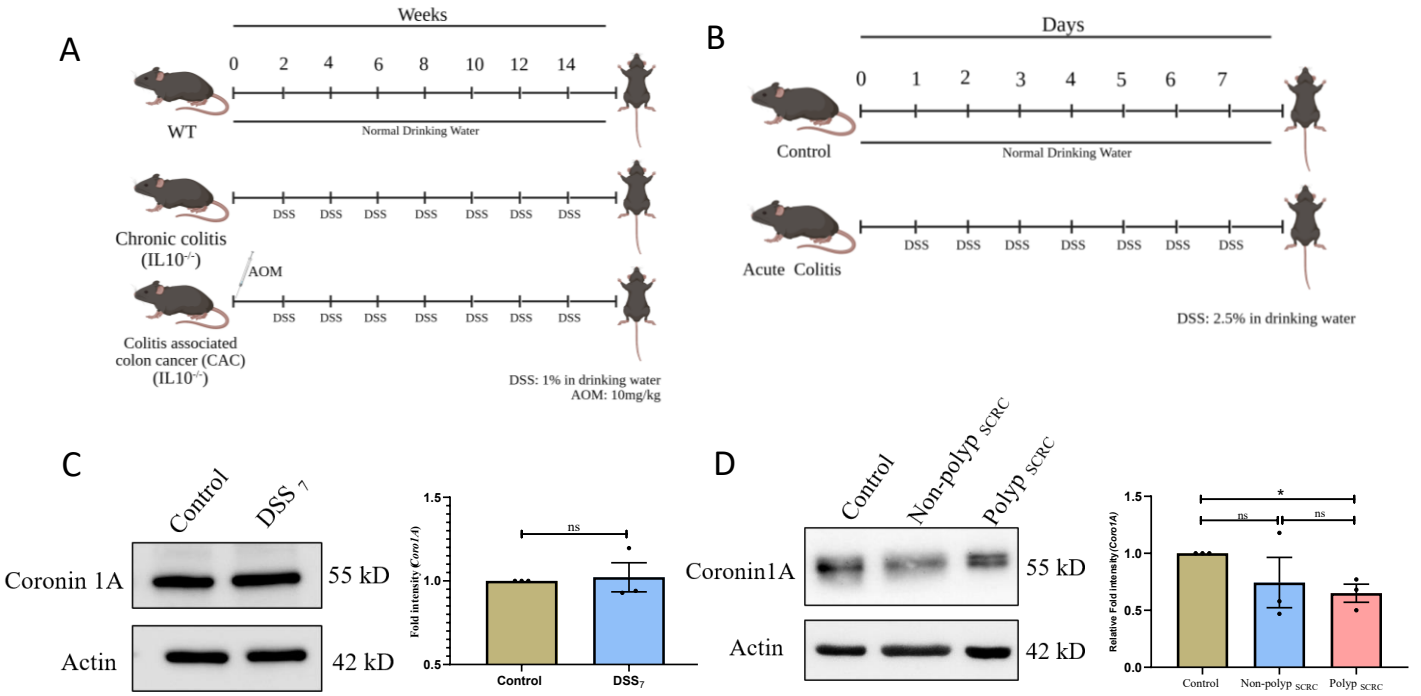

- Supplementary Figure 04:

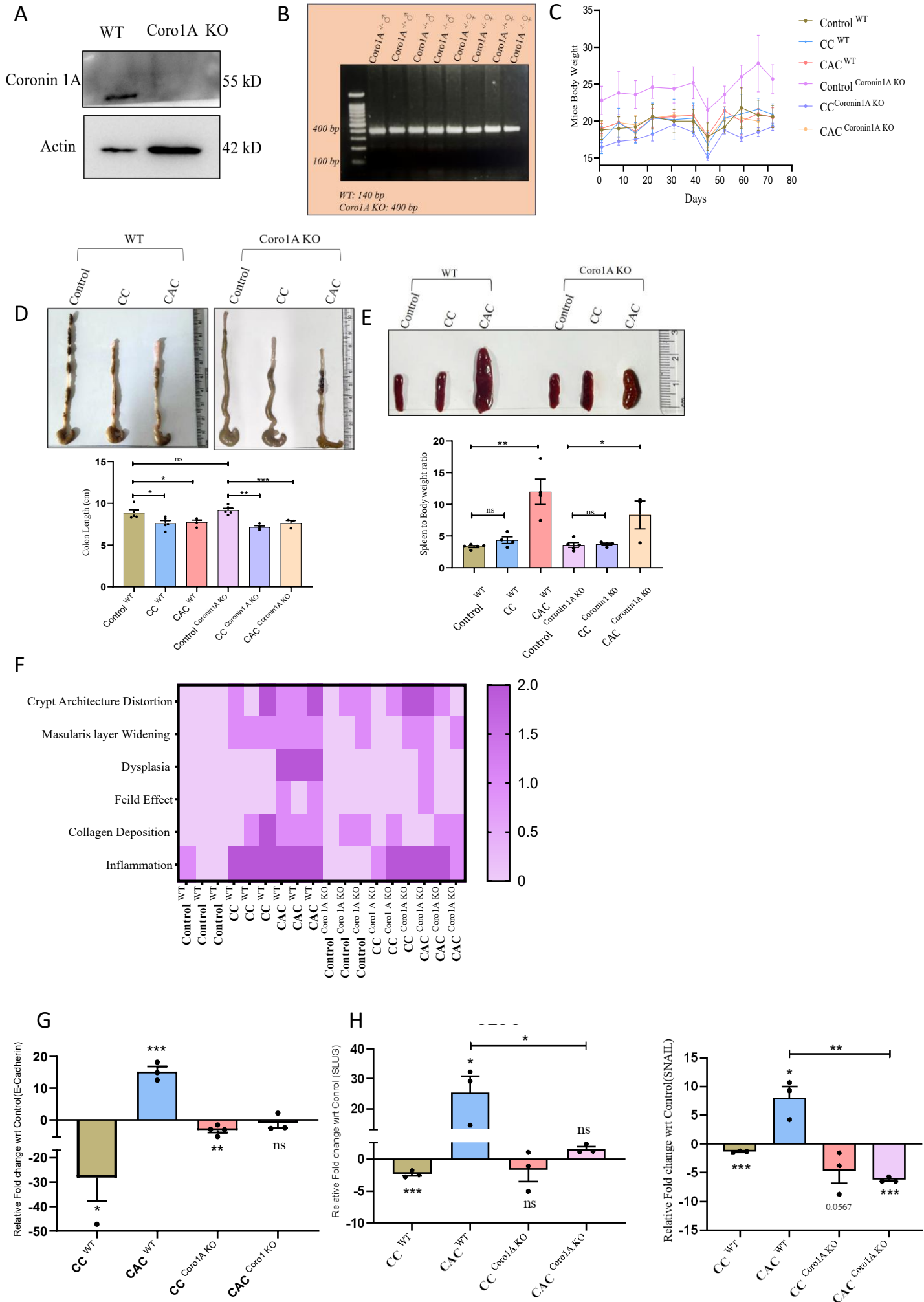

- Supplementary Figure 05:

A

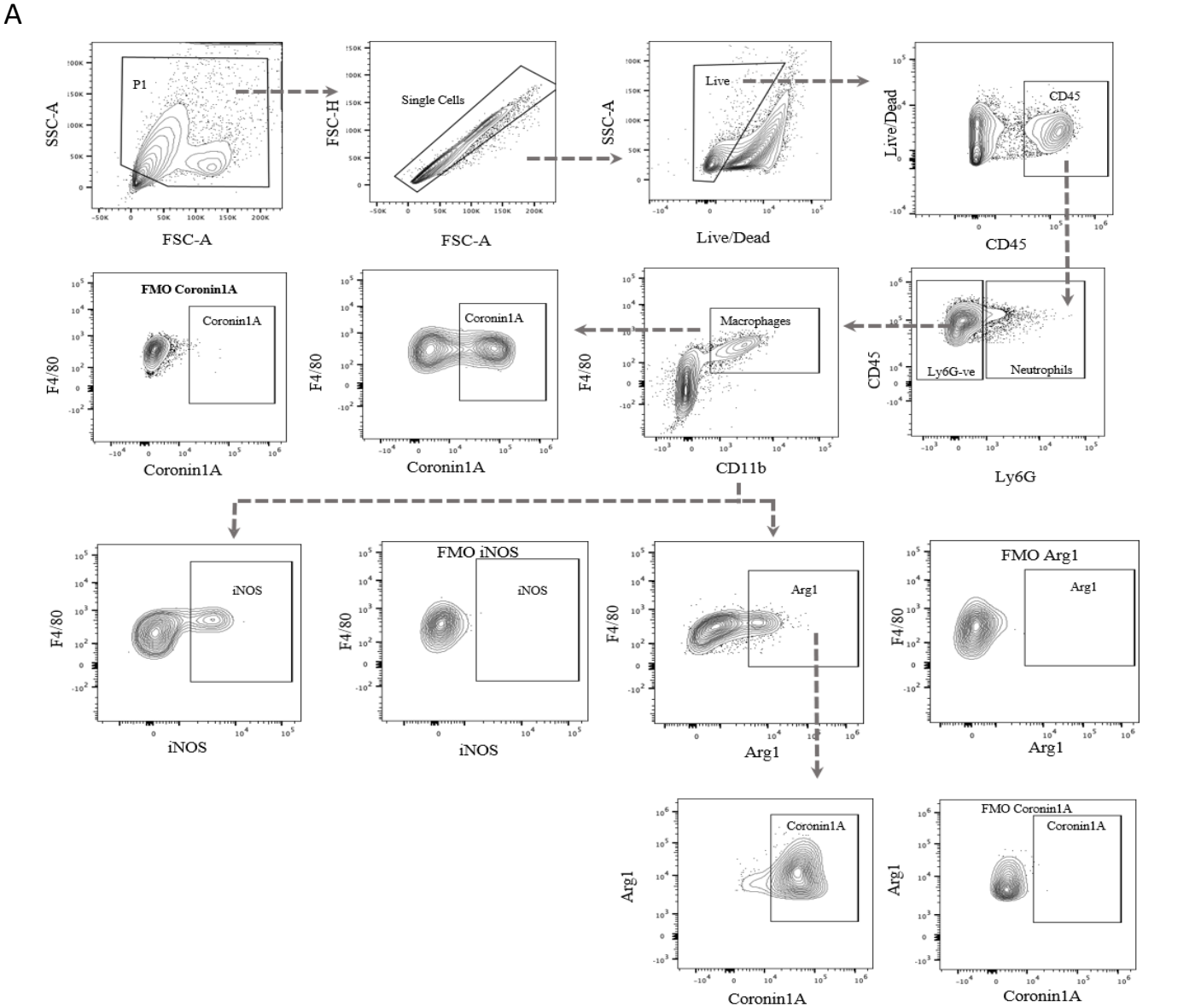

B

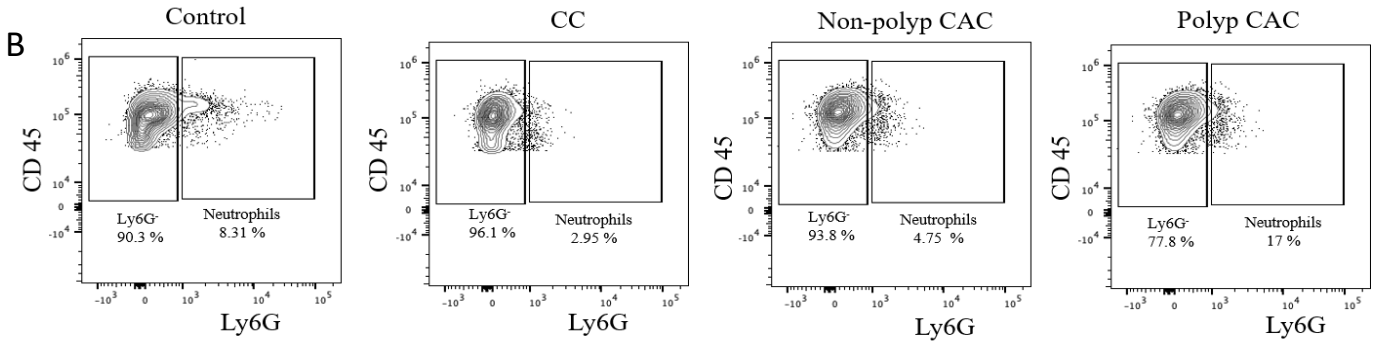

C

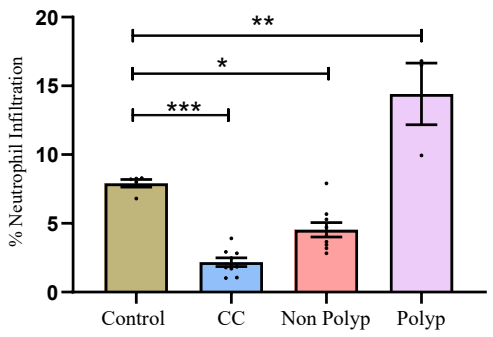

D

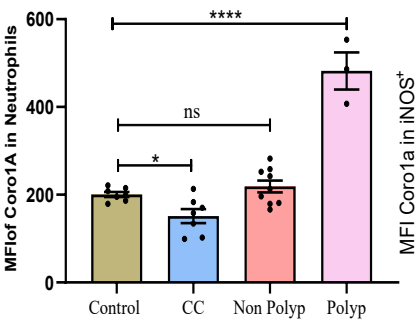

E

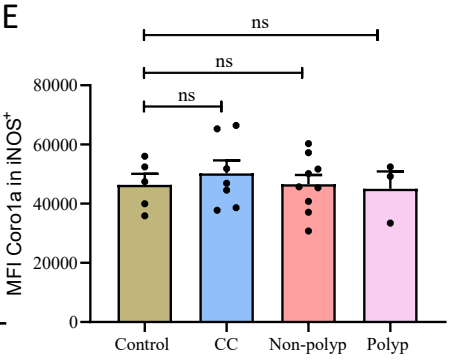

- Supplementary Figure 06:

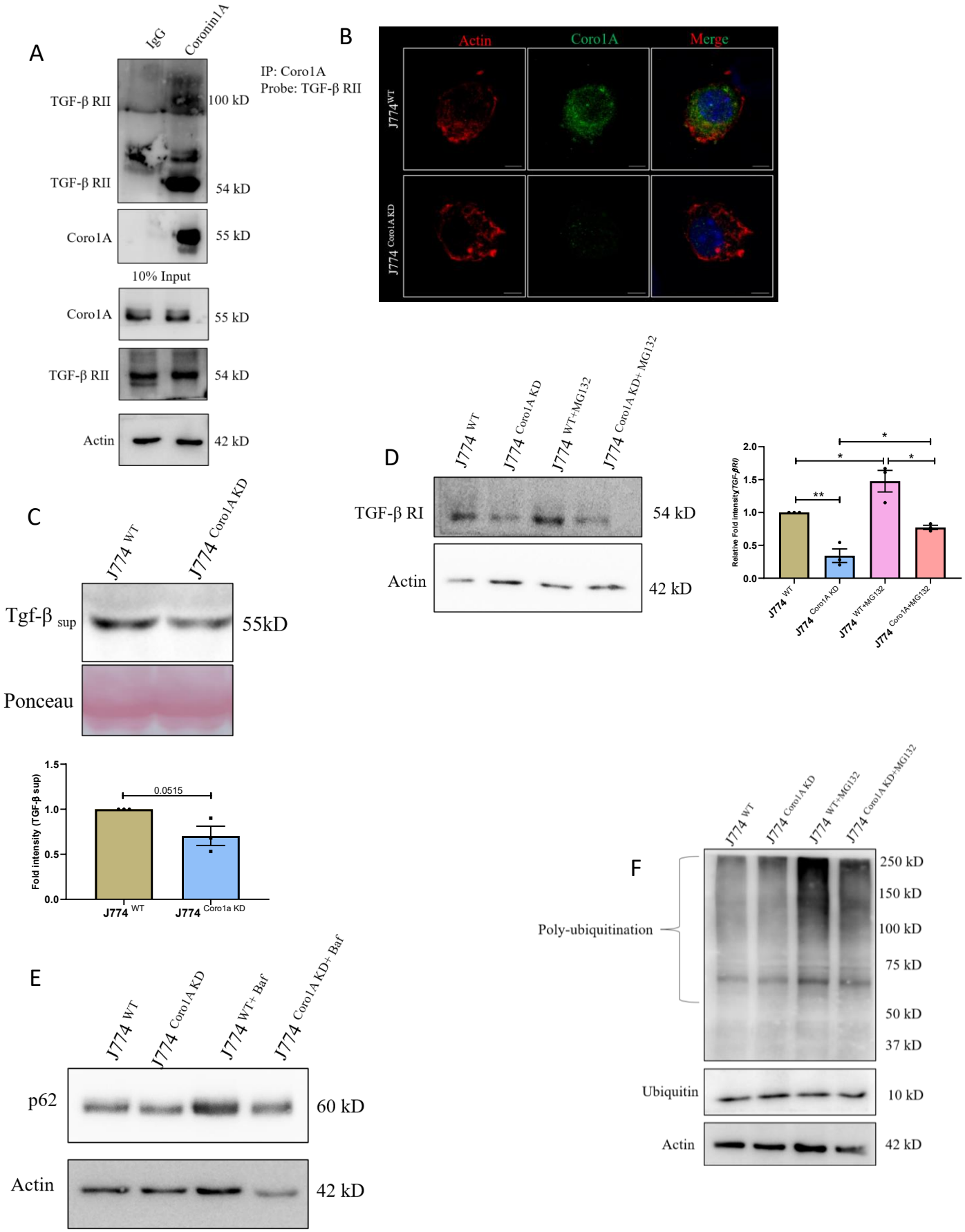

- Supplementary Figure 07:

A

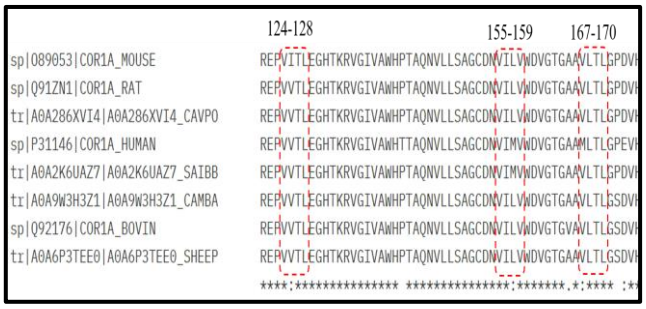

B

Protein	SIM Sites	SIM Sequence	Mutation in SIM Sequence
Coro1A	124-128	VITL	KITL
	155-159	VILV	KILV
	167-171	VLTL	KLTL

C

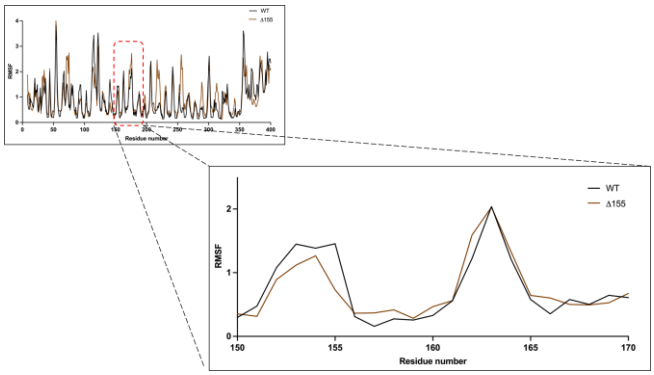

D

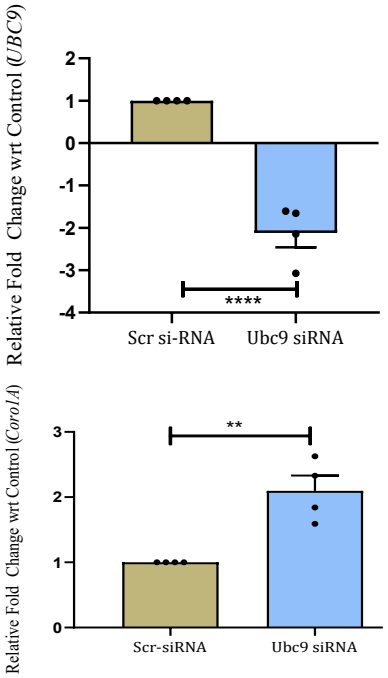

E

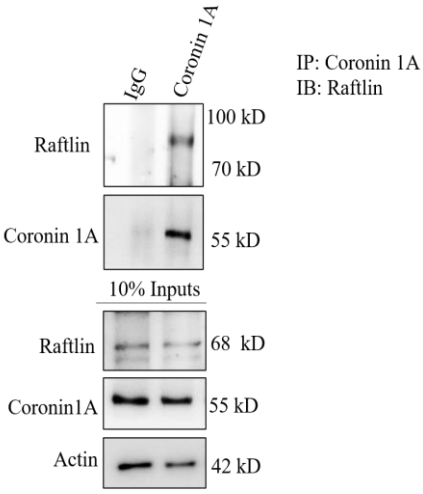

F

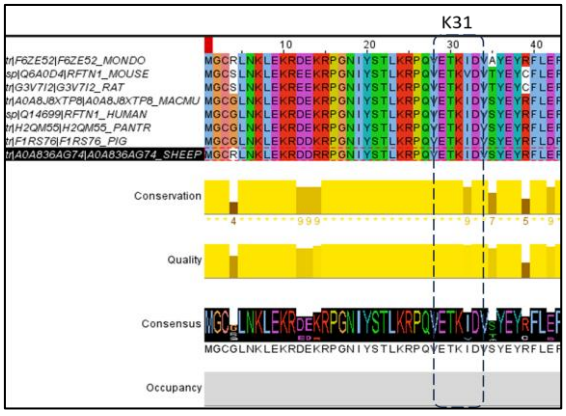
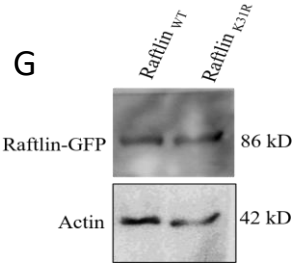
G